Distribution Agreement

In presenting this thesis or dissertation as a partial fulfillment of the requirements for an advanced degree from Emory University, I hereby grant to Emory University and its agents the non-exclusive license to archive, make accessible, and display my thesis or dissertation in whole or in part in all forms of media, now or hereafter known, including display on the world wide web. I understand that I may select some access restrictions as part of the online submission of this thesis or dissertation. I retain all ownership rights to the copyright of the thesis or dissertation. I also retain the right to use in future works (such as articles or books) all or part of this thesis or dissertation.

Signature:

_____ _____

Yawei Liu Date

Mechanism of charge separation and recombination in one-dimensional CdS-Pt nanorod heterostructures for solar energy conversion

By

Yawei Liu

Doctor of Philosophy

Chemistry

Dr. Tianquan Lian

Advisor

Dr. Brian Dyer

Committee Member

Dr. Joel Bowman

Committee Member

Accepted:

Kimberly Jacob Arriola, Ph.D.

Dean of the James T. Laney School of Graduate Studies

Date

Mechanism of charge separation and recombination in one-dimensional CdS-Pt nanorod heterostructures for solar energy conversion

By

Yawei Liu

B.S., University of Science and Technology of China, P.R. China, 2015

Advisor: Tianquan Lian, Ph.D.

An abstract of

A dissertation submitted to the Faculty of the

James T. Laney School of Graduate Studies of Emory University

in partial fulfillment of the requirements for the degree of

Doctor of Philosophy

in Chemistry

2021

Abstract

Mechanism of charge separation and recombination in one-dimensional CdS-Pt nanorod heterostructures for solar energy conversion

By Yawei Liu

Developing efficient solar energy conversion systems is of great significance to meet the explosively increasing demand for clean and renewable energies in the 21st century. Colloidal nanocrystals with strong light absorption, efficient carrier transport and broad tunability can be combined with catalytic metallic domains to form hybrid photocatalytic systems. The rational design of such hybrid semiconductor/metal photocatalysts for solar energy conversion requires comprehensive understanding of charge separation and recombination processes. Among various photocatalytic systems, Pt-tipped CdS nanorod heterostructures have been reported to undergo ultrafast charge separation to form long-lived charge-separated states and to demonstrate high quantum efficiencies for light driven H_2 production in the presence of sacrificial electron donors. In this dissertation, we use CdS-Pt nanorods as a model system to investigate how the light driven H_2 production performance of such photocatalysts can be systematically tuned by the size of the semiconductor and metal domains. Specifically, we examine how the effects of Pt size and CdS rod length on the H_2 generation quantum efficiency can be understood through their effects on various charge separation, charge recombination rates, and catalytic reaction rates.

First, we demonstrated that reducing the Pt size impedes both electron transfer from CdS to Pt and water reduction at Pt, leading to the decrease of hydrogen production quantum efficiency. Furthermore, we showed that increasing the CdS rod length prolongs the charge separated state lifetime and improve the hole removal efficiency by the hole scavengers, which leads to higher H_2 generation quantum efficiencies. Those dependences on the morphology of the heterostructures can be explained by a kinetic model that considers the competition between various forward charge separation and reaction processes (electron transfer, hole transfer, hole removal, water reduction) and background charge recombination processes of key intermediates. The efficiency of ssimultaneous multiple electron transfer from the CdS rod to the Pt tip was also examined as a function the excitation fluence. We observed efficient transfer of multiple electrons to the Pt tip and long lifetime of multiple charge separated states, indicating the feasibility of such systems for efficient light driven H_2 generation under concentrated sun light illumination.

Finally, we investigated the mechanism of plasmon-induced hot electron transfer from Au tips to CdS nanorods. The quantum efficiency of this process increases from 1% to 18% as the Au tip diameter decreases from 5.5 ± 1.1 to 1.6 ± 0.5 nm due to both enhanced hot electron generation and transfer efficiencies in small Au particles. Our findings suggest that reducing the Au particle size is an effective approach for enhancing the efficiency of plasmon induced hot electron transfer.

Mechanism of charge separation and recombination in one-dimensional CdS-Pt nanorod heterostructures for solar energy conversion

By

Yawei Liu

B.S., University of Science and Technology of China, P.R. China, 2015

Advisor: Tianquan Lian, Ph.D.

A dissertation submitted to the Faculty of the

James T. Laney School of Graduate Studies of Emory University

in partial fulfillment of the requirements for the degree of

Doctor of Philosophy

in Chemistry

2021

ACKNOWLEDGEMENT

First of all, I would like to express my most sincere gratitude to my advisor, Dr. Tianquan Lian, for his guidance, support and patience through my graduate study and research. I can still remember the time when I first joined the group, he told me that new materials may come and pass, as a physical chemist, our target is always to find out the universal principles behind those materials. This has become my criteria for my six-year graduate research. During my study, his insistence and devotion in overcoming research difficulties motivate me when I was lost in failure. His profundity of knowledge sheds new light when I sought for guidelines. His critical thinking about the big picture has reshaped me from a research rookie to a potential independent scientist, which I will treasure for my whole career. I also wish to thank my graduate committee professors, Dr. Joel Bowman and Dr. Brian Dyer for their valuable feedbacks and helpful comments to my graduate research.

It is my great honor to acknowledge my lab colleagues. They are my comrades in both research and life. I would like to thank Dr. Qiaoli Chen for teaching me synthetical skills and providing high quality nanocrystals during my first and second years of graduate study, Dr. Zihao Xu for his patient training on transient absorption spectroscopy, Qiliang Liu for his support both in- and out-side labs, and Dr. Wenxing Yang for his helpful discussion and revision of my manuscripts. I also want to express my gratitude for all my lab-mates: Dr. Qiuyang Li, Dr. Qiongyi Shang, Dr. Jia Song, Dr. Laura Kiefer, Dr. Chaoyu Li, Dr. Dhritiman Bhattacharyya, Tao Jin, Sara Gebre, Jinhui Meng, Fengyi Zhao, Sheng He, Sa Suo and Paul Jin --- I will treasure every moment working in the lab with you.

Finally, I would like to express my love deep-heartedly to my family, especially my parents for their continuous support. Their unconditional encouragement has been my largest spiritual power in my whole life.

Table of contents

List of Figures

spectra of CdS and CdS-Pt at 9-10 ns. The derivative feature shown in CdS-Pt indicates the presence of a charge separated state. Selected time delays are same for (A) and (B) and are specified in (A). (C) Comparison of 1Σ exciton bleach recovery kinetics of CdS monitored at bleach maximum ~461 nm and CdS-Pt NRs monitored at 466 nm. The TA signal of CdS-Pt at this wavelength, an isosbestic point of the charge separated state spectrum (inset of Figure 5.3B), contains only the exciton bleach amplitude, reflecting the kinetics of electron at the CdS conduction band edge. The faster exciton bleach recovery kinetics in CdS-Pt indicates electron transfer from the CdS to Pt. (D) Schematic energy level diagram of CdS-Pt NRs and key processes of photogenerated carriers: (i) Electron relaxation to the band edge (91±4 fs) and hole localization to the trap sites, (ii) exciton recombination (204±2 ns), (iii) Electron transfer from the CdS conduction band to the Pt tip (5.6±0.6 ps) and (iv) recombination of the electron in the Pt with the trapped hole in CdS..... 79

Figure 5.4. Multiple exciton dynamics in CdS NRs. (A) TA spectra of CdS NRs measured at excitation fluence of 175 mW/cm^2 (initial average number of excitons per NR of <N>~20) at selected delay times. (B) Comparison of normalized 1Σ exciton bleach recovery kinetics measured under various fluences (<N> ~0.2 to 40> and their fit according to the carrier-collision model described in the main text. These bleach kinetics have been normalized to the same amplitude at 100 ns, and show excellent agreement at 50 ns to 1 μs, when only single exciton states remain in these NRs. (C) Comparison of exciton bleach kinetics measured at <N>~0.2 (red circles) and <N>~0.3 (orange diamonds). (Inset) Biexciton decay kinetics (purple open circles) obtained by subtracting the normalized 1Σ exciton bleach kinetics measured at <N>~0.2 from that of <N>~0.3 and its fit to a single exponential decay function with a time constant of 2.0±0.2 ns (gray line). (D) Auger lifetime of N exciton states in CdS NRs obtained through the fit shown in Figure 5.4B

List of Tables

Chapter 1. Introduction

With the expansion of human activity and urgent quest on green environment, finding clean and renewable resources to replace transitional fossil fuels is one of the most urgent scientific challenges for the 21st century. In nature, plants harvest solar energy, convert it into hydrocarbons and store as consumptive energy. Animals gain food supply from plants. Solar energy is the fundamental of the food chains on earth. The incident solar energy on the earth every hour is sufficient to supply human's energy demand for a whole year.[1-2] Thus, efficient harvest and conversion of solar energy into electricity by photovoltaics or solar fuels is a ultimate solution for energy concerns. [3-7] Compared with the photovoltaics, solar fuels have advantages in higher energy density and easier energy storage and thus have attracted intense research interests for decades. [5, 8-11]

In artificial photosynthesis, semiconductor/metal heterostructures have been widely investigated because of the combined advantages of semiconductor (strong light absorption, long carrier lifetime, long distance charge transport) and metal (excellent catalytic reactivities).[3, 8, 12] Upon excitation, semiconductor nanocrystals act as light absorbers to capture solar light and generate high-energy electron–hole pairs. The conduction band (CB) electron can be selectively transferred to reactive sites, such as enzymes, molecular catalysts and metal nanoparticles to initiate reduction reactions, including proton reduction, CO_2 reduction, and N_2 fixation. Similarly, the valence band (VB) hole can be transferred to the oxidatively active sites to initiate oxidation reactions. With efficient charge separation and catalysis, the energy of the absorbed photons is converted to chemical energy stored in fuels or value-added chemicals, as shown in Figure 1.1.[4] Among different types of solar fuels, H_2 production from water splitting is one of the most widely

studied reactions and is regarded as one of the promising candidates of clean solar fuels. [9, 13-21] Consumption of H_2 only produces H_2O, largely reducing the release of greenhouse gases, compared with hydrocarbon fossils. Second, 70% of earth is consisted of water, guaranteeing its easy accessibility.

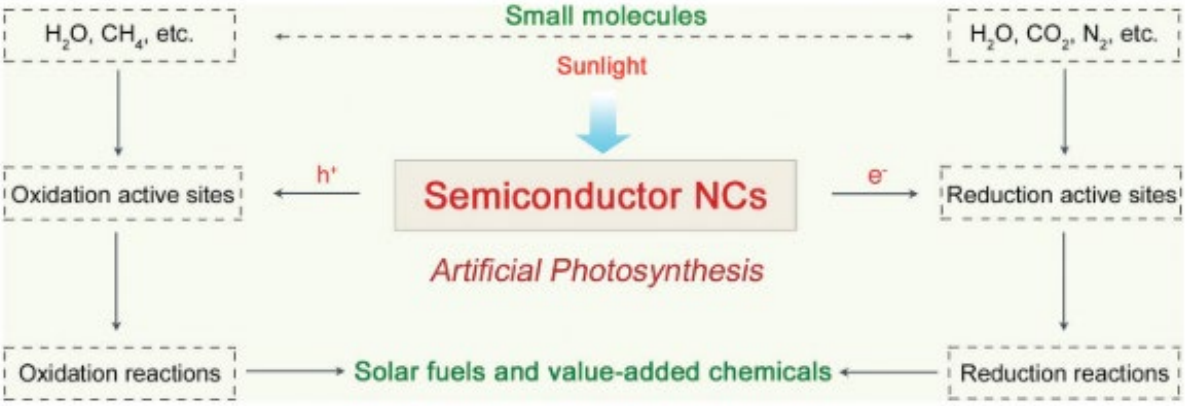

Figure 1.1. Schematic illustration of typical semiconductor NCs based artificial photosynthesis for small molecules activation, thus achieving solar-to chemical conversion. Adapted with permission from *Chem. Soc. Rev.*, **2020**, 49, 9028.

Semiconductor/metal heterostructures in the quantum confined nanometer size regimes offer additional advantages, including large surface area and size dependent tunable band gap and band edge positions through the quantum confinement effect.[8] Manipulating the band alignment of the NC offer new possibilities in controlling the carrier dynamics which cannot be realized by bulk materials, such as, controlling the charge separation distance by tuning materials dimension, charge transfer driving force by selecting suitable donor-acceptor pairs.[8] Recently, concept of "wavefunction engineering" has also been successfully applied in modifying the spatial distribution of the CB electron and VB hole in excitonic states by tuning the material composition and size.[22] Thus, studying the band alignment of semiconductor heterostructures offer insights in

understanding the mechanism of carrier dynamics and help improve rational design for next generation photocatalytic systems.

1.1 Band alignment of metal-tipped nanorods.

To realize rational design of the 1D heterostructure, state-of-art ultrafast optical spectroscopy has been utilized to monitor the carrier dynamics.[23-25] It has been reported the carrier dynamics in those materials are heavily dependent on their band structure.[26-27] With particle radius, *r*, smaller than the exciton Bohr radius, quantum confinement leads to discrete energy levels, described by the particle-in-box model.[28-29] In this model, the bandgap change decreases with size, leading to *r*-dependent redox or oxidation potentials in those nanomaterials.[30] However, unlike quantum dots, in 1D heterostructures, confinement effect only occurs in the radial direction, while the dimension on the longitude direction can vary from nm to μm scale with negligible effects on the energy level.[31-32] Figure 1.2 shows the absorption spectra and key energy levels of CdSe NRs of various length and diameters.

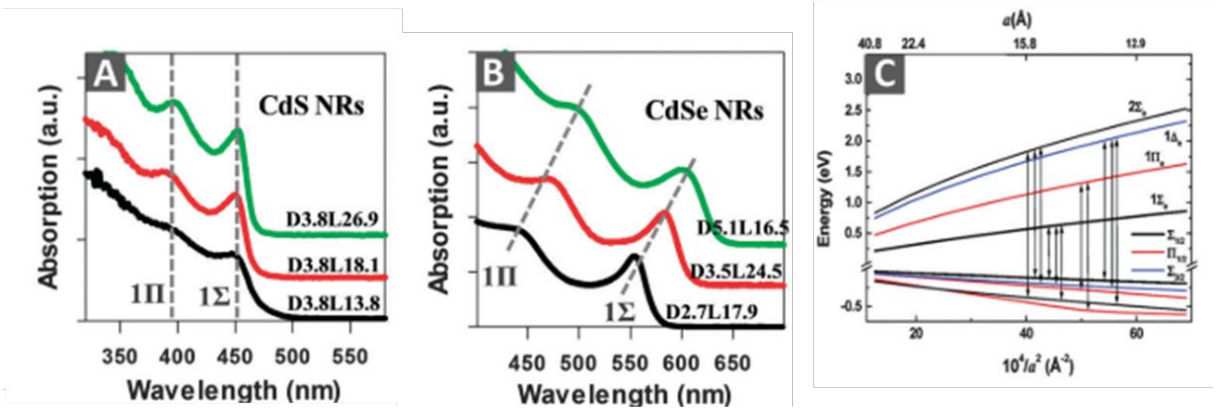

Figure 1.2 Electronic structure and optical property of NRs. (A) Static absorption spectra of three CdS NRs with similar diameters (3.8 nm) and different lengths (black: 13.8 nm; red: 18.1 nm; green: 26.9 nm). (B) Static absorption spectra of three CdSe NRs with different diameters (black: 2.7 nm, red: 3.5 nm, green: 5.1 nm) and lengths (black: 17.9 nm, red: 24.5 nm, green: 16.5 nm).

(C) Size dependence of the electron and hole energy levels in CdSe NRs calculated by effective mass six-band model. The NR was considered as an ellipsoid crystal with major semi-axis b (the NR axis) much larger than the minor semi-axis a (the NR radius). Arrows show optically allowed interband transitions. Reproduced with permission from *Chem. Soc. Rev.*, **2016**, 45, 3781-3810 and *Nano Lett*., **2004**, 4, 1821–1825.

Semiconductor nanoheterostructures offer additional opportunities to tune the electron and hole spatial distribution through their size and composition. For instance, CdSe@CdS dot-in-rod NRs consist of one CdSe QD core and CdS rod arm. Due to the lower conduction band position and higher valence band position in CdSe, holes are localized in the CdSe, while the electron wavefunction can be tuned by controlling the offset between the their conduction band edge positions. Type I structure forms when the offset is larger than the room temperature *kT*, leading to localized electron wavefunction in the CdSe core. When the offset is negligible, the electron extends into the rod region, forming a quasi-type II band alignment.[33] By changing CdSe to ZnSe core, which has both higher CB and VB relative to CdS, Type II band alignment can be achieved with electron localized in CdS nanorod and holes localized in ZnSe.[22] Three types of band alignment are shown in Figure 1.3.

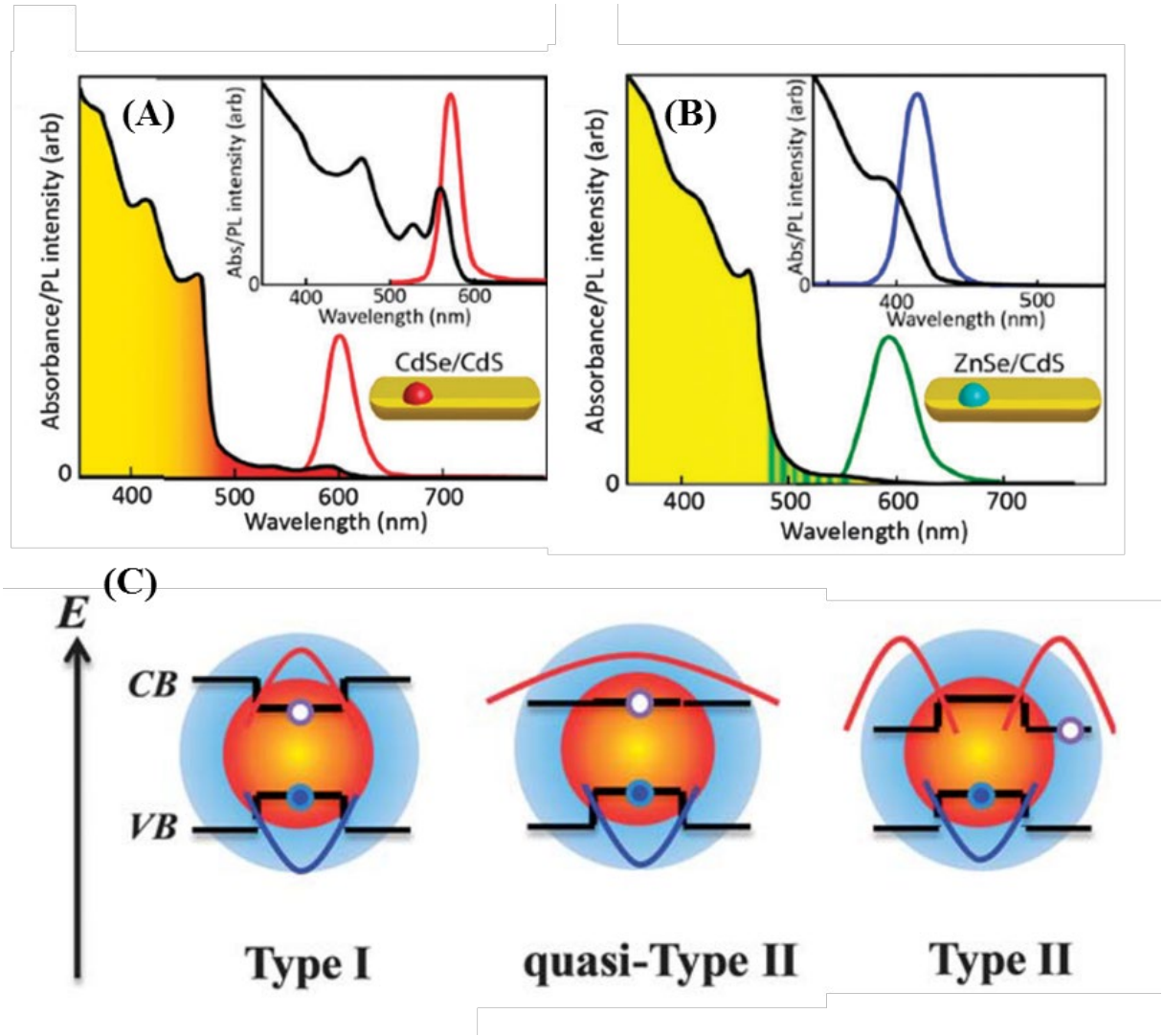

Figure 1.3. Absorption and PL spectra of dot-in-rod NRs with various materials compositions (A) CdSe@CdS NRs, (B) ZnSe@CdS NRs. Insets in (A-B): absorption and PL of the corresponding QD cores (where available). (C) Schematic representation of type I, quasi-type II and type II band alignment and carrier localization in core/shell heterostructures. The black lines indicate the band edge positions in the core and shell materials. The red and blue (inverted) lines depict the electron and hole envelope functions, respectively. (A) and (B) are reproduced with permission from *Chem. Soc. Rev*., **2016**, 45, 3781-3810. (C) is reproduced with permission from *Energy Environ. Sci.*, **2012**, 5, 9406–9418.

1.2 Charge dynamics and H_2 production performance

Excitation of the semiconductor light absorber generates excitons in the semiconductor. The band alignment between the metal and semiconductor domains determine the electron and hole transfer dynamics. Figure 1.4 shows the energy levels of CdS-Pt nanorods. When the absorber CdS is attached to electron acceptors, such as reducible molecules or metal (Pt) tips, or hole acceptors with suitable energies, electrons and holes transfer into different targets and form charge-separated states. Typically, in CdS nanorods, holes are quickly trapped by the surface states and then move to surface thiol ligands (L) with rate of k_{HT}, while electrons diffuse within the rod and are finally collected by the Pt (k_{ET}). With the presence of hole sacrificial donor (SD), trapped holes are further removed (k_{HS}). Electron accumulation in the Pt leads to the reduction of water into H_2 competing with the charge recombination (k_{CRi},i=1-4).

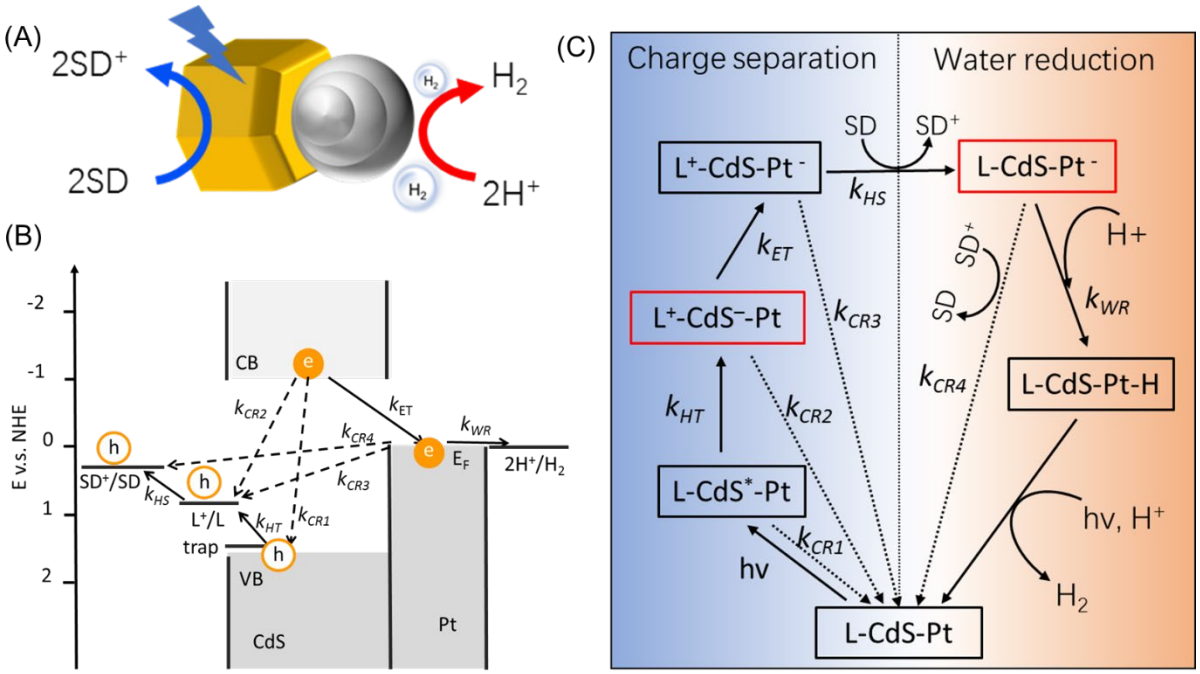

Figure 1.4. Scheme of photocatalytic generation of H_2 in CdS-Pt heterostructures. (A) A cartoon of the H_2 production with CdS-Pt NRs.. (B) Simplified schematic energy levels and charge

separation and recombination processes relevant to photocatalytic H_2 generation with exciton generated in CdS. (C) Simplified kinetic model with key intermediate states and processes for light driven H_2 generation in (B) using L-CdS-Pt nanorods.

1.3 Multielectron interaction in metal-tipped nanorods

Solar fuels formation reactions usually require the transfer of multielectrons and protons. Under solar flux, the multiple electrons are typically transferred sequentially. Under strong light intensity, multiple exciton states can be easily generated in semiconductor nanocrystals, suggesting the possibility of simultaneously delivering multiple electrons to the catalyst. With more than one electron -hole pair in the light absorber, many-body interaction starts to dominate the carrier lifetimes, leading Auger recombination process.[34-38] In Auger recombination, one exciton recombination by exciting another electron or hole into higher energy states, as shown in Figure 1.5A.[35] Auger recombination largely accelerates the electron-hole pair recombination and shortens the carrier lifetime. This rate usually scales with carrier density[37] (Figure 1.5B) and cannot be negligible when multielectron transfer is required. Consequently, understanding the capability of electron accumulation in a catalyst and the competition between Auger recombination and electron transfer (Figure 1.5C) has significance in promoting multielectron reduction efficiencies. In this

thesis, we use CdS-Pt nanorods to illustrate the competition between the Auger recombination and multielectron transfer from CdS to Pt.

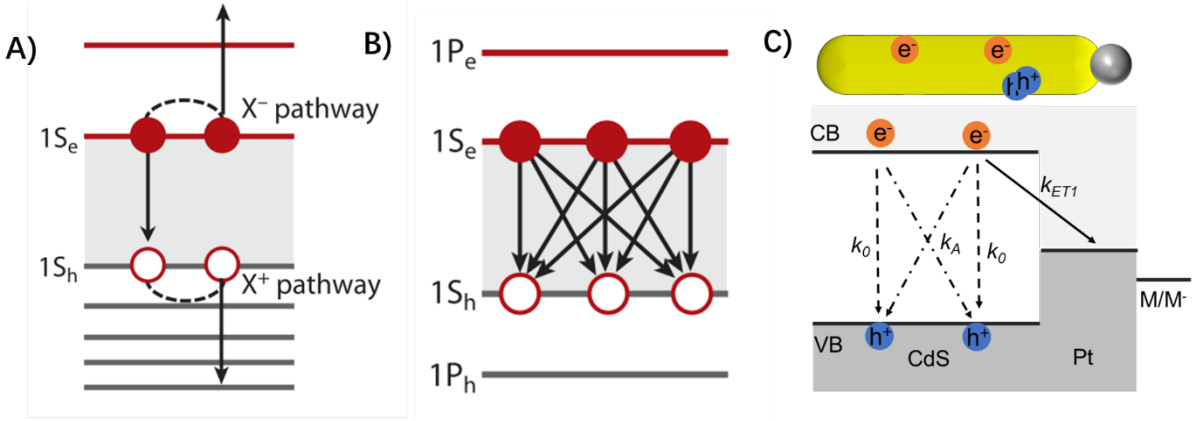

Figure 1.5. (A) Auger combination of biexciton state. The left exciton recombines by either exciting the hole or electron into high states. B) The pathways of Auger recombination in triple exciton state. C) Transfer of the first electron from the biexciton state competes with intrinsic exciton recombination (k_0) and Auger recombination (k_A) of bi-exciton state.

1.4 Plasmon-induced hot electron transfer

In a traditional semiconductor-metal heterostructure, such as those discussed above, the semiconductor usually serves as the light absorber, while the metal domain acts as catalytical sites. However, recent studies have shown plasmonic metal can serve as light absorber and generate hot electrons with capability of initiating reactions on its own.[39] This phenomenon, called plasmon-induced hot electron transfer (PIHT) has attracted intense research interests.[10, 15, 40-43] Plasmon, the collective motion of many electrons excited by light absorption, can decay into hot electrons or holes via intraband or interband pathways (Figure 1.6A), followed by transferring into the attached molecules' antibonding bonds or semiconductors' conduction band. [44-47] So far, PIHT has been reported in many systems but the efficiencies are often low due to the fast carrier relaxation and

charge recombination (Figure 1.6B).[48] Understanding the mechanisms of PIHT are needed to improve their efficiencies. 1D semiconductor NR heterostructures are ideal model system for exploring the PIHT mechanism. The selective deposition of the metal domain at the nanorod tip region makes a well-defined system with known Au particle numbers, independently tunable CdS and Au size, and strong metal-semiconductor interaction.[49] In this thesis, Au-CdS nanorod is used as a model system to investigate the mechanism of hot electron injection through a systematic study of the effect of Au size.

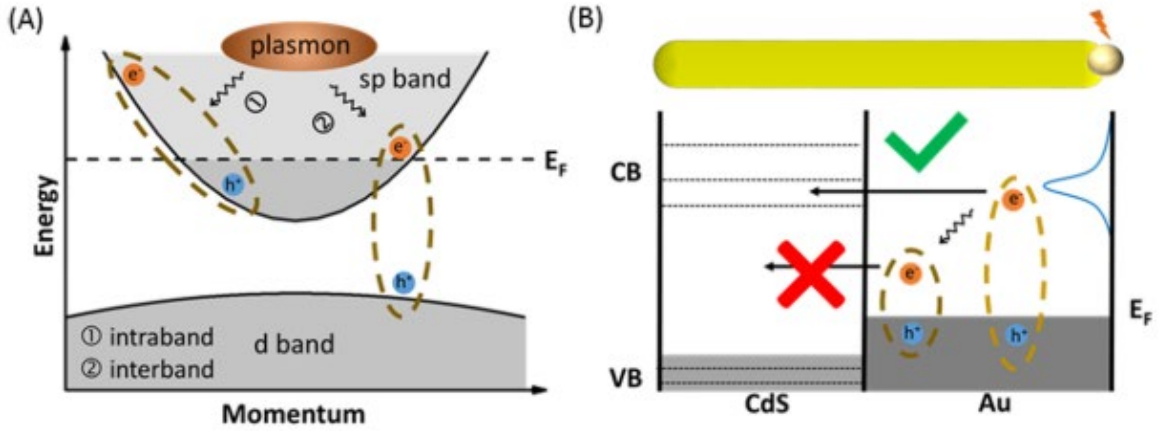

Figure 1.6. (A) Plasmon-induced hot electron transfer at metal/semiconductor junction. Interband (d−sp) and intraband (sp−sp) decay pathways for plasmon in metals. (B) Sequential plasmon decay and hot carrier transfer at Au nanoparticle/CdS nanorod interface. Adapted with permission from *Nano Lett*. 2020, 20, 4322−4329.

1.5 Conclusion

In this thesis, we will discuss the light-driven H_2 generation using quantum nanorods. Chapter 2 describes the sample preparation, mainly the synthesis of nanorods with metal tips. Systematic studies of the effects of the Pt size and CdS rod length on H_2 production quantum efficiencies in

CdS-Pt will be discussed in Chapter 3 and Chapter 4, respectively. Multicarrier interaction is also investigated in Pt tipped CdS to offer insights on multielectron transfer in Chapter 5. Finally, we will introduce the plasmon-induced hot electron injection mechanism in Au-tipped CdS in Chapter 6.

References

1. Lewis, N. S., Toward Cost-Effective Solar Energy Use. **2007**, *315*, 798-801.
2. Kabir, E.; Kumar, P.; Kumar, S.; Adelodun, A. A.; Kim, K.-H., Solar Energy: Potential and Future Prospects. *Renewable and Sustainable Energy Reviews* **2018**, *82*, 894-900.
3. Burke, R.; Bren, K. L.; Krauss, T. D., Semiconductor Nanocrystal Photocatalysis for the Production of Solar Fuels. *J Chem Phys* **2021**, *154*, 030901.
4. Li, X. B.; Xin, Z. K.; Xia, S. G.; Gao, X. Y.; Tung, C. H.; Wu, L. Z., Semiconductor Nanocrystals for Small Molecule Activation Via Artificial Photosynthesis. *Chem Soc Rev* **2020**, *49*, 9028-9056.
5. Li, X.; Yu, J.; Jaroniec, M.; Chen, X., Cocatalysts for Selective Photoreduction of Co2 into Solar Fuels. *Chem. Rev.* **2019**, *119*, 3962-4179.
6. Weiss, E. A., Designing the Surfaces of Semiconductor Quantum Dots for Colloidal Photocatalysis. *ACS Energy Letters* **2017**, *2*, 1005-1013.
7. Wilker, M. B.; Schnitzenbaumer, K. J.; Dukovic, G., Recent Progress in Photocatalysis Mediated by Colloidal Ii-Vi Nanocrystals. *Isr J Chem* **2012**, *52*, 1002-1015.
8. Wu, K.; Lian, T., Quantum Confined Colloidal Nanorod Heterostructures for Solar-to-Fuel Conversion. *Chem. Soc. Rev.* **2016**, *45*, 3781-810.
9. Tachibana, Y.; Vayssieres, L.; Durrant, J. R., Artificial Photosynthesis for Solar Water-Splitting. *Nat. Photon.* **2012**, *6*, 511-518.
10. Thomann, I.; Pinaud, B. A.; Chen, Z. B.; Clemens, B. M.; Jaramillo, T. F.; Brongersma, M. L., Plasmon Enhanced Solar-to-Fuel Energy Conversion. *Nano Letters* **2011**, *11*, 3440-3446.
11. Gust, D.; Moore, T. A.; Moore, A. L., Solar Fuels Via Artificial Photosynthesis. *Acc. Chem. Res.* **2009**, *42*, 1890-1898.
12. Kranz, C.; Wachtler, M., Characterizing Photocatalysts for Water Splitting: From Atoms to Bulk and from Slow to Ultrafast Processes. *Chem. Soc. Rev.* **2021**, *50*, 1407-1437.
13. Simon, T., et al., Redox Shuttle Mechanism Enhances Photocatalytic H2 Generation on Ni-Decorated Cds Nanorods. *Nat. Mater.* **2014**, *13*, 1013-1018.
14. Warren, S. C.; Thimsen, E., Plasmonic Solar Water Splitting. *Energy Environ. Sci.* **2012**, *5*, 5133-5146.
15. Chen, J. J.; Wu, J. C. S.; Wu, P. C.; Tsai, D. P., Plasmonic Photocatalyst for H-2 Evolution in Photocatalytic Water Splitting. *Journal of Physical Chemistry C* **2011**, *115*, 210-216.
16. Maeda, K.; Domen, K., Photocatalytic Water Splitting: Recent Progress and Future Challenges. *J. Phys. Chem. Lett.* **2010**, *1*, 2655-2661.
17. Kudo, A.; Miseki, Y., Heterogeneous Photocatalyst Materials for Water Splitting. *Chem. Soc. Rev.* **2009**, *38*, 253-278.

18. Fu, C. F.; Sun, J.; Luo, Q.; Li, X.; Hu, W.; Yang, J., Intrinsic Electric Fields in Two-Dimensional Materials Boost the Solar-to-Hydrogen Efficiency for Photocatalytic Water Splitting. *Nano Lett* **2018**, *18*, 6312-6317.
19. Zheng, Y.; Jiao, Y.; Jaroniec, M.; Qiao, S. Z., Advancing the Electrochemistry of the Hydrogen-Evolution Reaction through Combining Experiment and Theory. *Angew. Chem. Int. Ed.* **2015**, *54*, 52-65.
20. Zou, X.; Zhang, Y., Noble Metal-Free Hydrogen Evolution Catalysts for Water Splitting. *Chem. Soc. Rev.* **2015**, *44*, 5148-5180.
21. Ingram, D. B.; Linic, S., Water Splitting on Composite Plasmonic-Metal/Semiconductor Photoelectrodes: Evidence for Selective Plasmon-Induced Formation of Charge Carriers near the Semiconductor Surface. *Journal of the American Chemical Society* **2011**, *133*, 5202-5205.
22. Zhu, H.; Lian, T., Wavefunction Engineering in Quantum Confined Semiconductor Nanoheterostructures for Efficient Charge Separation and Solar Energy Conversion. *Energy Environ. Sci.* **2012**, *5*, 9406-9418.
23. Li, Q.; Lian, T., Area-and Thickness-Dependent Biexciton Auger Recombination in Colloidal Cdse Nanoplatelets: Breaking the "Universal Volume Scaling Law". *Nano Lett.* **2017**, *17*, 3152-3158.
24. Zhu, H.; Yang, Y.; Hyeon-Deuk, K.; Califano, M.; Song, N.; Wang, Y.; Zhang, W.; Prezhdo, O. V.; Lian, T., Auger-Assisted Electron Transfer from Photoexcited Semiconductor Quantum Dots. *Nano Lett* **2014**, *14*, 1263-9.
25. Zhu, H.; Lian, T., Enhanced Multiple Exciton Dissociation from Cdse Quantum Rods: The Effect of Nanocrystal Shape. *J. Am. Chem. Soc.* **2012**, *134*, 11289-97.
26. Eshet, H.; Grunwald, M.; Rabani, E., The Electronic Structure of Cdse/Cds Core/Shell Seeded Nanorods: Type-I or Quasi-Type-Ii? *Nano Lett* **2013**, *13*, 5880-5.
27. Acharya, K. P.; Khnayzer, R. S.; O'Connor, T.; Diederich, G.; Kirsanova, M.; Klinkova, A.; Roth, D.; Kinder, E.; Imboden, M.; Zamkov, M., The Role of Hole Localization in Sacrificial Hydrogen Production by Semiconductor-Metal Heterostructured Nanocrystals. *Nano Lett* **2011**, *11*, 2919-26.
28. Yu, W. W.; Qu, L.; Guo, W.; Peng, X., Experimental Determination of the Extinction Coefficient of Cdte, Cdse, and Cds Nanocrystals. *Chemistry of Materials* **2003**, *15*, 2854-2860.
29. Peng, X.; Manna, L.; Yang, W.; Wickham, J.; Scher, E.; Kadavanich, A.; Alivisatos, A. P., Shape Control of Cdse Nanocrystals. *Nature* **2000**, *404*, 59-61.
30. Kershaw, S. V.; Susha, A. S.; Rogach, A. L., Narrow Bandgap Colloidal Metal Chalcogenide Quantum Dots: Synthetic Methods, Heterostructures, Assemblies, Electronic and Infrared Optical Properties. *Chem Soc Rev* **2013**, *42*, 3033-87.
31. Shabaev, A.; Efros, A. L., 1d Exciton Spectroscopy of Semiconductor Nanorods. *Nano Lett.* **2004**, *4*, 1821-1825.
32. Efros, A. L.; Rosen, M., The Electronic Structure of Semiconductor Nanocrystals. *Annu. Rev. Mater. Sci.* **2000**, *30*, 475-521.
33. Wu, K.; Hill, L. J.; Chen, J.; McBride, J. R.; Pavlopolous, N. G.; Richey, N. E.; Pyun, J.; Lian, T., Universal Length Dependence of Rod-to-Seed Exciton Localization Efficiency in Type I and Quasi-Type Ii Cdse@Cds Nanorods. *ACS Nano* **2015**, *9*, 4591-4599.
34. Garcia-Santamaria, F.; Brovelli, S.; Viswanatha, R.; Hollingsworth, J. A.; Htoon, H.; Crooker, S. A.; Klimov, V. I., Breakdown of Volume Scaling in Auger Recombination in Cdse/Cds Heteronanocrystals: The Role of the Core-Shell Interface. *Nano Lett.* **2011**, *11*, 687-93.

35. Klimov, V. I., Multicarrier Interactions in Semiconductor Nanocrystals in Relation to the Phenomena of Auger Recombination and Carrier Multiplication. *Annu. Rev. Condens. Matter Phys.* **2014**, *5*, 285-316.
36. Klimov, V. I.; Mikhailovsky, A. A.; McBranch, D. W.; Leatherdale, C. A.; Bawendi, M. G., Quantization of Multiparticle Auger Rates in Semiconductor Quantum Dots. *Science* **2000**, *287*, 1011-1013.
37. Klimov, V. I.; McGuire, J. A.; Schaller, R. D.; Rupasov, V. I., Scaling of Multiexciton Lifetimes in Semiconductor Nanocrystals. *Physical Review B* **2008**, *77*.
38. Wu, K.; Lim, J.; Klimov, V. I., Superposition Principle in Auger Recombination of Charged and Neutral Multicarrier States in Semiconductor Quantum Dots. *ACS Nano* **2017**, *11*, 8437-8447.
39. Mukherjee, S.; Libisch, F.; Large, N.; Neumann, O.; Brown, L. V.; Cheng, J.; Lassiter, J. B.; Carter, E. A.; Nordlander, P.; Halas, N. J., Hot Electrons Do the Impossible: Plasmon-Induced Dissociation of H2 on Au. *Nano Lett.* **2013**, *13*, 240-247.
40. Wu, K.; Chen, J.; McBride, J. R.; Lian, T., Efficient Hot-Electron Transfer by a Plasmon-Induced Interfacial Charge-Transfer Transition. *Science* **2015**, *349*, 632-635.
41. Gao, S. Y.; Ueno, K.; Misawa, H., Plasmonic Antenna Effects on Photochemical Reactions. *Accounts of Chemical Research* **2011**, *44*, 251-260.
42. Brongersma, M. L.; Halas, N. J.; Nordlander, P., Plasmon-Induced Hot Carrier Science and Technology. *Nat. Nanotechnol.* **2015**, *10*, 25-34.
43. Manjavacas, A.; Liu, J. G.; Kulkarni, V.; Nordlander, P., Plasmon-Induced Hot Carriers in Metallic Nanoparticles. *ACS Nano* **2014**, *8*, 7630-7638.
44. Valenti, M.; Venugopal, A.; Tordera, D.; Jonsson, M. P.; Biskos, G.; Schmidt-Ott, A.; Smith, W. A., Hot Carrier Generation and Extraction of Plasmonic Alloy Nanoparticles. *ACS Photonics* **2017**, *4*, 1146-1152.
45. Tisdale, W. A.; Williams, K. J.; Timp, B. A.; Norris, D. J.; Aydil, E. S.; Zhu, X.-Y., Hot-Electron Transfer from Semiconductor Nanocrystals. *Science* **2010**, *328*, 1543-1547.
46. Gong, T.; Munday, J. N., Materials for Hot Carrier Plasmonics [Invited]. *Optical Materials Express* **2015**, *5*.
47. Brown, A. M.; Sundararaman, R.; Narang, P.; Goddard, W. A.; Atwater, H. A., Nonradiative Plasmon Decay and Hot Carrier Dynamics: Effects of Phonons, Surfaces, and Geometry. *ACS Nano* **2016**, *10*, 957-966.
48. Liu, Y.; Chen, Q.; Cullen, D. A.; Xie, Z.; Lian, T., Efficient Hot Electron Transfer from Small Au Nanoparticles. *Nano Letters* **2020**, *20*, 4322-4329.
49. Habas, S. E.; Yang, P.; Mokari, T., Selective Growth of Metal and Binary Metal Tips on Cds Nanorods. *J. Am. Chem. Soc.* **2008**, *130*, 3294-3295.

Chapter 2. Experimental Methods

2.1 Sample Preparation

2.1.1 Reagents:

Cadmium oxide (CdO, 99.998%), 1-octadecene (ODE, 90%), oleic acid (OA, 90%), sulphur powder (S, 99.999%),Selenium powder(Se, 99.99%), trioctylphosphine oxide (TOPO 99%), trioctylphosphine (TOP, 97%), oleylamine (Ola, 98%), diphenyl ether (99%), platinum(II) acetylacetonate ($Pt(AcAc)_2$, 97%), 1,2-dichlorobezene (99%), 11-mercaptoundecanoic acid (11-MUA, 98%), gold chloride ($AuCl_3$, 99.99%), dodecyldimethylammonium bromide (DDAB, 98%), dodecylamine (DDA, 98%), chloroauric acid hydrated ($HAuCl_4{\cdot}4H_2O$, 99%), sodium borohydride ($NaBH_4$, 98%), hexadecyl trimethyl ammonium chloride (CTAC), were purchased from Sigma Aldrich. 1,2-hexadecanediol, N-hexylphosphonic acid (HPA, 95%), octadecylphosphonic acid (ODPA, 97%) were purchased from TCI chemicals. All chemicals were used without further purification.

2.1.2 Synthesis of CdS Quantum Dots

CdS quantum dots. To prepare the CdS quantum seeds, sulphur solution (0.8 mL, 0.25 mol/L) was injected into a solution containing 60 mg CdO, 6 mL 1-octadecene (ODE) and 0.45 mL oleic acid (OA) at 250 ºC under Ar, and after reacting for 45 seconds, the reaction was quenched by inserting the reaction vessel into a room temperature water bath. The products were washed three times by precipitation with ethanol followed by centrifugation, and finally dispersed in chloroform for later use. The first exciton peak of CdS QD is at around 377 nm.

2.1.3 Synthesis of CdS Nanorods (NRs)

Synthesis of CdS NRs: CdS NRs were synthesized according to a reported seeded-growth method with modifications.[1, 2] In a typical synthesis of CdS NRs, 0.06 g cadmium oxide (CdO), 3 g trioctydlphosphine oxide (TOPO), 0.29 g octadecylphosphonic acid (ODPA), and 0.08 g hexylphosphonic acid (HPA) were added into a 25 mL three-necked flask, which was then degassed under vacuum for 1 h at 150 ºC. After that, the bottle was heated to 350 ºC under argon. Gradually, the mixture in the flask turned into clear solution, indicating the full dissolution of CdO. At this point, 1.8 mL trioctylphosphine (TOP) was injected to the solution. After the temperature of the reaction solution was once again stabilized at 350 ºC, another solution containing sulfur (0.12g S) and CdS quantum dot seeds(~120nmol) in 1.8 mL TOP was injected. After the temperature of the solution recovered to 350 ºC (in ~3-4 min), the reaction was allowed to proceed for another 5 min and then stopped by removing the heating mantle. Products were precipitated out of the reaction crudes by addition of ethanol. The dissolution and precipitation processes were repeated with toluene and ethanol for several times. Finally, the CdS NRs were dispersed in chloroform.

2.1.4 Synthesis of CdS-Au NRs

Au-tipped CdS NRs (CdS-Au NRs) were synthesized according to a reported procedure with slight modifications.[1, 3] Firstly, CdS NRs were dispersed in 3 mL toluene in a sealed vial and purged with Argon gas for 30 min. A gold stock solution was prepared by dissolution of 10 mg gold(III) chloride ($AuCl_3$), 15 mg of dodecyldimethylammonium bromide (DDAB) and 40 mg of dodecylamine (DDA) in 6 mL toluene in another sealed vial and purged with Ar for 1h. The NR-containing vial was placed in an ice bath, into which 2 mL of Au stock solution was injected under vigorous stirring. The vial was irradiated with a Xeon lamp (20 W) to deposit Au tips on one end

of NRs. The CdS NRs-Au heterostructure with different Au sizes were achieved by tuning the illumination time. Usually, the smallest diameter (~1.6 nm) was achieved within 15min. The largest diameter (~5.5 nm) was achieved with 2.5 h. After the desired illumination time, the reaction was stopped and ethanol was added to precipitate CdS-Au NRs. The precipitation process was repeated for several times to remove excessive surfactants.

2.1.5 Synthesis of Au NPs

Synthesis of Au NPs (2.3 nm and 3.5 nm): Au NPs were synthesized according to reported literature with a little modification.[4]10 mL of 75 mM CTAC and 25 μL of 25 mM $HAuCl_4$ were mixed in a vial at room temperature, into which 0.6 mL freshly prepared ice-cold $NaBH_4$ (10 mmol/L) was rapidly injected with vigorously stirring. After the solution turned to brown, within a few seconds, it was stirred slowly for two hours to promote the decomposition of the remaining $NaBH_4$. Then, the solution was cooled in ice water bath to reduce the solubility of CTAC, followed by centrifugation to remove the excess CTAC. The supernatant containing Au particles with diameters of 2.3nm was obtained.

Synthesis of Au nanoparticles (NPs) (6.5 nm): Au NPs were prepared according to a reported literature.[5] Briefly, 6 mL oleylamine was degassed at 120 °C for about 30 minutes and then was cooled down to 50 °C. After injecting 4 mL pre-prepared oleylamine into a three-necked flask containing 20 mg of $AuCl_3$, the temperature of the flask was raised to 90 °C. After 1h, the reaction was stopped by addition of toluene and then precipitated out by addition of ethanol.

2.1.6 Synthesis of CdS-Pt NRs

Pt-tipped NRs were synthesized according to a reported seeded-growth method with modifications. 8 g diphenyl ether, 0.2 mL oleic acid and 0.2mL oleyamine are added in a 50 mL

flask and degassed under 90ºC for 30 min. Then the temperature was raised to 205 ºC under Ar flow. CdS NR solution (OD=2 @460nm with 1 mm pathlength, volume 1 mL) was evaporated and re-dispersed in 1mL 1,2-dichlorobenzene with $Pt(AcAc)_2$. The amount of $Pt(AcAc)_2$ were tuned to achieve different Pt sizes (1.5 mg for $CdSPt_{0.7nm}$, 2.5 mg for $CdSPt_{1.4nm}$, 7 mg for $CdSPt_{2.3nm}$, 10 mg for $CdSPt_{2.5nm}$, 20 mg for $CdSPt_{3.0nm}$). After the injection of dispersion of NRs and $Pt(AcAc)_2$, the reaction was allowed to proceed for 7 min, quenched by a water bath. The crude solution was centrifuged with adding extra ethanol and toluene. The supernatant containing free Pt NPs was discarded and the precipitate was dissolved in toluene. The purification procedure was repeated once. The final product was dispersed in toluene or hexane (~6mL) and stored in glove box.

2.1.7 Ligand exchange of NRs

1 pellet of KOH (~100mg) was dissolved in 10mL water with 15mg 11-MUA. 3mL of this solution was added to CdS-Pt vial. The vial was stirred for 1 h and then stand still for several mins to allow separation into two phases. The aqueous phase was transferred into a centrifuge tube followed by addition of ethanol, precipitation and re-dissolved in water. The purification procedure was repeated once with extra ethanol. The final product was dissolved in water and kept under dark in glove box.

2.2 Time Resolved Spectroscopy Set-up

The femtosecond transient absorption measurements were conducted in a Helios spectrometer (Ultrafast Systems LLC) with pump and probe beams derived from a regenerative amplified Ti: Sapphire laser system (Coherent Astrella, 35 fs, 4 mJ/pulse, and 1 kHz repetition rate). The 800 nm fundamentals are split into two parts. One part of the 800 nm output pulse passed through a

frequency-doubling BBO crystal and generated the 400 nm excitation beam. Another part of the 800 nm beams was attenuated and focused on a CaF_2 window for the generation of the white light continuum, with a wavelength range from 350 nm to 800 nm. The probe beam was focused onto the sample. The transmission of the probe was collected by a fiber optics-coupled multichannel spectrometer with complementary metal-oxide-semiconductor (CMOS) sensors and detected at a frequency of 1 kHz. During the measurement, the pump laser beam was chopped at 500 Hz. The delay between the pump and probe pulses was controlled by a motorized delay stage. The change in absorbance for the pumped and unpumped samples was calculated.

The nanosecond transient absorption spectroscopy was collected with EOS spectrometer (Ultrafast Systems). The 2 kHz probe pulse was generated by STM-2-UV (Leukos) light source. The signals were processed by the same optical instrument and software as the femtosecond setup. Data were processed to generate transient absorption spectra, kinetic graphs.

2.3 Photo-catalytical H_2 production

The photocatalysts were dispersed in Milli-Q water. A total volume of 1.5 mL solution with optical density= 0.3-0.4 at 405 nm was placed in a cylindrical cuvette and 3 mg/mL L-cysteine as hole scavengers. The solution PH was controlled by adding KOH monitored by PH meter. The solution was purged with Argon for 1 min before exposure to LED illumination. The hybrid nanoparticles were then illuminated with 4.7 mW 405nm diode (Thorlabs, CPS405). Aliquots of the reaction vessel head space were taken using a gas tight syringe at different time intervals and detected and quantified using Shimadzu gas chromatograph (GC-2014) equipped with a molecular sieve (5 Å) packed column and a thermal conductivity detector. The resulting chromatograms and hydrogen concentration were obtained by the comparison to a calibration curve of known hydrogen amounts.

References

1. Wu, K.; Rodríguez-Córdoba, W. E.; Yang, Y.; Lian, T., Plasmon-Induced Hot Electron Transfer from the Au Tip to CdS Rod in CdS-Au Nanoheterostructures. *Nano Lett.* **2013,** *13* (11), 5255-5263.
2. Wu, K.; Zhu, H.; Liu, Z.; Rodriguez-Cordoba, W.; Lian, T., Ultrafast charge separation and long-lived charge separated state in photocatalytic CdS-Pt nanorod heterostructures. *J. Am. Chem. Soc.* **2012,** *134* (25), 10337-40.
3. Habas, S. E.; Yang, P.; Mokari, T., Selective Growth of Metal and Binary Metal Tips on CdS Nanorods. *J. Am. Chem. Soc.* **2008,** *130* (11), 3294-3295.
4. Inoue, Y.; Tsutamoto, Y.; Muko, D.; Nanamura, K.; Sawada, T.; Niidome, Y., Stepwise Preparation of Spherical Gold Nanoparticles Passivated with Cationic Amphiphiles. *Anal. Sci.* **2016,** *32* (8), 875-880.
5. Khon, E.; Mereshchenko, A.; Tarnovsky, A. N.; Acharya, K.; Klinkova, A.; Hewa-Kasakarage, N. N.; Nemitz, I.; Zamkov, M., Suppression of the plasmon resonance in Au/CdS colloidal nanocomposites. *Nano Lett.* **2011,** *11* (4), 1792-1709.

Chapter 3. Size- dependent light-driven H_2 generation quantum efficiency of CdS-Pt nanorod

3.1 Introduction

Artificial photosynthesis has attracted enormous research interests in the past decades due to its promise as a renewable energy resource for a sustainable society.[1-5] Among various reported approaches, heterogenous hybrid photocatalysts composed of semiconductor/metal nanoparticle heterostructures are particularly attractive because they combine both the superior light-harvesting of semiconductors and the catalytic properties of metal catalysts.[4-11] The size of catalysts is one of the most important parameters in the design of these systems, because it can significantly affect not only the catalytic activity and selectivity, but also the cost of these systems, especially for precious noble metal catalysts.[12-13] The size dependent catalytic properties of noble metal nanoparticles have been extensively studied under electro- or thermal- catalytic conditions, in the absence of light.[14-19] However, it is unclear to what extent the insight obtained in these dark conditions can be used to guide the design of photocatalysts composed of semiconductor/metal heterostructures. The overall performance of the hybrid photocatalyst depends on the light harvesting properties of the semiconductor domain, charge separation and recombination across the semiconductor/metal interface, and the catalytic activities of the metal nanoparticle.[20-21] The size of the metal catalyst may have complex effects on all these aspects, especially at the sub-nanometer regime where the density of states changes rapidly with size.

The photocatalytic performance of semiconductor/metal hybrid catalysts have been reported to depend on the metal domain size. Many of these studies focus on Pt, one of the most efficient catalysts for water splitting and H_2 evolution,[14-15, 18, 22-23] with significant effort devoted to reducing

the Pt catalyst size from large particles of several nm,[24-25] to small clusters of tens of atoms,[20, 26-28]and, more recently, to the single atom level.[14-15, 29-31] Despite these efforts, mechanistic understanding of the effect of the metal catalyst size remains elusive due in part to the difficulty in designing material systems in which the metal particle number density and sizes can be systematically tuned without affecting the semiconductor or support domain.[20, 26] The recent development of semiconductor-metal hybrid nanorod heterostructures offers unique opportunities to study the size effects of metal catalysts in photocatalysts.[32-35] These structures consist of semiconductor NRs with 1 or 2 metal nanoparticles selectively deposited at the NR tips; and the size of the metal tip can be independently and systematically tuned without changing the NR domain.[32, 34] Using this materials platform, CdS NRs decorated with Au and Ni nanoparticles have been examined to understand the effect of metal particle sizes on their photocatalytic H_2 generation performances.[36-38] These studies are focused on particle sizes from ~ 2 – 10 nm and did not extend into the subnanometer size regime. Furthermore, although Pt is one of the most widely studied and CdS-Pt NRs and nanoplatelets are among the best performing photocatalysts for H_2 generation,[29, 39-41] systematic study of the effect of Pt size on their photocatalytic performance has not been reported.

Here, we utilize CdS-Pt NR heterostructures as a platform to investigate the effect of Pt size on the photocatalytic light-to-H_2 conversion efficiency in small Pt size regimes, from 0.7±0.3 to 3.0±0.8 nm. We first measured the overall light to H_2 conversion efficiencies as a function of Pt particle size under steady-state light illumination. To gain insight into the key efficiency limiting steps, we carried out *in situ* transient absorption (TA) spectroscopic measurement of charge separation and recombination kinetics of these nanorods. We propose a simplified model that divides the overall process into charge separation and water reduction stages, and using this model,

the size dependence of overall light-to-H_2 conversion can be understood by the increase of both the charge separation and water reduction quantum efficiencies at larger Pt sizes. Finally, our analysis suggests that the electron transfer (ET) rate from the CdS to Pt increases at larger Pt size due to the increase of the electronic coupling strength and density of accepting states. Our findings provide important insight into designing semiconductor-metal hybrid photocatalysts with small metal particle sizes.

3.2 Results

3.2.1 CdS NR Characterization

The 1D CdS and CdS-Pt NRs were synthesized according to previous literature procedures with slight modifications (Chapter 2).[32,42] Transmission electron microscope (TEM) measurements (Figure 3.1A) show that the length and diameter of CdS NRs are 26.8±3.1 and 3.7±0.4 nm, respectively. Starting from the same batch of CdS NRs, five CdS-Pt NR samples with Pt tip diameters of 0.7±0.3, 1.4±0.8, 2.3±1.1, 2.5±1.0, and 3.0±0.8 nm were prepared. Their TEM images are shown in Figure 3.1B-F and the histograms of Pt size distributions are shown in Figure A.3.1 and Table A.3.1. The distributions of the number of Pt tips on the NR are also listed in Table A.3.2. These CdS-Pt NR samples are designated as $CdSPt_{xnm}$ with the subscript *x* representing the Pt diameter. All CdS and CdS-Pt NR samples are ligand-exchanged with 11-mercaptoundecanoic acid (MUA) into aqueous solutions by standard methods (See Chapter 2), unless otherwise noted. UV-vis absorption spectra of both CdS and CdS-Pt NRs in water show clear exciton bands with the lowest energy 1Σ exciton band at ~460 nm (Figure 3.1G), determined by quantum confinement in the NR radial direction.[43-44] In comparison, the CdS-Pt NR shows an additional broad absorption feature extending from the near IR into visible region, consistent with the Pt d-sp interband

transition.[45] The absorption spectra of all five CdS-Pt NR samples are well described by the linear combination of the CdS NR and Pt particle absorption features (black dashed lines in Figure 3.1G), indicating that the deposition of Pt has little impact on the electronic transitions of CdS NRs.

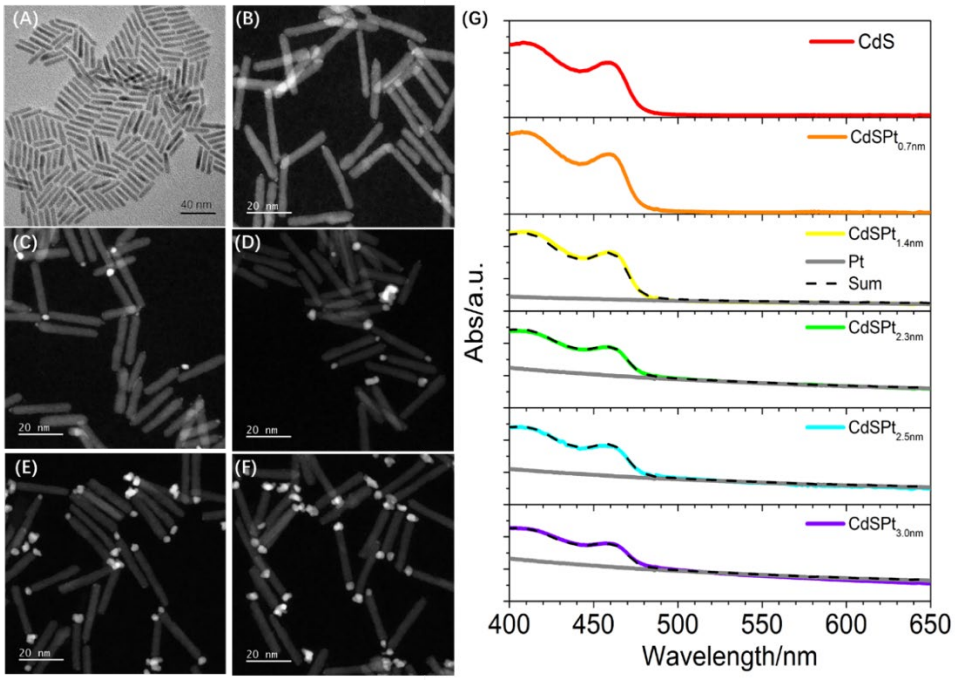

Figure 3.1. TEM images and absorption spectra of CdS and CdS-Pt NRs. (A-F) TEM images of (A) CdS, (B) $CdSPt_{0.7nm}$, (C) $CdSPt_{1.4nm}$, (D) $CdSPt_{2.3nm}$, (E) $CdSPt_{2.5nm}$, and (F) $CdSPt_{3.0nm}$. (G) UV-vis absorption spectra of CdS and CdS-Pt NRs (colored solid lines). Also shown are fits to the CdS-Pt spectra (black dashed lines) by the linear combination of the absorption spectra of isolated Pt particles (grey solid lines) and CdS NRs. This indicates the deposition of Pt has little impact on the CdS exciton bands.

3.2.2 Size-dependent H_2 Production Performance

The size-dependent H_2 production performance of CdS-Pt NRs was evaluated in aqueous solution at pH=12, with 3 mg/mL L-Cysteine as hole scavengers [46] under 405 nm LED illumination

(~100 mW/cm^2). The amount of generated H_2 was quantified by gas chromatography and 3 samplings were averaged for each data point. Here, we compare the H_2 production performance of CdS-Pt NR samples by their internal quantum efficiencies of light to H_2 conversion, $QE_{H_2} = \frac{2n_{H2}}{n_{photon}} * 100\%$ where n_{H_2} and n_{photon} are the number of produced H_2 and absorbed photons by the CdS NRs, respectively; this excludes any performance differences due to the variation of light absorption by different NR samples. The QE_{H_2} of pristine CdS NRs is <0.1%, close to our detection limit. Under the same experimental conditions, much higher QE_{H_2} are observed in CdS-Pt NRs, indicating the importance of Pt catalysts for H_2 production (Figure 3.2, violet circles). With an increase of Pt catalyst size from 0.7±0.3 to 3.0±0.8 nm, the QE_{H_2} of CdS-Pt increases from 0.5±0.2% to 38.3±5.1%, by nearly two orders of magnitude. We have chosen pH 12 for this study because measurements using similar CdS-Pt NRs from pH 7 to 14 shows the highest QE_{H_2} at this pH (Figure A.3.2).

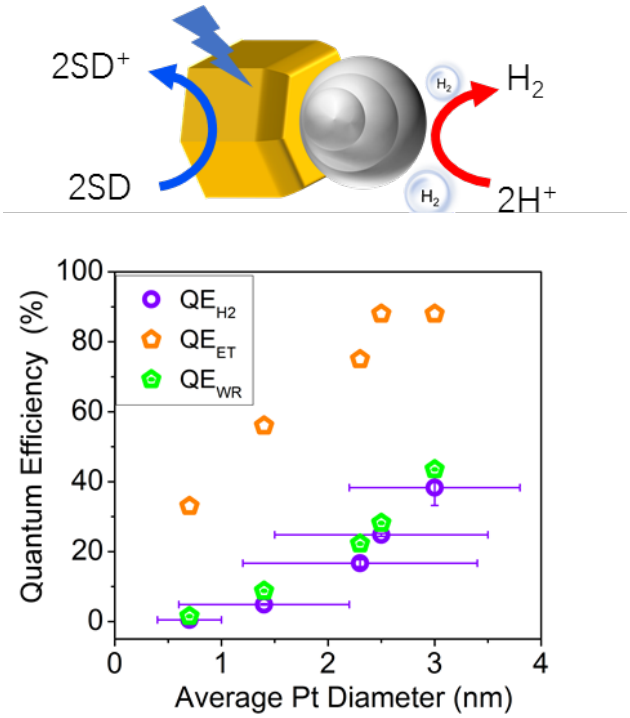

Figure 3.2. Photo-driven H_2 generation by proton reduction using CdS-Pt NRs. (top) Schematic of overall light driven H_2 generation: the overall process of forming one H_2 involves the absorption of two photons by CdS, the reduction of two H^+ on the Pt nanoparticle, and oxidation of 2 sacrificial electron donors (SD, L-cysteine) in solution. (bottom) Photo-driven H_2 production internal quantum efficiency QE_{H_2} of CdS-Pt NRs as a function of the average Pt tip size. Measurement conditions: 405nm LED illumination at ~100 mW/cm^2, pH=12, 3 mg/mL L-cysteine as hole scavengers**.** Also shown is the ET quantum efficiency QE_{ET} determined from transient absorption kinetics and the water reduction quantum efficiency $C * QE_{WR}$ calculated by the ratio of QE_{H_2} and QE_{ET} according to Eq. (3.1).

3.2.3 Charge separation and recombination kinetics

The overall light-to-H_2 conversion processes involves many competing elementary steps.[36] To gain further insight, we utilized TA spectroscopy to directly measure the size dependence of ET kinetics from the CdS NR to Pt tip, following previous reports.[39, 42, 47] TA studies of CdS and CdS-Pt NRs were conducted with 400 nm pulse laser photoexcitation at a fluence of ~2 mW/cm^2. Under this condition, the average exciton number per NR is estimated to be ~0.1-0.2 following previously reported methods, and the measured transient signal is dominated by NRs with one exciton.[48-50] The measurements were conducted under conditions (solution pH and sacrificial donor concentration) that are the same as the H_2 generation efficiency measurement described above (Appendix 3 and Chapter 2), with the exception that the CW LED illumination at 405nm is replaced by pulse laser excitation at 400 nm. The same electrolyte environment is important when making a direct comparison between the photoinduced charge transfer results and photocatalytic performances because the charge transfer rates of photocatalysts depends strongly on the

electrolyte environments.[51-52] The TA spectra of CdS NRs (Figure 3.3A) show two major features: (a) a bleach of 1Σ exciton band (XB) centered at 460 nm due to the electron filling at the conduction band (CB) edge which reduces 1Σ exciton absorption in excited NRs and (b) an photoinduced exciton absorption (XA) at ~425 nm that is attributed to red-shift of a higher energy transitions in excited NRs.[42] Because the XB bleach reflects only the populations of photogenerated CB edge electrons in the CdS NR, its decay probes the recombination of photogenerated electrons with the holes in the NR and/or ET from the NR to Pt. As shown in Figure 3.3D, for bare CdS NRs, the XB decay can be fit to a stretched exponential decay $\Delta A(t) = e^{-\left(\frac{t}{\tau_x}\right)^{\beta}}$, with the time constant τ_x and β of 17±1 ns and 0.40±0.01, respectively, which corresponds to an averaged lifetime of 57±2 ns. This highly non-single-exponential XB decay in bare CdS NRs has been attributed to the recombination of the CB electron with the trapped hole.[42] The TA spectra of selected CdS-Pt NRs, regardless of the Pt size, show similar spectral features as those in CdS NRs, as shown in Figure 3.3B and C for $CdSPt_{0.7nm}$ and $CdSPt_{3.0nm}$, respectively, and in Figure A.3.3 for other samples. However, the XB and XA features decay on a much faster time scale, which is attributed to ET from the CdS CB edge to the Pt tip. With increasing Pt size from 0.7±0.3 nm to 3.0±0.8 nm (Figure 3.3D), the XB half lifetimes reduces progressively from 2.2±0.2 ns to only 8±1 ps, indicating a faster ET from the CdS NR to Pt tip at larger Pt tip size (Table A.3.3).

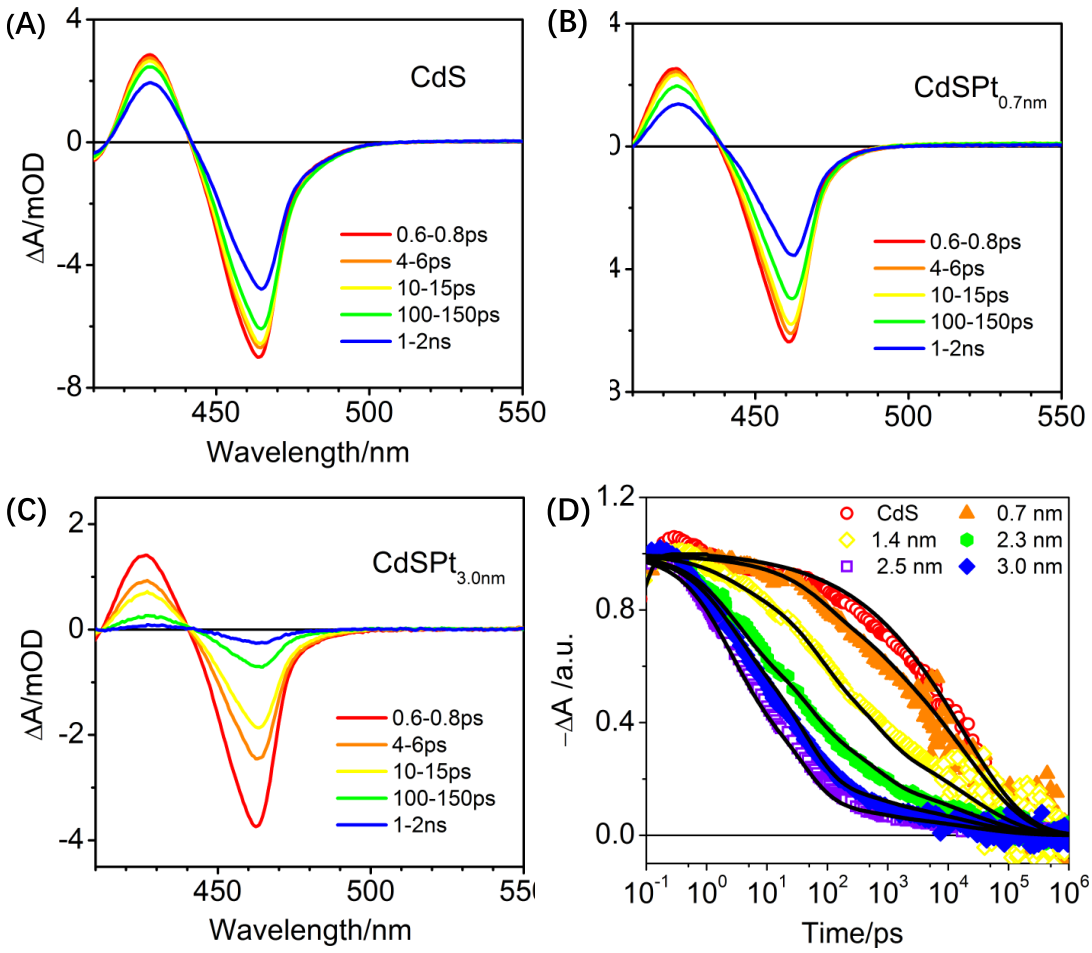

Figure 3.3. Transient absorption spectra and kinetics of CdS and CdS-Pt NRs. Transient absorption spectral evolution of CdS (A), CdS-$Pt_{0.7nm}$ (B) CdS-$Pt_{3.0nm}$ (C) at indicated delay times after 400 nm excitation. For clarity, only averaged spectra in selected time delay windows are plotted. (D) Comparison of the normalized 1Σ exciton bleach recovery kinetics of CdS and 5 CdS-Pt samples (colored symbols) and their fits (solid lines) to a model described in Appendix 4. Faster bleach recovery at larger Pt sizes is attributed to increased ET rates.

Previous studies have shown that in the charge separated state, the presence of holes in the nanorod shifts the exciton transition energy and leads to a derivative like TA feature that can be used to follow the lifetime of charge separated state.[42, 47] Interestingly, with MUA ligand capped

CdS-Pt NRs under light driven H_2 conditions described above, such charge separated state signal was not observed (Figure A.3.4), which likely indicates a fast transfer of the hole to excess L-cysteine molecules in the solution or large dielectric screening by water. To probe the size dependent charge recombination rate, we carried out TA study of CdS-Pt NRs capped with phosphonates in toluene. The transient spectra of phosphonate capped $CdSPt_{2.5nm}$ from 10 ns to 100 μs are compared in Figure A.3.5, which shows characteristic derivative like features of the charge separated state. A comparison of decay kinetics of this charge separated state signal for phosphonate-capped $CdSPt_{1.4nm}$, $CdSPt_{2.3nm}$ $CdSPt_{2.5nm}$ in toluene (Figure A.3.6) shows that the charge recombination kinetics are independent of the Pt size with a half lifetime of ~2.3 μs. Previous studies have shown that the charge recombination is limited by the activation of holes to the valence band (VB) from hole acceptors, which may explain the slow Pt-size independent recombination kinetics.[53] Under the H_2 evolution conditions in water, the trapped holes are rapidly transferred to surface ligand MUA, which likely further slowing down the charge recombination process.

Under the CW illumination conditions of the light-driven H_2 generation measurement shown in Figure 3.2, each NR is estimated to absorb a photon in every 0.4 ms (Appendix 2). Because of the relative slow H_2 evolution rate (about 1.3 ms, estimated from QE_{H_2} of $CdSPt_{3.0nm}$, corresponding to turnover frequency of 770 1/s), there may be accumulation of electrons in the Pt. To examine its effect of charge separation kinetics, we also carried out TA studies with the sample under the same CW illumination conditions used for the H_2 production measurement (Appendix 3). TA spectra of CdS and CdS-Pt NRs samples with (Figure A.3.7) and without (Figure 3.3A-C) CW illumination are similar. The XB bleach of untipped CdS NRs under CW illumination show identical decays as those measured under dark situations (Figure A.3.8, first panel,) which is

consistent with faster electron-hole recombination (~50 ns) compared to photon absorption rate (~0.4 ms). Interestingly, for all CdS-Pt samples, the CdS XB decay become slower in the presence of CW illumination (Table A.3.3), indicative of a slower ET rate. However, because ET lifetimes are still much faster than the intrinsic decay of exciton, the ET efficiencies of CdS-Pt under illumination, calculated using the method to be described below, is only lower by 5-10% than under dark conditions (Figure A.3.9). Such effect does not affect the qualitative understanding of the efficiency limiting factors of the hybrid photocatalyst and will not be discussed further.

3.3. Discussion

3.3.1 Size-dependent efficiencies of charge separation and water reduction

The overall light-driven H_2 generation process in CdS-Pt NRs reduces two protons to H_2 and oxidizes two L-cysteine molecules, with energy provided by the absorption of two photons. This overall process involves multiple competing elementary steps and intermediates as shown in Figure 3.4A and B.[36, 47] Photoexcitation of MUA-capped CdS-Pt NRs generates an exciton in the CdS NR. The VB hole (1.6 V *v.s.* NHE)[54-55] is transferred to a trap state (likely the S dangling bond) on a sub-picosecond time scale to form a trapped exciton in CdS (labelled as L-CdS*-Pt, with L being the MUA ligand).[42, 56] The trapped hole in L-CdS*-Pt is transferred to the MUA ligand (oxidation potential of 0.8 V *v.s.* NHE[57]) with a rate constant k_{HT} of around ~$(100\ ps)^{-1}$ to form L^+-CdS^--Pt; and the hole transfer quantum efficiency (QE_{HT}) is determined by its competition with the electron-hole recombination (k_{CR1}) process within CdS*.[39, 47] Because of the long e-h recombination time (~ 57ns, Figure 3.3D), this process is expected to be of near unity quantum efficiency. The transfer of CB electron (-1.0 eV v.s. NHE) to the Pt tip (with a rate constant k_{ET}) forms a charge separated state (L^+-CdS-Pt^-) and this ET quantum efficiency (QE_{ET}) is determined

by the competition with the charge recombination process in L^+-CdS^--Pt (k_{CR2}). This process occurs on the same time scale as hole transfer in CdS NRs with large Pt and become much slower in NRs with small Pt. Further removal of the hole in the surface ligand to the solution hole scavengers (L-cysteine, 0.1-0.3 eV v.s. NHE),[54, 58] with a rate constant of k_{HS}, forms a long-lived L-CdS-Pt^- species; and the quantum efficiency of this hole scavenging process (QE_{HS}) is limited by the competitive charge recombination in L^+-CdS-Pt^- (k_{CR3}). In the water reduction stage with a quantum efficiency of QE_{WR}, a proton is reduced on L-CdS-Pt^- to form L-CdS-Pt-H (with rate constant k_{WR}). This species can absorb another photon to repeat the process above to produce another Pt-H on the Pt particle and the two adsorbed H atoms diffuse together to form H_2. Alternatively, two L-CdS-Pt-H can find each other in solution to produce H_2. The overall quantum efficiency of the light driven water reduction process is the product of these elementary steps according to Eq. (3.1).

$$QE_{H2} = QE_{HT} * QE_{ET}(d) * QE_{HS} * QE_{WR}(d) = C * QE_{ET}(d) * QE_{WR}(d) \quad (3.1)$$

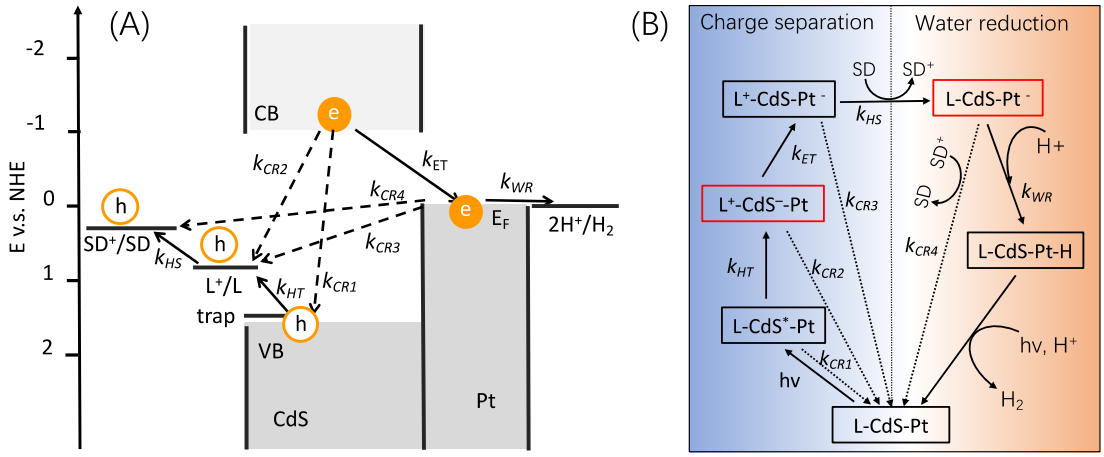

Figure 3.4. (A) Key energy levels and elementary processes and (B) simplified kinetic model with key intermediate states and processes for light driven H_2 generation using L-CdS-Pt nanorods. L indicates the MUA capping ligands on the CdS surface. Forward processes (solid arrows): hole

transfer from the trapped exciton state to surface ligand L (with a rate constant k_{HT}), electron transfer from the CdS to Pt (k_{ET}), hole transfer from the oxidized surface ligand L^+ to hole scavenger SD(k_{HS}), water reduction on reduced Pt particle (k_{WR}). Each process competes with a charge recombination process (k_{CRi}, i=1-4, dashed arrows), which determines the quantum efficiency of the elementary step. The overall quantum efficiency of light drive H_2 generation is the product of the quantum efficiencies of the elementary steps.

Among the four elementary steps, the quantum efficiencies of the ET and water reduction steps are dependent on the Pt particle size. QE_{HT} is independent on the Pt size, as it is determined by the competition of hole transfer from the CdS to surface ligand and electron-hole recombination within CdS. QE_{HS} is determined by the competition of hole transfer from the oxidized ligand L^+ to the scavenger and charge recombination within L^+-CdS-Pt^-. As discussed above, the direct experimental determination of charge recombination in L^+-CdS-Pt^- in water is not feasible due to the lack of associated spectroscopic signatures (Figure A.3.4). TA measurements of CdS-Pt in organic solvent (Figure A.3.5 and A.3.6), corresponding to CdS^+-Pt^-, shows that charge recombination, with a half lifetime of ~2.3 μs, is independent of the Pt size. We assume that charge recombination in L^+-CdS-Pt^-, in which the hole resides in the surface ligand instead of a surface site in CdS^+-Pt^-, should also be independent of the Pt size. This is consistent with the previous finding that charge recombination is determined by the slow rate of hole diffusion on the NR and is likely not sensitive to the Pt size dependent hole transfer step at the Pt/CdS interface.[53] Thus, in Eq. (3.1) we have group the product of the size independent quantum efficiency into a constant C ($= QE_{HT} * QE_{HS}$).

In this simplified kinetic model, we have assumed that the rates of these elementary steps are distinctly different and can be modelled by the sequential kinetics scheme described above. This assumption is justified based on known time constants. For example, the hole transfer from trap states in CdS to the surface ligand L, occurring on the 100 ps time scale, is well separated from the next hole transfer event from the oxidized ligand to hole scavengers in solution on the >> ns time scale. Similarly, while the initial electron transfer from the CdS to Pt is ultrafast (< 1ns time), the reduction of water on Pt and the H_2 evolution processes occurs on the much slower (~1.3 ms) time scale. Thus, it is also informative to divide the overall process into a charge separation stage (with a quantum efficiency of $QE_{CS} = QE_{HT} * QE_{ET}(d) * QE_{HS}$) and a water reduction stage (with a quantum efficiency of QE_{WR}), as shown in Figure 3.4B

The ET QE can be determined from transient absorption kinetics (Figure 3.3D) according to Eq. (3.2).[59]

$$QE_{ET} = 1 + \int_0^\infty dt \frac{dS_{CdS}(t)}{dt} \frac{S_{CdS-Pt}(t)}{S_{CdS}(t)} \quad (3.2)$$

In eq. (3.2), $S_{CdS}(t)$ and $S_{CdS-Pt}(t)$ represents the time dependent probability distribution of the CdS conduction band electron in CdS and CdS-Pt NRs, respectively, which can be obtained from their 1Σ exciton bleach recovery kinetics. The calculated QE_{ET} values for CdS-Pt of different Pt sizes are shown in Figure 3.2 (orange pentagon). From the measured QE_{ET} and QE_{H_2}, $C * QE_{WR}$ can also be calculated according to eq. (3.1), which is also plotted in Figure 3.2.

The result in Figure 3.2 shows that the observed increase of QE_{H_2} with Pt particle sizes results from the size dependence of QE_{ET} and QE_{WR}, both increasing with the Pt particle size. Over the size regime studied, QE_{ET} values are significantly higher than C* QE_{WR}. For example, for $CdSPt_{3.0nm}$ the QE_{ET} is ~88%, while $C * QE_{WR} = QE_{HT} * QE_{HS} * QE_{WR}(d)$ is ~ 44%, leading to a QE_{H_2} efficiency of only 38.3±5.1%. As discussed above, QE_{HT}~ 1, because of much faster hole

transfer rate compared to the trap exciton decay in CdS. Thus, the low overall light to hydrogen conversion efficiency in $CdSPt_{3.0nm}$ can be attributed to small $QE_{HS} * QE_{WR}(d) \sim 44\%$. Photocatalytical H_2 production reactivities of metal-tipped NRs have been reported previously. For CdS-Au NRs, Banin and coworkers observed that the H_2 production rate increases with gold diameters from 1.5±0.2 to 3.0±0.5 nm, followed by a decrease with Au sizes from 4.8±0.7 nm to 6.2±0.8 nm.[36] A similar trend was also found in CdS-Ni NRs, in which Amirav and coworkers reported an optimal diameter of Ni tip at around 5.2 nm within a range of 2.3 nm to 10.1 nm.[37] Our trend of increasing H_2 production quantum efficiencies with the Pt size shown in Figure 3.2 is consistent with these previous reports in the small diameter range (<5 nm).

According to the simplified kinetic model (Figure 3.4) and Figure 3.2, the size dependent QE_{ET} can be attributed to the size-dependent ET rate from the CdS to Pt. The origin of this dependence will be further discussed below. Two factors affecting size-dependent QE_{WR} should be considered: (i) the size dependent water reduction rate, k_{WR}, and (ii) the size dependent recombination between the electrons (e^-) in Pt and with the hole in the oxidized sacrificial donor. The Pt size dependence of this charge recombination process is unclear. If it is assumed to be size independent, our result would suggest higher water reduction rates in larger Pt particles. It has been reported previously that decreasing the Pt size from 3 nm particles to single atoms causes an order of magnitude decrease in the rate of electrocatalytic reduction of water (k_{WR}), which has been attributed to the size dependent of H* absorption energy and its effect on the rate limiting Pt-H formation step.[15] It is possible that the dark electrocatalytic property of Pt size dependence is well encoded into the photoelectrochemical performance, playing an important role in controlling the second stage of the overall photoinduced H_2 generation process (Figure 3.4B).

3.3.2 Size dependent electron transfer from CdS to Pt

As shown in Figure 3.3D, ET rates decrease in CdS-Pt samples with smaller average Pt sizes. According to Figure A.3.1, there is a broad distribution of Pt particle sizes in each CdS-Pt sample. As shown in Figure A.3.10, a normalized comparison of exciton bleach kinetics of samples of different Pt sizes shows that the slow component (10^4-10^6 ps) of all samples are the same as that of CdS NRs without Pt, indicating the presence of a subpopulation that is ET inactive. This ET inactive subpopulation increases in samples with a smaller average Pt tip size. The percentage of this subpopulation is larger than the percentage of untipped nanorods in each sample. For instance, in $CdSPt_{0.7nm}$, about 80% of decay comes from ET inactive nanorods, while only around 30% nanorods are not tipped with small Pt clusters (Table A.3.2). As shown in Figure A.3.11, the subpopulation of ET inactive nanorods is consistent with subpopulations of untipped nanorods and nanorods with Pt particles smaller than 1 nm. This indicates extreme slow ET into small Pt clusters, which cannot compete with the intrinsic exciton recombination in CdS NRs. The kinetics of exciton bleach recovery in the CdS-Pt samples can be fit according to a model that accounts for the Pt size dependent ET rates, as described in Appendix 4. The best fit according to this model is shown in Figure 3.3D and the resulting size dependent ET times for Pt size >1 nm are shown in Figure 3.5. The plot of the logarithm of electron transfer lifetime vs Pt diameter shows a linear dependence with a slope of -5.6±0.6, indicating that the electron transfer lifetime scales with the diameter (d) of the Pt particle as $d^{-5.6}$.

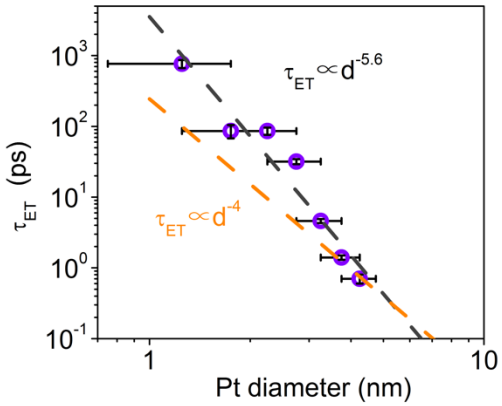

Figure 3.5. Estimated size-dependent electron transfer from 1 nm to 4 nm used in fitting of the kinetics shown in Figure 3.3D. Logarithm plot indicates a power law between size and electron transfer rates. The linear fit of slope equals -5.6±0.6. Also shown is $\tau_{ET} \propto d^{-4}$ according to the model described by Eq.(3.3).

The model for describing electron transfer from the CdS nanorod to the Pt tip remains unclear. This process can involve direct one-step tunneling of the electron from the trapped exciton state to the Pt. Alternatively, it can involve indirect activated diffusion process that consists of several steps: (i) electron ionization from the hole, (ii) diffusive transport of the electron to the CdS/Pt interface in the CdS, (iii) finally, the electron transfer across the CdS/Pt interface. The five CdS-Pt samples are prepared using the same CdS rod, which suggest they should have the same rates for the first and second steps. Thus, only the last step depends on the size of the Pt and varies in these samples. Within the activated diffusion model, the observation of the $d^{-5.6}$ dependence of the ET time (Figure 3.3D and Figure 3.5) suggest that the ET rate is limited by the interfacial transfer step. Thus, in both models, the effective interfacial electron transfer rate can be described by the Fermi's golden rule as shown in eq. 3.3:[60]

$$k_{ET} = \frac{2\pi}{\hbar}\rho(E)|H(E)|^2 \quad (3.3)$$

$\rho(E)$ represents the density of states in the metal acceptors and can be expressed as $\rho(E) = V\frac{(2m_e^*)^{3/2}}{2\pi\hbar^3}\sqrt{E} \propto d^3\sqrt{E}$, with E being the energy difference between the CdS conduction band edge and the Pt sp band bottom. For large Pt particles, the CB states in Pt is continuous and E is nearly size-independent, which suggests that $\rho(E)$ scales with d^3. $|H(E)|^2$ is the modular square of the transition matrix from the initial state in the CdS CB to the final state in Pt. Within the tight binding model, the coupling strength is determined by the first layer of Pt atoms that are in contact with the CdS. Thus, $H(E)$ should be proportional to the number of Pt atoms at the interface, which scales with d^2, and the contribution of each interfacial Pt atom to a k state within the Pt, which scales with $1/\sqrt{N} \sim 1/\sqrt{d^3}$. These factors combine to lead to $|H(E)|^2 \sim d$. According to eq. (3.3), the electron transfer rate from the CdS to Pt should scale with d^4, or $\tau_{ET} \sim d^{-4}$, which is close to experimentally observed size dependence shown in Figure 3.5. Such steep dependence of ET rates on Pt diameter is consistent with the lack of ET activity in NRs with small Pt clusters. Previously, $|H(E)|^2$ for ET from the CdSe rod to the Au tip is assumed to be independent of the Pt size.[36] This assumption is likely more valid when the size of the Pt exceeds the diameter of the CdS NRs and the contact area become independent of the Pt size. It should also be noted that the d^{-4} dependence is based on the assumption of continuous density of states in the Pt, which is likely not applicable for small Pt clusters with discrete conduction band states.

3.3.3 Key parameters for hybrid semiconductor/metal photocatalysts

Our findings provide important insight into designing photocatalysts that are based on semiconductor/metal catalyst hybrid materials. In general, both the quantum efficiencies for charge separation (including electron transfer, hole transfer, and hole scavenging) and catalytic reaction

should be optimized to improve the quantum efficiency of overall light driven reactions. In CdS-Pt nanorods, increasing the Pt size in the 1 - 4 nm size regime improves the catalyst performance by enhancing both the electron transfer of water reduction quantum efficiencies. In recent years, single atom or small cluster catalysis have received intense interest because of their high catalytic activity and cost-effectiveness. Our result shows that in CdS-Pt nanorods, the rate of electron transfer into <1 nm Pt cluster is too slow to compete with the electron-hole recombination due to the steep decrease of the electron transfer rate with the particles size ($d^{-5.6}$). Thus, significant challenges remain in designing efficient photocatalysts based on single atom or small cluster catalysts. First, the electron transfer rate into such small clusters should be improved. This can be done by shortening charge migration distance and increasing the interaction strength between metal and semiconductor support.[30] Second, the catalytical performance of small clusters on the semiconductor should be optimized, e.g. by changing the surface Pt^{2+}/Pt^0 ratio[25, 61], the surface indexes of Pt[62], and the surface ligands on Pt. Future work that focuses on improving the surface chemistry of small Pt clusters would be important for developing efficient photocatalytic systems with a catalyst loading approaching single atoms. Finally, slowing down charge recombination processes through better design of nanostructures and coupling to faster oxidation processes will be essential to increasing the charge separation and water reduction efficiencies for smaller Pt clusters.

3.4. Conclusion

We have investigated the mechanism by which the Pt particle size affects the photocatalytic light-to-H_2 conversion efficiency of CdS-Pt nanorod heterostructures, a model system for hybrid semiconductor/metal photocatalysts. We observed that the light-to-H_2 conversion efficiency QE_{H2} increases from 0.5±0.2% to 38.3±5.1% when the average Pt particle size increases from 0.7±0.3

to 3.0 ±0.8 nm. The light-to-H_2 generation process involves multiple elementary forward (electron transfer, hole transfer, hole scavenging and proton reduction) and backward charge recombination steps, and their competitions determines the quantum efficiencies of the elementary steps and overall process. We propose a simplified kinetic model in which the overall light driven H_2 generation quantum efficiency is the product of the quantum efficiencies of four key steps: $QE_{H2} = QE_{HT} * QE_{ET}(d) * QE_{HS} * QE_{WR}(d)$. To gain insight into the key Pt size dependent steps, we carried out *in situ* transient absorption measurement of charge separation of these nanorods under the same conditions as H_2 generation measurements. Both the rate and quantum efficiency of electron transfer from the CdS to Pt increase with the average Pt particle size. Our analysis suggests that QE_{ET} increases from 33% to 88% and the quantum efficiency of the remaining steps $C * QE_{WR}(d)$ increases from 2% to 44% when the average Pt particle size increases from 0.7±0.3 to 3.0 ±0.8 nm. The latter change is caused by the size dependence of $QE_{WR}(d)$ because C=$QE_{HT} * QE_{HS}$ is independent on the Pt size. The increase in the former can be attributed to faster electron transfer in larger Pt particle sizes and the increase in the latter may reflect faster water reduction rates in larger Pt particles. The increases of both electron transfer and water reduction quantum efficiencies account for the observed increase of overall light-to-H_2 generation quantum efficiency in nanorods with larger Pt sizes. Detailed analyses of electron transfer kinetics that account for the Pt tip size distribution reveal that the ET rate increases with the Pt diameter according to $d^{5.6\pm0.6}$ and reflect the size dependences of the electronic coupling strength between the CdS and Pt and the density of ET accepting states in Pt.

Our findings suggest that efficient hybrid semiconductor/metal photocatalysts require both efficient light driven charge separation from the semiconductor to the metal and fast catalysts to reduce the charge recombination loss. The observed steep decrease of interfacial charge transfer

rate from the CdS to Pt at small particle sizes suggests significant challenges in designing efficient photocatalysts based on single atom or small cluster catalysts. In addition to increasing the catalytic rate of small clusters, efficient photocatalysts also require schemes to enhance forward charge transfer rates and suppress multiple charge recombination processes in the overall photocatalytic system.

References

1. Gust, D.; Moore, T. A.; Moore, A. L., Solar Fuels Via Artificial Photosynthesis. *Acc. Chem. Res.* **2009**, *42*, 1890-1898.
2. Meyer, T. J., Chemical Approaches to Artificial Photosynthesis. *Acc. Chem. Res.* **1989**, *22*, 163-170.
3. Tachibana, Y.; Vayssieres, L.; Durrant, J. R., Artificial Photosynthesis for Solar Water-Splitting. *Nat. Photon.* **2012**, *6*, 511-518.
4. Kudo, A.; Miseki, Y., Heterogeneous Photocatalyst Materials for Water Splitting. *Chem. Soc. Rev.* **2009**, *38*, 253-278.
5. Kranz, C.; Wachtler, M., Characterizing Photocatalysts for Water Splitting: From Atoms to Bulk and from Slow to Ultrafast Processes. *Chem. Soc. Rev.* **2021**, *50*, 1407-1437.
6. Wu, K.; Lian, T., Quantum Confined Colloidal Nanorod Heterostructures for Solar-to-Fuel Conversion. *Chem. Soc. Rev.* **2016**, *45*, 3781-810.
7. Maeda, K.; Domen, K., Photocatalytic Water Splitting: Recent Progress and Future Challenges. *J. Phys. Chem. Lett.* **2010**, *1*, 2655-2661.
8. Li, X.-B.; Tung, C.-H.; Wu, L.-Z., Semiconducting Quantum Dots For artificial Photosynthesis. *Nature Reviews Chemistry* **2018**, *2*, 160-173.
9. Li, X. B.; Xin, Z. K.; Xia, S. G.; Gao, X. Y.; Tung, C. H.; Wu, L. Z., Semiconductor Nanocrystals for Small Molecule Activation Via Artificial Photosynthesis. *Chem Soc Rev* **2020**, *49*, 9028-9056.
10. Cheng, L.; Xiang, Q.; Liao, Y.; Zhang, H., Cds-Based Photocatalysts. *Energy & Environmental Science* **2018**, *11*, 1362-1391.
11. Somers, R. C.; Bawendi, M. G.; Nocera, D. G., Cdse Nanocrystal Based Chem-/Bio- Sensors. *Chem Soc Rev* **2007**, *36*, 579-91.
12. Roduner, E., Size Matters: Why Nanomaterials Are Different. *Chem. Soc. Rev.* **2006**, *35*, 583-592.
13. Zou, X.; Zhang, Y., Noble Metal-Free Hydrogen Evolution Catalysts for Water Splitting. *Chem. Soc. Rev.* **2015**, *44*, 5148-5180.
14. Cheng, N., et al., Platinum Single-Atom and Cluster Catalysis of the Hydrogen Evolution Reaction. *Nat. Commun.* **2016**, *7*, 13638.
15. Zhou, M.; Bao, S.; Bard, A. J., Probing Size and Substrate Effects on the Hydrogen Evolution Reaction by Single Isolated Pt Atoms, Atomic Clusters, and Nanoparticles. *J. Am. Chem. Soc.* **2019**, *141*, 7327-7332.

16. Cao, S.; Tao, F. F.; Tang, Y.; Li, Y.; Yu, J., Size- and Shape-Dependent Catalytic Performances of Oxidation and Reduction Reactions on Nanocatalysts. *Chem. Soc. Rev.* **2016**, *45*, 4747-4765.
17. Zheng, Y.; Jiao, Y.; Jaroniec, M.; Qiao, S. Z., Advancing the Electrochemistry of the Hydrogen-Evolution Reaction through Combining Experiment and Theory. *Angew. Chem. Int. Ed.* **2015**, *54*, 52-65.
18. Quinson, J., et al., Investigating Particle Size Effects in Catalysis by Applying a Size-Controlled and Surfactant-Free Synthesis of Colloidal Nanoparticles in Alkaline Ethylene Glycol: Case Study of the Oxygen Reduction Reaction on Pt. *ACS Catal.* **2018**, *8*, 6627-6635.
19. Zhu, J.; Yang, M.-L.; Yu, Y.; Zhu, Y.-A.; Sui, Z.-J.; Zhou, X.-G.; Holmen, A.; Chen, D., Size-Dependent Reaction Mechanism and Kinetics for Propane Dehydrogenation over Pt Catalysts. *ACS Catal.* **2015**, *5*, 6310-6319.
20. Schweinberger, F. F., et al., Cluster Size Effects in the Photocatalytic Hydrogen Evolution Reaction. *J. Am. Chem. Soc.* **2013**, *135*, 13262-13265.
21. Karakus, M.; Sung, Y.; Wang, H. I.; Mics, Z.; Char, K.; Bonn, M.; Cánovas, E., Correlating Carrier Dynamics and Photocatalytic Hydrogen Generation in Pt Decorated Cdse Tetrapods as a Function of Cocatalyst Size. *J. Phys. Chem. C* **2017**, *121*, 13070-13077.
22. Imaoka, T.; Akanuma, Y.; Haruta, N.; Tsuchiya, S.; Ishihara, K.; Okayasu, T.; Chun, W. J.; Takahashi, M.; Yamamoto, K., Platinum Clusters with Precise Numbers of Atoms for Preparative-Scale Catalysis. *Nat. Commun.* **2017**, *8*, 688.
23. Dong, C.; Lian, C.; Hu, S.; Deng, Z.; Gong, J.; Li, M.; Liu, H.; Xing, M.; Zhang, J., Size-Dependent Activity and Selectivity of Carbon Dioxide Photocatalytic Reduction over Platinum Nanoparticles. *Nat. Commun.* **2018**, *9*, 1252.
24. Wei, Y.; Jiao, J.; Zhao, Z.; Zhong, W.; Li, J.; Liu, J.; Jiang, G.; Duan, A., 3d Ordered Macroporous Tio2-Supported Pt@Cds Core–Shell Nanoparticles: Design, Synthesis and Efficient Photocatalytic Conversion of Co2 with Water to Methane. *J. Mater. Chem. A* **2015**, *3*, 11074-11085.
25. Kim, G. J.; Kwon, D. W.; Hong, S. C., Effect of Pt Particle Size and Valence State on the Performance of Pt/Tio2 Catalysts for Co Oxidation at Room Temperature. *J. Phys. Chem. C* **2016**, *120*, 17996-18004.
26. Sung, Y.; Lim, J.; Koh, J. H.; Hill, L. J.; Min, B. K.; Pyun, J.; Char, K., Uniform Decoration of Pt Nanoparticles on Well-Defined Cdse Tetrapods and the Effect of Their Pt Cluster Size on Photocatalytic H2 Generation. *CrystEngComm* **2015**, *17*, 8423-8427.
27. Berr, M.; Vaneski, A.; Susha, A. S.; Rodríguez-Fernández, J.; Döblinger, M.; Jäckel, F.; Rogach, A. L.; Feldmann, J., Colloidal Cds Nanorods Decorated with Subnanometer Sized Pt Clusters for Photocatalytic Hydrogen Generation. *Appl. Phys. Lett.* **2010**, *97*, 093108.
28. Crampton, A. S.; Rotzer, M. D.; Ridge, C. J.; Schweinberger, F. F.; Heiz, U.; Yoon, B.; Landman, U., Structure Sensitivity in the Nonscalable Regime Explored Via Catalysed Ethylene Hydrogenation on Supported Platinum Nanoclusters. *Nat Commun* **2016**, *7*, 10389.
29. Li, X.; Bi, W.; Zhang, L.; Tao, S.; Chu, W.; Zhang, Q.; Luo, Y.; Wu, C.; Xie, Y., Single-Atom Pt as Co-Catalyst for Enhanced Photocatalytic H2 Evolution. *Adv. Mater.* **2016**, *28*, 2427-2431.
30. Gao, C.; Low, J.; Long, R.; Kong, T.; Zhu, J.; Xiong, Y., Heterogeneous Single-Atom Photocatalysts: Fundamentals and Applications. *Chem. Rev.* **2020**, *120*, 12175-12216.
31. Liu, L.; Corma, A., Metal Catalysts for Heterogeneous Catalysis: From Single Atoms to Nanoclusters and Nanoparticles. *Chem. Rev.* **2018**, *118*, 4981-5079.

32. Carbone, L.; Kudera, S.; Giannini, C.; Ciccarella, G.; Cingolani, R.; Cozzoli, P. D.; Manna, L., Selective Reactions on the Tips of Colloidal Semiconductor Nanorods. *J. Mater. Chem.* **2006**, *16*, 3952-3956.
33. Schlicke, H.; Ghosh, D.; Fong, L. K.; Xin, H. L.; Zheng, H.; Alivisatos, A. P., Selective Placement of Faceted Metal Tips on Semiconductor Nanorods. *Angew. Chem. Int. Ed.* **2013**, *52*, 980-982.
34. Habas, S. E.; Yang, P.; Mokari, T., Selective Growth of Metal and Binary Metal Tips on Cds Nanorods. *J. Am. Chem. Soc.* **2008**, *130*, 3294-3295.
35. Wächtler, M.; Kalisman, P.; Amirav, L., Charge-Transfer Dynamics in Nanorod Photocatalysts with Bimetallic Metal Tips. *J. Phys. Chem. C* **2016**, *120*, 24491-24497.
36. Ben-Shahar, Y.; Scotognella, F.; Kriegel, I.; Moretti, L.; Cerullo, G.; Rabani, E.; Banin, U., Optimal Metal Domain Size for Photocatalysis with Hybrid Semiconductor-Metal Nanorods. *Nat. Commun.* **2016**, *7*, 10413.
37. Nakibli, Y.; Mazal, Y.; Dubi, Y.; Wachtler, M.; Amirav, L., Size Matters: Cocatalyst Size Effect on Charge Transfer and Photocatalytic Activity. *Nano Lett.* **2018**, *18*, 357-364.
38. Ben-Shahar, Y.; Philbin, J. P.; Scotognella, F.; Ganzer, L.; Cerullo, G.; Rabani, E.; Banin, U., Charge Carrier Dynamics in Photocatalytic Hybrid Semiconductor-Metal Nanorods: Crossover from Auger Recombination to Charge Transfer. *Nano Lett.* **2018**, *18*, 5211-5216.
39. Li, Q.; Zhao, F.; Qu, C.; Shang, Q.; Xu, Z.; Yu, L.; McBride, J. R.; Lian, T., Two-Dimensional Morphology Enhances Light-Driven H2 Generation Efficiency in Cds Nanoplatelet-Pt Heterostructures. *J. Am. Chem. Soc.* **2018**, *140*, 11726-11734.
40. Amirav, L.; Alivisatos, A. P., Photocatalytic Hydrogen Production with Tunable Nanorod Heterostructures. *J. Phys. Chem. Lett.* **2010**, *1*, 1051-1054.
41. Vamvasakis, I.; Liu, B.; Armatas, G. S., Size Effects of Platinum Nanoparticles in the Photocatalytic Hydrogen Production over 3d Mesoporous Networks of Cds and Pt Nanojunctions. *Advanced Functional Materials* **2016**, *26*, 8062-8071.
42. Wu, K.; Zhu, H.; Liu, Z.; Rodriguez-Cordoba, W.; Lian, T., Ultrafast Charge Separation and Long-Lived Charge Separated State in Photocatalytic Cds-Pt Nanorod Heterostructures. *J. Am. Chem. Soc.* **2012**, *134*, 10337-10340.
43. Shabaev, A.; Efros, A. L., 1d Exciton Spectroscopy of Semiconductor Nanorods. *Nano Lett.* **2004**, *4*, 1821-1825.
44. Efros, A. L.; Rosen, M., The Electronic Structure of Semiconductor Nanocrystals. *Annu. Rev. Mater. Sci.* **2000**, *30*, 475-521.
45. Henglein, A.; Ershov, B. G.; Malow, M., Absorption Spectrum and Some Chemical Reactions of Colloidal Platinum in Aqueous Solution. *J. Phys. Chem.* **1995**, *99*, 14129-14136.
46. Sakimoto, K. K.; Wong, A. B.; Yang, P., Self-Photosensitization of Nonphotosynthetic Bacteria for Solar-to-Chemical Production. *Science* **2016**, *351*, 74-77.
47. Wu, K.; Chen, Z.; Lv, H.; Zhu, H.; Hill, C. L.; Lian, T., Hole Removal Rate Limits Photodriven H2 Generation Efficiency in Cds-Pt and Cdse/Cds-Pt Semiconductor Nanorod-Metal Tip Heterostructures. *J. Am. Chem. Soc.* **2014**, *136*, 7708-7716.
48. Zhu, H.; Song, N.; Rodriguez-Cordoba, W.; Lian, T., Wave Function Engineering for Efficient Extraction of up to Nineteen Electrons from One Cdse/Cds Quasi-Type Ii Quantum Dot. *J. Am. Chem. Soc.* **2012**, *134*, 4250-4257.
49. Zhu, H.; Lian, T., Wavefunction Engineering in Quantum Confined Semiconductor Nanoheterostructures for Efficient Charge Separation and Solar Energy Conversion. *Energy Environ. Sci.* **2012**, *5*, 9406-9418.

50. Liu, Y.; Cullen, D. A.; Lian, T., Slow Auger Recombination of Trapped Excitons Enables Efficient Multiple Electron Transfer in 1d Cds-Pt Heterostructure. *Under review* **2021**.
51. Berr, M. J.; Vaneski, A.; Mauser, C.; Fischbach, S.; Susha, A. S.; Rogach, A. L.; Jackel, F.; Feldmann, J., Delayed Photoelectron Transfer in Pt-Decorated Cds Nanorods under Hydrogen Generation Conditions. *Small* **2012**, *8*, 291-297.
52. Yang, W.; Godin, R.; Kasap, H.; Moss, B.; Dong, Y.; Hillman, S. A. J.; Steier, L.; Reisner, E.; Durrant, J. R., Electron Accumulation Induces Efficiency Bottleneck for Hydrogen Production in Carbon Nitride Photocatalysts. *J. Am. Chem. Soc.* **2019**, *141*, 11219-11229.
53. Utterback, J. K.; Grennell, A. N.; Wilker, M. B.; Pearce, O. M.; Eaves, J. D.; Dukovic, G., Observation of Trapped-Hole Diffusion on the Surfaces of Cds Nanorods. *Nat. Chem.* **2016**, *8*, 1061-1066.
54. Yang, W., et al., Surface-Ligand "Liquid" to "Crystalline" Phase Transition Modulates the Solar H2 Production Quantum Efficiency of Cds Nanorod/Mediator/Hydrogenase Assemblies. *ACS Appl. Mater. Interfaces* **2020**, *12*, 35614-35625.
55. Simon, T., et al., Redox Shuttle Mechanism Enhances Photocatalytic H2 Generation on Ni-Decorated Cds Nanorods. *Nat. Mater.* **2014**, *13*, 1013-1018.
56. Cline, R. P.; Utterback, J. K.; Strong, S. E.; Dukovic, G.; Eaves, J. D., On the Nature of Trapped-Hole States in Cds Nanocrystals and the Mechanism of Their Diffusion. *J. Phys. Chem. Lett.* **2018**, *9*, 3532-3537.
57. Brown, K. A.; Wilker, M. B.; Boehm, M.; Dukovic, G.; King, P. W., Characterization of Photochemical Processes for H2 Production by Cds Nanorod-[Fefe] Hydrogenase Complexes. *J. Am. Chem. Soc.* **2012**, *134*, 5627-5636.
58. Sornambikai, S.; Abdul Kadir, M. R.; Kumar, A. S.; Ponpandian, N.; Viswanathan, C., Selective and Low Potential Electrocatalytic Oxidation and Sensing of L-Cysteine Using Metal Impurity Containing Carbon Black Modified Electrode. *Anal. Methods* **2017**, *9*, 6791-6800.
59. Utterback, J. K.; Wilker, M. B.; Mulder, D. W.; King, P. W.; Eaves, J. D.; Dukovic, G., Quantum Efficiency of Charge Transfer Competing against Nonexponential Processes: The Case of Electron Transfer from Cds Nanorods to Hydrogenase. *J. Phys. Chem. C* **2018**, *123*, 886-896.
60. Canovas, E.; Moll, P.; Jensen, S. A.; Gao, Y.; Houtepen, A. J.; Siebbeles, L. D.; Kinge, S.; Bonn, M., Size-Dependent Electron Transfer from Pbse Quantum Dots to Sno2 Monitored by Picosecond Terahertz Spectroscopy. *Nano Lett.* **2011**, *11*, 5234-5239.
61. Wang, Y.; Wang, Y.; Xu, R., Photochemical Deposition of Pt on Cds for H2 Evolution from Water: Markedly Enhanced Activity by Controlling Pt Reduction Environment. *J. Phys. Chem. C* **2013**, *117*, 783-790.
62. Wang, H.; Gu, X.-K.; Zheng, X.; Pan, H.; Zhu, J.; Chen, S.; Cao, L.; Li, W.-X.; Lu, J., Disentangling the Size-Dependent Geometric and Electronic Effects of Palladium Nanocatalysts Beyond Selectivity. *Sci. Adv.* **2019**, *5*, eaat6413.

Appendix 1

Size-distribution of Pt tips

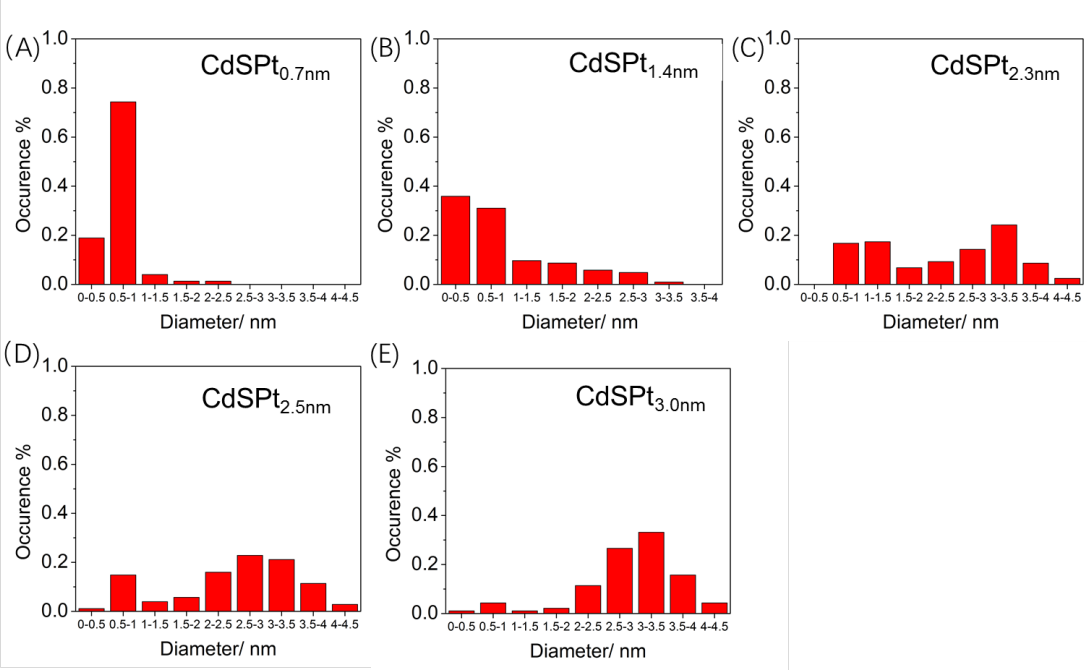

Figure A.3.1. Pt tip diameter distribution of (A) $CdSPt_{0.7nm}$ (B) $CdSPt_{1.4nm}$ (C) $CdSPt_{2.3nm}$ (D) $CdSPt_{2.5nm}$ (E) $CdSPt_{3.0nm}$. Each interval represents 0.5 nm. Non-tipped nanorod is not included in 0-0.5 nm.

Table A.3.1. Size distribution of the Pt sizes in CdS-Pt, as shown in Figure A.3.1.

j	d/nm	$CdSPt_{0.7nm}$	$CdSPt_{1.4nm}$	$CdSPt_{2.3nm}$	$CdSPt_{2.5nm}$	$CdSPt_{3.0nm}$
1	0-0.5	0.19	0.03	0.00	0.01	0.01
2	0.5-1	0.74	0.36	0.17	0.15	0.04
3	1-1.5	0.04	0.31	0.17	0.04	0.01
4	1.5-2	0.01	0.10	0.07	0.06	0.02
5	2-2.5	0.01	0.09	0.09	0.16	0.11
6	2.5-3	0.00	0.06	0.14	0.23	0.27
7	3-3.5	0.00	0.05	0.24	0.21	0.33

8	3.5-4	0.00	0.01	0.09	0.11	0.16
9	4-4.5	0.00	0.00	0.02	0.03	0.04

Non-tipped (d=0) is **not included** in this Table.

Table A.3.2. Percentage of singly-tipped, doubly-tipped and non-tipped nanorods.

	CdSPt0.7nm	CdSPt1.4nm	CdSPt2.3nm	CdSPt2.5nm	CdSPt3.0nm
Single	70%	85%	84%	71%	58%
Double	0%	5%	8%	20%	40%
Zero	30%	10%	8%	9%	2%

Appendix 2

Photo-catalytical H_2 production

As previously reported, the H_2 production quantum efficiency (QE) is determined by the hole removal by the hole scavenger (HS) and solution pH. L-cysteine has been used as a conventional hole scavenger in many H_2 production system. pH is optimized with L-cysteine as hole scavenger. Due to sample limitation, the optimization is carried out with another CdS NR with similar rod diameter and absorption, but slight longer rod length ~37 nm. pH 7 and 10 buffers were controlled by NaH_2PO_4/Na_2HPO_4 and $NaHCO_3/Na_2CO_3$, respectively. pH 12 and 14 were obtained by adding KOH. All solutions contain hole scavenger 3 mg/mL L-cysteine.

As shown in Figure A.3.2, pH 10 and 12 shows relatively higher quantum efficiency than pH 7 and pH 14. pH12 is chosen due to the highest efficiency achieved. Thus, the following H_2 production are conducted under condition of pH 12 and 3 mg/mL L-cysteine in Argon atmosphere. The pH 12 is achieved by adding KOH solution (30 mg/mL) dropwise into 3 mg/mL L-cysteine (pH~6) and monitored by a pH meter.

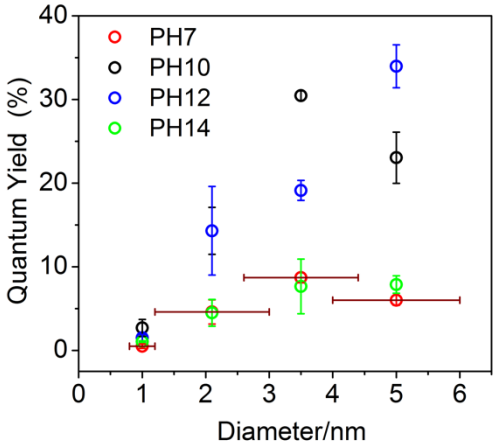

Figure A.3.2. pH-dependent H_2 production QE for sizes from 1-5 nm.

Estimate the arrival time of photons under LED illumination.

The average time for one NR absorbing one photon is estimated to be ~400 μs. The solution OD at 350 nm is ~0.4 in a cell with 1 cm pathlength. The extinction coefficient of NR at 350nm is $2.8*10^{25}$*volume $M^{-1}cm^{-1}$. The concentration of the NR is ~0.04 nmol/mL. The 405nm LED power is 4.7 mW ($9.6*10^{15}$ photons/s) with a beam size of 3.8 mm*1.8 mm=0.05 cm^2. The average photon absorption frequency by a NR is $9.6*10^{15}/(0.05*0.04*10^{-9}*6.02*10^{23})$*Absorption of CdS (~30%)~2500 (1/s), which corresponds to an absorption frequency of one photon per 400 μs.

Appendix 3

Charge separation kinetics

Table A.3.3. Half lifetime of electron transfer ($\tau_{\frac{1}{2}}$/ps) in CdSPt samples measured with (light) and without (dark) CW illumination

	$CdSPt_{0.7nm}$	$CdSPt_{1.4nm}$	$CdSPt_{2.3nm}$	$CdSPt_{2.5nm}$	$CdSPt_{3.0nm}$
dark	2198±200	197±50	32±5	12±5	8±1
light	2800±200	397±50	57±5	27±5	15±1

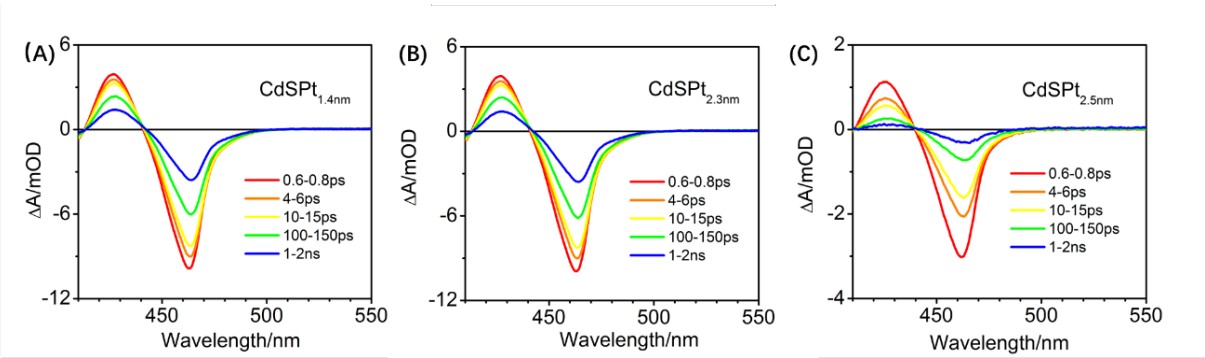

Figure A.3.3. Transient absorption spectral evolution of CdS-Pt NRs. (A) $CdSPt_{1.4nm}$, (B)$CdSPt_{2.3nm}$, (C)$CdSPt_{2.5nm}$.

Charge recombination kinetics in CdS-Pt.

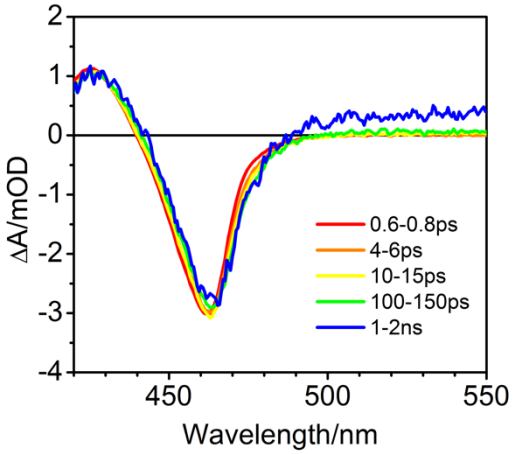

Figure A.3.4. Normalized transient absorption spectra of $CdSPt_{2.5nm}$ in aqueous solution (pH=12, 3mg/mL L-cysteine) at different time delays. The shape of the spectra remains same indicates no charge separation state signal even with electron transfer.

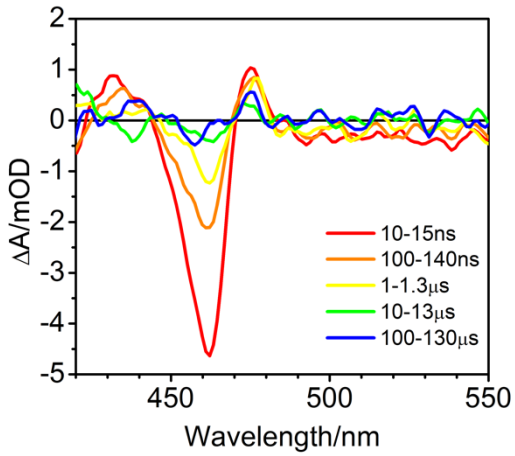

Figure A.3.5. Normalized transient absorption spectra of phosphonates capped $CdSPt_{2.5nm}$ in toluene. The derivative feature at 470 nm indicates the formation of charge separation state. This signal is attributed to shift of exciton transition energy caused by the hole in CdS. The lack of this signal in Figure A.3.4 may indicate ultrafast hole removal from the L-cysteine on surface or large dielectric screening by water.

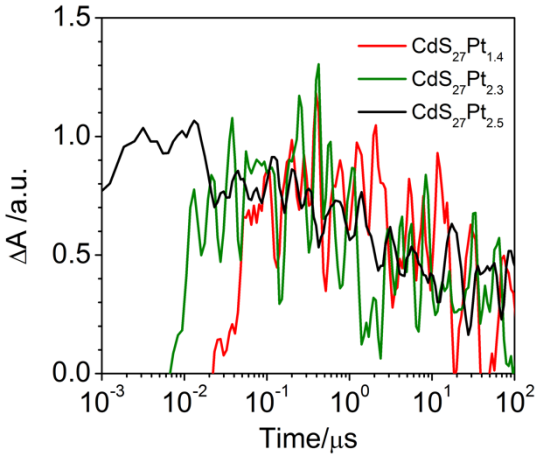

Figure A.3.6. Normalized charge separated state recombination kinetics monitored at 472 nm (derivative feature in Figure A.3.5) for phosphonates capped $CdSPt_{1.4nm}$, $CdSPt_{2.3nm}$ $CdSPt_{2.5nm}$ in toluene.

Operando transient absorption spectra and kinetics of CdS-Pt NRs

The Operando transient absorption measurements are conducted under CW LED illumination. Other condition is same as pump-probe measurements, described in main text.

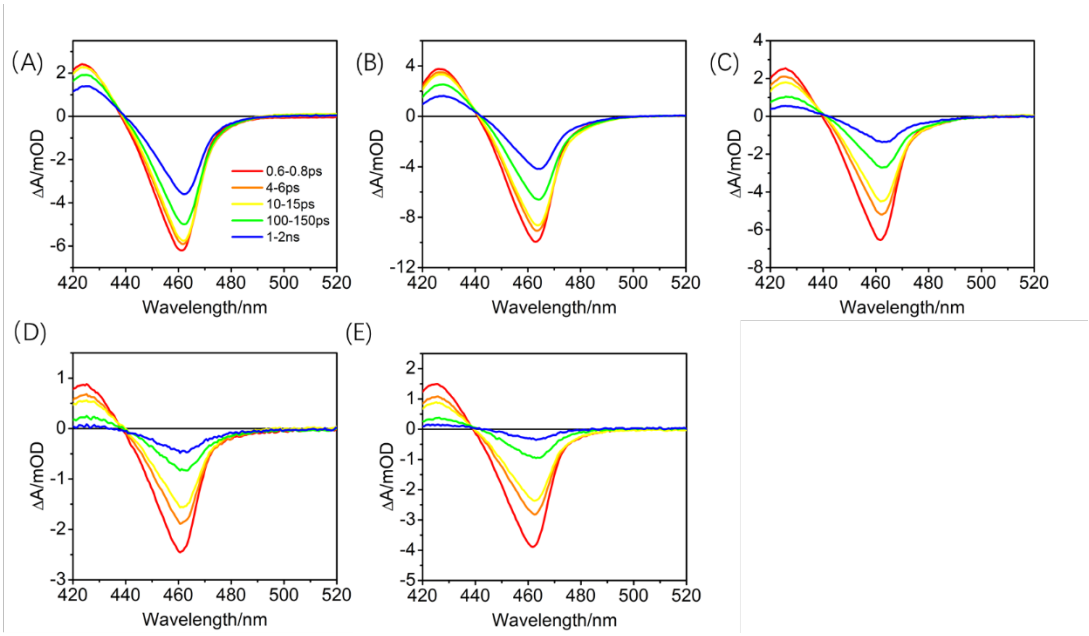

Figure A.3.7. Operando transient absorption spectra of CdS-Pt NRs at selected time delays. (A)$CdSPt_{0.7nm}$, (B) $CdSPt_{1.4nm}$, (C)$CdSPt_{2.3nm}$, (D)$CdSPt_{2.5nm}$, (E)$CdSPt_{3.0nm}$.

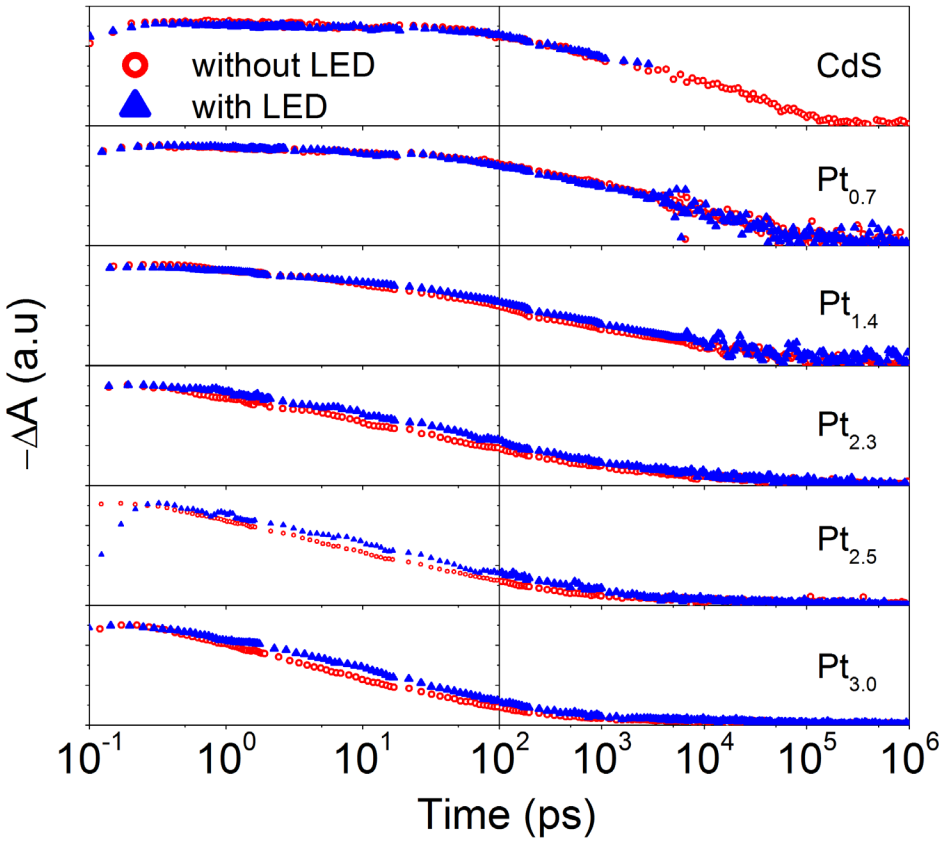

Figure A.3.8. The comparison between electron transfer kinetics with LED illumination and without LED illumination.

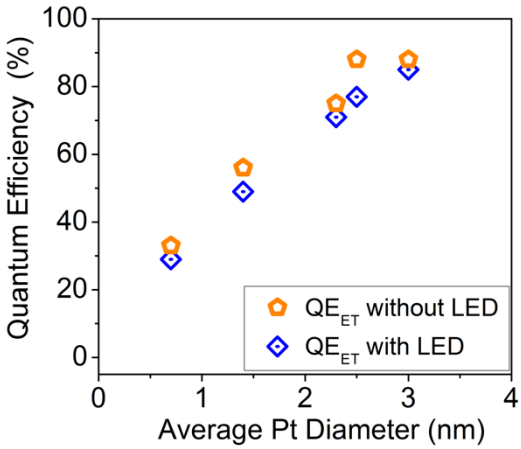

Figure A.3.9. Electron transfer quantum efficiency measured under LED illumination.

Appendix 4

Fitting model of size dependent ET kinetics

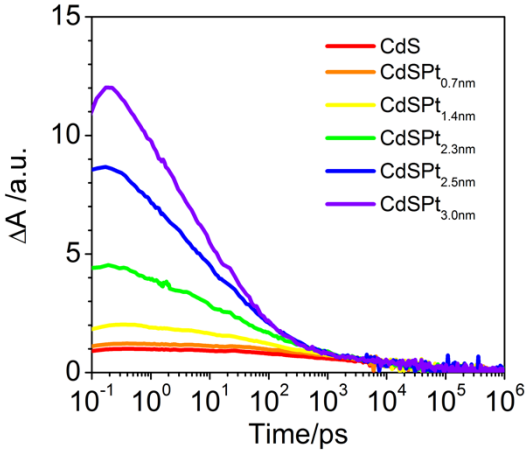

Figure A.3.10. Normalized kinetics at 10^4-10^6 ps of CdS and CdS-Pt.

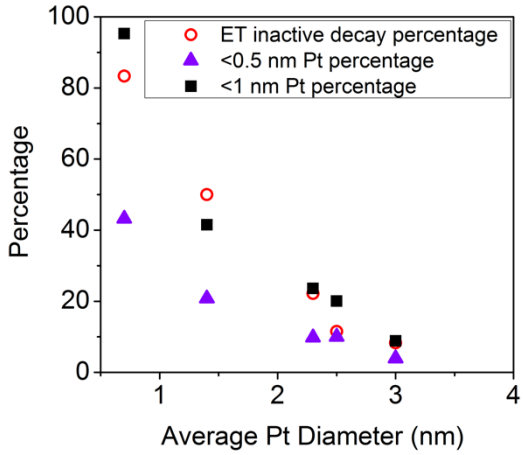

Figure A.3.11. Comparison of percentage of ET-inactive decay component in CdS-Pt exciton bleach recovery kinetics (red circles) and percentage of NRs with Pt tip size of <0.5nm (purple triangles) and <1 nm (black square). The latter includes NRs without tip and are determined from the TEM images (Table A.3.1 and A.3.2).

As discussed in the main text, the exciton decay CdS exciton decay in the absence of the Pt particle can be well described a stretched exponential decay. It can also be described by multiple exponential functions:

$S_{CdS}(t)$=($\sum_i A_i e^{-k_{rec,i}t}$). (A.3.1)

A_i and $k_{rec,i}$ represent the amplitudes and lifetimes, respectively, of the i_{th} component of the multiexponential CdS exciton decay.

TEM images of nanorods show a broad Pt particle size distribution in the ensemble (**Figure** A.3.1). Let $p(j)$ represent occurrence possibility of Pt size between *j* nm and *j*+0.5 nm and $k_{ET,j}$ represents the average electron transfer rate for this size range. The total CB electron decay kinetics can be written as:

$$S_{CdS-Pt}(t) = \sum_i A_i[\sum_j p(j)e^{-(k_{rec,i}+k_{ET,j})t}]$$

$$= S_{CdS}(t) * \sum_j p(j)e^{-(k_{ET,j})t} \quad \text{(A.3.2)}$$

Eq. (A.3.6) is used to fit the transient kinetics. In the fit, $k_{ET,j}$ is set to 0 for j<1 nm or nanorods without Pt particles. The values of $k_{ET,j}$ is set to increase with particle size, i.e. $k_{ET,j-1} <= k_{ET,j} <= k_{ET,j+1}$. The best fit is obtained by minimizing the value of $\chi^2 = 1/\sigma^2 * (\Sigma_t[S_{CdS-Pt}'(t) - S_{CdS-Pt}(t)]^2)$, summing over all time points from 0.5 ps to 1 μs. $S'_{CdS-Pt}(t)$ and $S_{CdS-Pt}(t)$ are the amplitudes of the measured transient absorption signal and its fit by Eq.(A.3.2), respectively. σ is the average standard deviation of $S'_{CdS-Pt}(t)$, estimated to be about 3%. The error of $k_{ET,j}$ is estimated by $\sigma^2_{k_{ET,j}} = \frac{2}{\frac{\partial^2 \chi^2}{\partial kET,j^2}}$.[62] In the fit, the initial guess of $p(j)$ is set at the experimentally

determined values shown in Figure A.3.1 and is allowed to vary slightly to obtain better fit kinetics. The fitting parameters are shown in Table A.3.4 and plotted in Figure 3.3D.

Table A.3.4. $P\ (j)$, the occurrence possibility of different size ranges and electron transfer lifetimes $k_{ET,j}$ obtained from fitting the kinetics.

j	d/nm	$P\ (j)$					$1/k_{ET}$(d) /ps
		$CdSPt_{0.7nm}$	$CdSPt_{1.4nm}$	$CdSPt_{2.3nm}$	$CdSPt_{2.5nm}$	$CdSPt_{3.0nm}$	
1[a]	0-0.5	0.43	0.21	0.10	0.05	0.04	
2	0.5-1	0.40	0.21	0.14	0.10	0.05	
3	1-1.5	0.06	0.22	0.16	0.05	0.03	766±100
4	1.5-2	0.06	0.10	0.06	0.06	0.03	86±18
5	2-2.5	0.05	0.11	0.09	0.16	0.11	86±10
6	2.5-3	0.00	0.06	0.15	0.24	0.25	32±3
7	3-3.5	0.00	0.06	0.21	0.21	0.29	4.6±0.3
8	3.5-4	0.00	0.04	0.07	0.10	0.15	1.4±0.1
9	4-4.5	0.00	0.00	0.02	0.03	0.05	0.7±0.1

[a]This includes nanorods without Pt tips (d=0).

Chapter 4. Length-dependence of photo-driven H_2 production in 1D CdS-Pt heterostructures

4.1. Introduction

A Colloidal quantum confined semiconductor-metal nano-heterostructures are a promising class of photocatalysts for solar energy conversion.[1-9] In these photocatalysts, the semiconductor domain serves as the light absorber and the metal as the catalyst. Such photocatalysts combine the superior light absorption and charge transport properties of the semiconductor with the superior catalytic activity and selectivity of the metal.[4, 10-11] Furthermore, both domains can be independently tuned to enhance the photocatalytic performance of the heterostructure.[5, 12-19]Among various semiconductor/metal heterostructures, metal-tipped colloidal semiconductor nanorods,[20-21] have attracted extensive interest because they have been reported to have high quantum efficiencies of light driven H_2 generation[13, 22-23] and their charge separation and recombination processes can be examined to advance mechanistic understanding and rational design. [3, 13, 22, 24-26] It has been reported previously, the light-driven H_2 generation performance of metal-tipped nanorods depends on the pH of the solution,[1, 13, 23] the nature of the sacrificial electron donors,[3, 27] the size of the metal domain[15, 22, 28] and the length of the nanorods.[12] These studies have reported interesting dependences of the performances on the semiconductor and metal domains. For example, for CdSe@CdS dot-in-rods tipped with Pt particles, their H_2 generation performances increase with the CdS rod length and decrease with the CdSe core diameter.[12] The overall light driven H_2 generation process involves multiple elementary charge separation and recombination steps in the semiconductor and across the semiconductor/metal interface as well as proton-coupled electron transfer reactions at the catalytic center. The change of the semiconductor or metal domains can often have effects on the multiple competing processes in the overall reaction. As a

result of these complexities, the mechanisms for the morphological dependence of the observed H_2 generation efficiencies are not fully understood, hindering the rational design of these photocatalysts.

In this chapter we use Pt tipped CdS nanorod (CdS-Pt NR) heterostructures as a model system to study the mechanism by which the CdS rod length affects their light-driven H_2 production. We observe that the quantum efficiency (QE) of light driven H_2 generation (QE_{H_2}) initially increases with rod length from 4.6±0.9 nm to 27.8.±4.2 nm, but reaches a plateau value of ~ 30% from rod length of 27.8.±4.2 to 88.9±15.8 nm. Because the CdS rod length can affect the rates of the initial electron transfer (ET) from the CdS to the Pt and the lifetime of the charge separated state (with electron in the Pt domain and hole in the CdS domain), the length dependences of these rates were directly measured. We propose a simplified kinetics model that considers key processes from the initial photon absorption to final catalytic reaction and assumes that the overall light driven H_2 generation QE is the product of the QEs of these elementary steps. Using this model, we examine how the CdS rod length affects the quantum efficiencies these elementary steps and the overall H_2 generation performance.

4.2 Results

4.2.1 Sample Preparation

CdS quantum dots (QDs) and four NR samples of different rod lengths are prepared according to reported literature procedures with slight modifications and the Pt tips are deposited by thermal reduction as described in chapter 2.[21] The as-synthesized CdS and CdS-Pt samples have phosphoric acid as native capping ligands and are soluble in organic solvents. To transfer these samples in aqueous solution, the surface ligands were exchanged to 11-mercaptoundecanoic acid

(11-MUA), as described in chapter 2. The CdS and CdS-Pt samples are designated as CdS_{xnm} and CdS_{xnm}-Pt, respectively, with the subscript *x* representing nanorod length or x=QD to indicate CdS QD and QD-Pt samples. The first exciton absorption peaks of CdS QDs and NRs, determined by the radial confinement,[29] are around 450-470 nm, as shown in Figure 4.1A. The absorption spectra of CdS-Pt can be well fit to the sum of CdS absorption bands and a broad Pt d-sp interband absorption feature[30], as shown in Figure 4.1A. Transmission electron microscope (TEM) images of CdS and CdS-Pt are shown in Figure A.4.1 and Figure 4.1B-F, respectively. The detailed statistics of CdS diameter, rod lengths, Pt diameters are listed in Table A.4.1. The diameter of the QD is 4.6±0.9 nm. The CdS and CdS-Pt NR samples have four different rod lengths of 13.8±2.3 nm, 27.8.±4.2 nm, 66.6±6.6 nm, 88.9±15.8 nm, similar CdS diameters in range of 4.1±0.4 to 4.7±0.8 nm and similar Pt tip diameters in the range of 3.3±0.7 nm to 4.0±1.0 nm. Thus, these samples can be considered as nanorods of the same CdS diameters and Pt tip sizes, but different CdS rod length (Figure 4.1G).

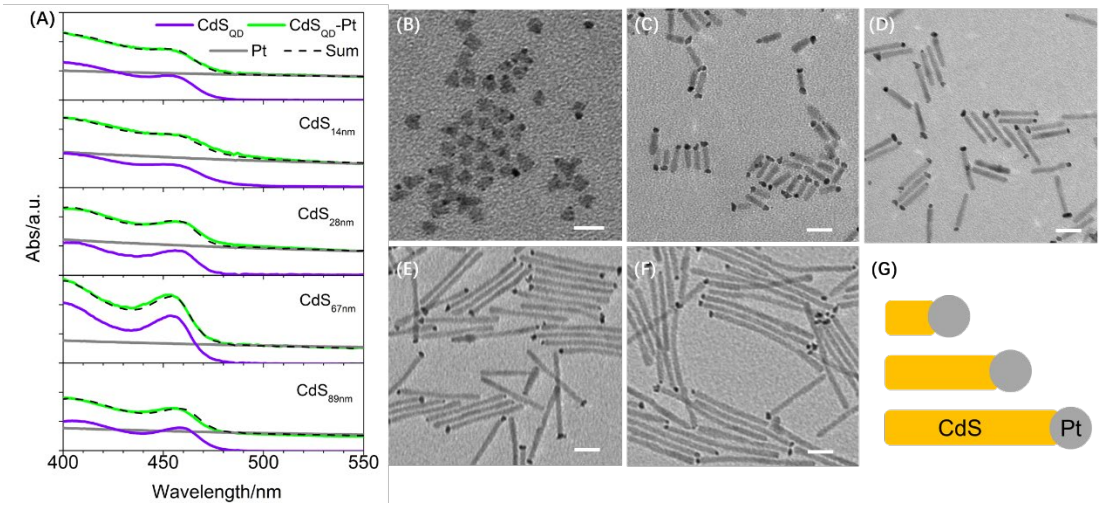

Figure 4.1. Absorption spectra and TEM images of CdS-Pt heterostructures. (A) UV-vis absorption spectra of CdS-Pt NRs in aqueous phase (green lines) and their fits (black dashed lines) by the linear combination of the spectra of free Pt particles (grey solid lines) and CdS NRs or QDs

(violet lines). This indicates that the deposition of Pt has negligible impacts on the CdS exciton bands. (B)-(F) TEM images of CdS_{QD}-Pt, $CdS_{14nm}Pt$, $CdS_{28nm}Pt$, $CdS_{67nm}Pt$, $CdS_{89nm}Pt$, respectively. Scale bars are 10 nm in (B) and 20 nm in other panels. (G) Schematic representation of these samples as nanorods of the same CdS diameters and Pt tip sizes, but different CdS rod lengths.

4.2.2 H_2 production

The photo-catalytical H_2 production measurements using 11-MUA capped CdS-Pt nanocrystals were carried out under continuous 405 nm LED light illumination (power density of ~100 mW/cm^2) in aqueous solution at pH=12 with L-Cysteine (3 mg/mL) as hole scavenger. The absorbances of all samples at 405 nm were adjusted to 0.3 to 0.4. The generated H_2 amount was quantified by gas chromatography. Further details of the measurement are provided in chapter 2. The quantum efficiencies (QE) of H_2 production are calculated by $QE_{H_2} = \frac{2n_{H2}}{n_{photon}} * 100\%$, with n_{H2} and n_{photon} representing the number of produced H_2 and the absorbed photons by the CdS-Pt NRs, respectively, as reported in our previous paper.[31] The measured QE_{H_2} is plotted in Figure 4.2 as a function of rod length. The rod length of the QD sample is taken as its diameter. QY_{H_2} increases from 0.2±0.0% to 27.8±0.4% when rod length increases from 4.6±0.9 nm (QD) to 28±3nm, and then remains constant, within the range of 30±10%, for longer rod lengths (67±7 and 89±15 nm). To understand this length-dependent H_2 production, transient absorption (TA)

spectroscopy was utilized to measure the how the rod-length affects ET and charge recombination (CR) in CdS-Pt heterostructures.

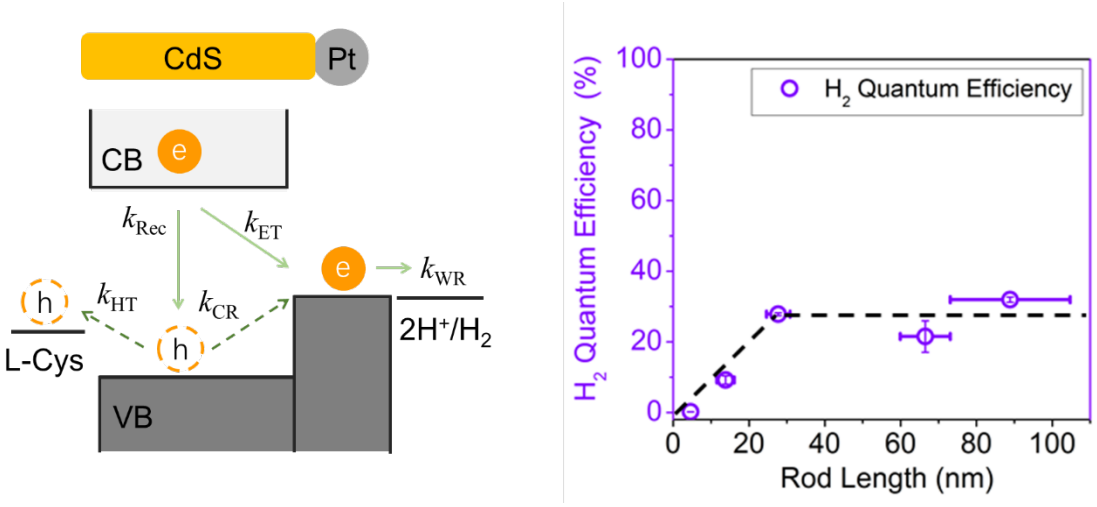

Figure 4.2. Photocatalytic H_2 performance of CdS-Pt NRs. (Left) A scheme of photocatalytic process in CdS-Pt. (right) Measured quantum efficiencies of H_2 production (purple circles) as a function of rod length in CdS-Pt under pH12, 3 mg/mL L-cysteine, 405 nm LED (100mW/cm^2.) Dashed black line is shown to indicate the trend.

4.2.3 Length dependent electron transfer kinetics

ET from CdS to Pt tips was firstly studied by the TA spectroscopy. TA studies of CdS and CdS-Pt NRs were conducted under the same pH and hole scavenger conditions as the light-driven H_2 generation measurement described above using 400 nm pulse laser excitation. The details of the TA measurement are provided in chapter 2. The TA spectra of selected CdS and CdS-Pt samples are shown in Figure 4.3A and 4.3B, respectively. These spectra show similar features: (a) a bleach of 1Σ exciton band (XB) centered at the 450-470 nm due to the electron state filling at the conduction band (CB) edge which reduces 1Σ exciton absorption; (b) an photoinduced absorption

at ~420 nm that is attributed to red-shift of a higher energy transitions due to biexciton interaction.[24] The slight time-dependent red-shift of XB peak position in CdS_{89nm} spectra is likely due to its ununiform rod diameter, which leads to exciton localization into the bulb region.[32] As shown in Figure 4.3C, the XB decay in free CdS NRs shows similar kinetics, independent of the rod length, and can be fit to a stretched exponential function with an average lifetime of 45.7±0.9 ns. Because the XB feature reflects the population of photogenerated CB edge electrons in the CdS NR, its decay in bare CdS reflects the recombination of photogenerated electrons with the holes in the NR.[24] The TA spectra of CdS-Pt NRs show similar spectral features as those in CdS NRs (Figure 4.3B). However, their XB decays on a much faster time scale (Figure 4.3D), which can be attributed to ET from the CdS rod to the Pt tip. The ET half lifetime is 0.7±0.1 ps in CdS_{QD}-Pt and increases to 1.8±0.3 ps, 23.4±3.6 ps, 52.9±7.9 ps, 170.2±29.5 ps for $CdS_{14nm}Pt$, $CdS_{28nm}Pt$, $CdS_{67nm}Pt$ and $CdS_{89nm}Pt$ rods, respectively, increasing with the rod length.

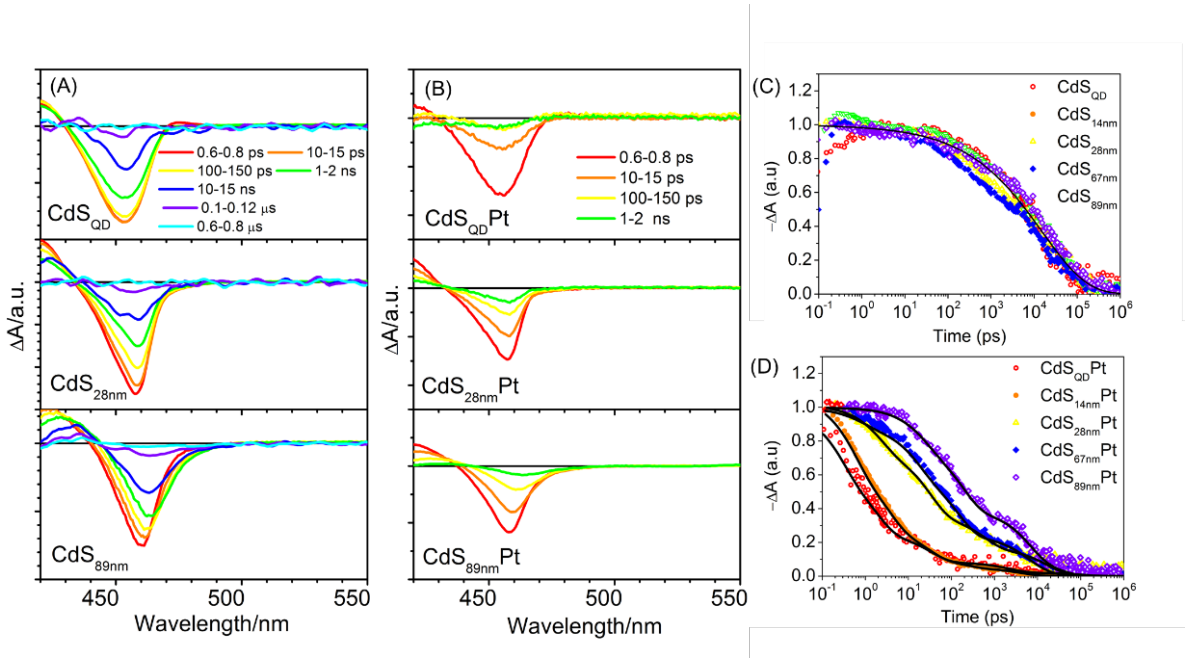

Figure 4.3. Transient absorption spectra of selected MUA capped CdS and CdS-Pt samples in aqueous solution of pH 12. (A) Average TA spectra of CdS_{QD}, CdS_{28nm} and CdS_{89nm} at indicated

time delay windows are shown. (B) Average TA spectra of $CdS_{QD}Pt$, $CdS_{28nm}Pt$ and $CdS_{89nm}Pt$ at indicated time delay windows. (C) XB bleach recovery in CdS NRs of different rod length (symbols) and their fit to a stretched exponential function (black line) with an average lifetime of 45.7±0.9 ns. (D) Exciton bleach recovery kinetics in CdS-Pt samples of different rod lengths (symbols) and their fit to multiexponential decay functions (black lines). Faster XB in CdS-Pt is attributed to electron transfer from the CdS NR to Pt.

4.2.4 Length dependent charge recombination kinetics in toluene

To investigate the length dependence of CR of electrons in the Pt tip with the hole in CdS, we carried out TA study of phosphoric acid capped CdS-Pt NRs dissolved in toluene. The TA spectra of CdS-Pt from 10 ns to 200 μs are shown in Figure 4.4A. After the completion of ET from the CdS to Pt on <1 ns time scale, a second derivative feature of the exciton band is observed beginning at 1-10 ns. This derivative feature has been attributed to the trapped hole in CdS, which shifts the CdS exciton absorption band.[24] Decay of this derivative feature has been attributed to recombination of the electron in Pt with the hole in CdS.[24] Comparison of the recombination kinetics of CdS-Pt of different rod length (Figure 4.4B) shows that the CR lifetime increases with the rod length. With the rod length increases from 4.6±0.9 nm to 14±2 and 28±3 nm, the amplitude-weighted average lifetime of charge separated state increases from 4.7±0.4 μs to 25.7±3.3 μs and 149±34 μs, after which the average lifetime increases negligibly at longer rod lengths. This length-dependent trend is consistent with the observed QY_{H_2} in Figure 4.2, implying CR may be the dominant reason for the size-dependent QY_{H_2}. For 11-MUA capped CdS-Pt in aqueous solution under the light-driven H_2 generation conditions, ET from the CdS to Pt does not lead to the charge separated state signal discussed above, as shown in Figure A.4.5. This is likely caused by fast hole

transfer to the surface 11-MUA ligand, which reduces the Stark effect signal of the CdS exciton band.

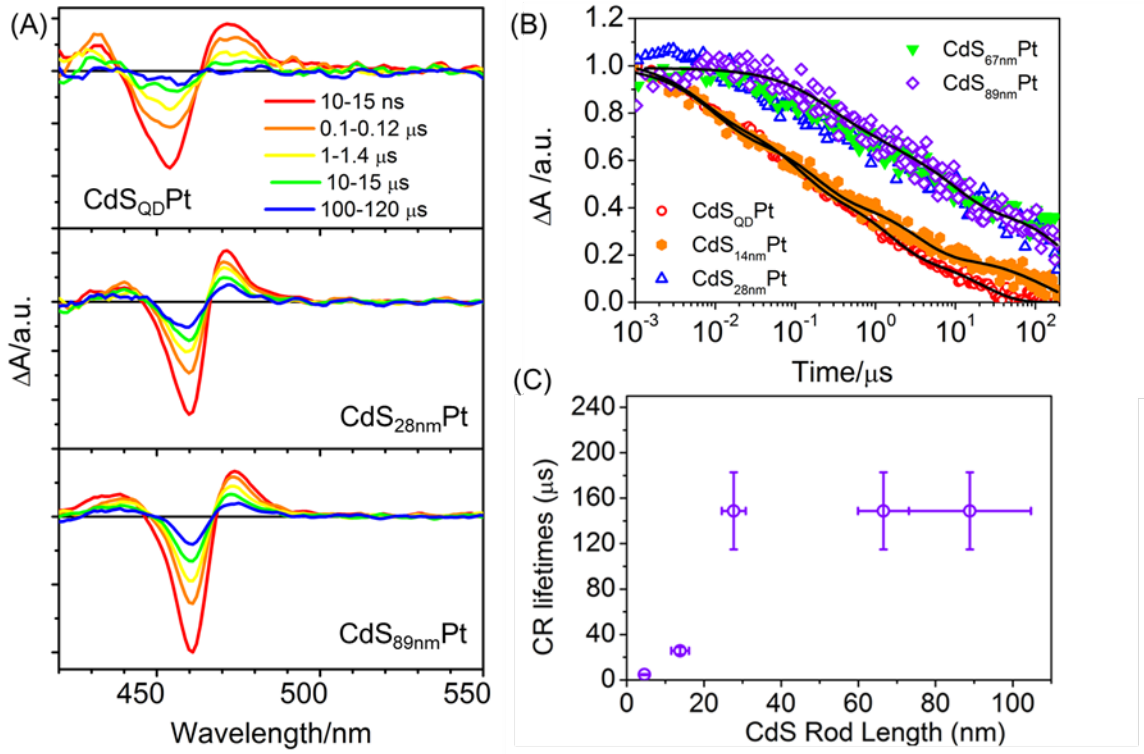

Figure 4.4. Transient absorption spectra of selected phosphoric acid capped CdS-Pt samples in toluene. (A) TA spectra of $CdS_{QD}Pt$ (upper) $CdS_{28nm}Pt$ (middle) and $CdS_{89nm}Pt$ (lower) at selected time delays. These spectra show a clear derivative feature of the exciton band, indicating the appearance of charge separated state with an electron in the Pt and hole in CdS. (B) Comparison of the normalized decay kinetics of the charge separated state at ~470 nm, showing the length dependence of the charge recombination time. (C) Amplitude-weighted average charge recombination time of as a function of the CdS rod length.

4.3. Discussion

The overall light-driven H_2 generation process in CdS-Pt NRs involves multiple forward steps: hole transfer (HT) from the CdS to surface ligands (L), ET from the CdS to Pt, hole from the surface ligand to L-cysteine in solution or hole scavenging (HS), and water reduction (WR) at Pt. Each of these steps competes with a backward charge recombination process. Figure 4.5A shows the schematic energy levels of electrons and holes involved in these steps and Figure 4.5B shows a simplified kinetic model that considers key intermediates and their competing forward and backward processes.[33] As shown in Figure 4.5B, the absorption of a photon generates an exciton in L-CdS-Pt NRs (L=11-MUA), which undergoes fast trapping of the VB hole on a sub-picosecond time scale generates L-CdS*-Pt.[24, 34] In L-CdS*-Pt, the transfer of the trap hole (k_{HT}) to the MUA ligand to form L^+-CdS^--Pt competes with the electron-hole recombination (k_{CR1}) process within CdS* to determine the hole transfer QE (QE_{HT}). QE_{HT} is estimated to be nearly 100% because $k_{HT,}$ ~$(100s\ ps)^{-1}$, is much larger than k_{CR1} (~$10s\ ns)^{-1}$.[1, 3] k_{HT} and k_{CR1} (Figure 4.3C) are length independent, giving rise to a length independent QE_{HT}. In L^+-CdS^--Pt, ET to the Pt tip (k_{ET}) forms a charge separated state (L^+-CdS-Pt^-), which competes with rod-length independent CR (k_{CR2}) (Figure 4.3C). Because k_{ET} is dependent on the rod length (Figure 4.3D), the ET QE (QE_{ET}) is rod-length dependent and can be determined from the transient kinetics. In L^+-CdS-Pt^-, hole transfer from the oxidized surface ligand to the solution hole scavengers (with a rate constant of k_{HS}) forms a long-lived L-CdS-Pt^- species that can proceed on to the slow water reduction steps; and the HT step competes with the rod length dependent CR (k_{CR3}) to give rises to rod length dependent hole scavenging QE (QE_{HS}). Finally, water reduction QE (QE_{WR}) should not vary with the rod length as this step involves only the Pt particle.

The overall quantum efficiency (QE) of the light driven water reduction process can be considered as the product of these four elementary steps according to equation (Eq.) (4.1).

$$QE_{H2} = QE_{HT} * QE_{ET}(L) * QE_{HS}(L) * QE_{WR} = C * QE_{ET}(L) * QE_{HS}(L) \quad (4.1)$$

Because QE_{HT} and QE_{WR} are rod-length independent, in Eq. (4.1) we have grouped the product of the rod length independent QEs into a constant C $(= QE_{HT} * QE_{WR})$.

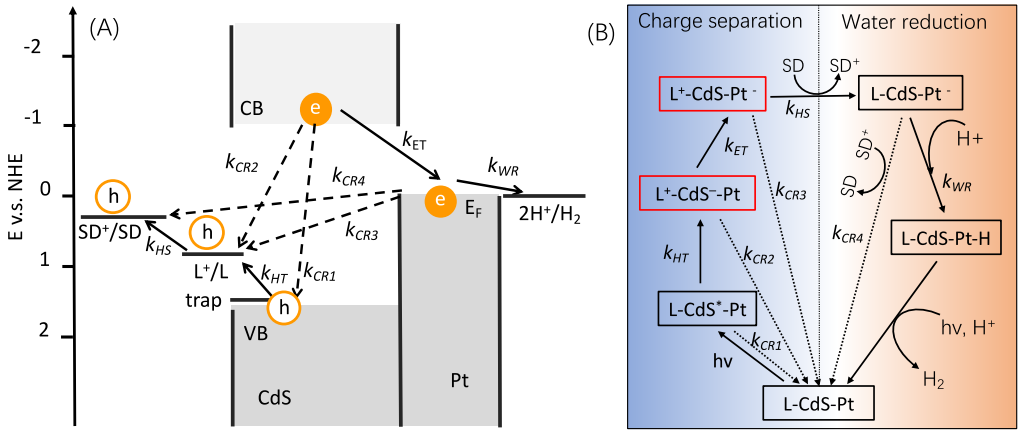

Figure 4.5. Mechanism of rod length dependent light driven H_2 generation quantum efficiency in L-CdS-Pt nanorods. (A) Key energy levels and elementary processes and (B) simplified kinetic model showing key intermediate states and their competing forward and backward processes involved in the overall light driven H_2 generation. L indicates the MUA capping ligands on the CdS surface. Forward processes (solid arrows): hole transfer from the trapped exciton state to surface ligand L (with a rate constant k_{HT}), ET from the CdS to Pt (k_{ET}), hole transfer from the oxidized surface ligand L^+ to hole sacrificial donor SD (k_{HS}), water reduction on reduced Pt particle (k_{WR}). Each process competes with a CR process (k_{CRi}, i=1-4, dashed arrows), which determines the quantum efficiency of each elementary step. The overall quantum efficiency of light drive H_2 generation is the product of the quantum efficiencies of the elementary steps. (Figure 4.5 A and B are adapted from reference 33).

The QE for ET from the CdS to Pt (QE_{ET}) can be determined from the XB kinetics using Eq. (4.2).[35]

$$QE_{ET} = 1 + \int_0^{\infty} dt \frac{dS_{CdS}(t)}{dt} \frac{S_{CdS-Pt}(t)}{S_{CdS}(t)} \quad . \quad (4.2)$$

In Eq. (4.2), $S_{CdS}(t)$ and $S_{CdS-Pt}(t)$ represent the normalized time dependent probability distribution of the CdS CB electron in CdS and CdS-Pt NRs, respectively, which can be obtained from their 1Σ exciton bleach recovery kinetics. The calculated QE_{ET} values for CdS-Pt of different lengths are shown in Figure 4.6A (orange triangle). From the measured QE_{ET} and QE_{H_2}, the QE of the remaining steps $QE_{HT} * QE_{HS}(L) * QE_{WR} = C * QE_{HS}(L)$ can be determined by the ratio between QE_{H_2} and QE_{ET}, which is plotted in Figure 4.6B (orange circles). QE_{ET} decreases monotonically and relatively slowly from 92% to 70% when the rod length increases from 4.6±0.9 nm to 89±15 nm, as shown in Figure 4.6A. Interestingly, calculated $C * QE_{HS}$, increases more rapidly with the rod length from 0.2% for L= 4.6±0.9 nm in $CdS_{QD}Pt$ to 35% for L= 28±3nm, and then stays at 35±10% for longer length. Thus, the observed length dependent QY_{H_2} in CdS-Pt NRs mainly reflects the trend of QE_{HS}, which is determined by the length dependent charge recombination rates in L^+-CdS-Pt^-.

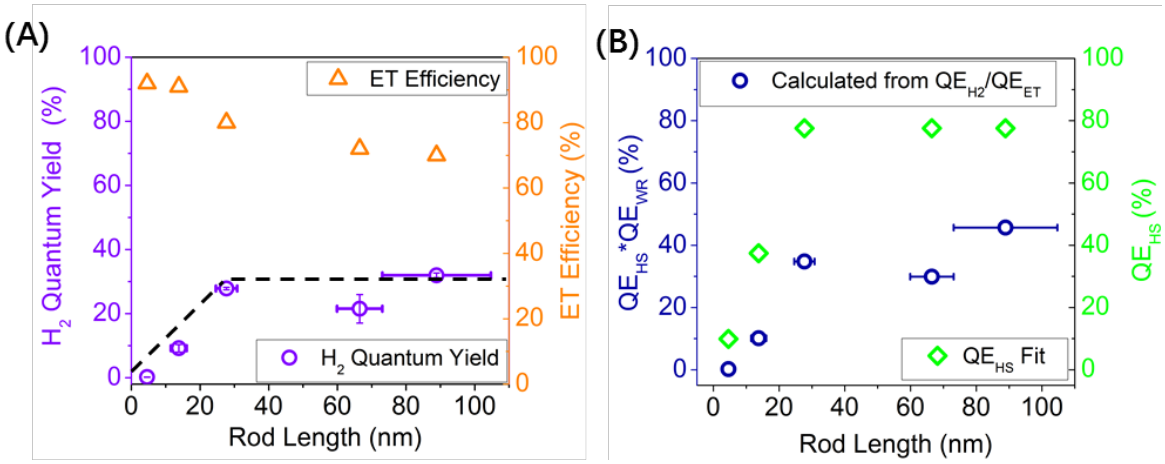

Figure 4.6. Quantum efficiencies of elementary steps involved in the overall light driven H_2 generation in L-CdS-Pt. (A) Measured quantum efficiencies of H_2 production (purple circles, QE_{H_2} from Figure 4.2) and electron transfer (orange triangles, QE_{ET}) as a function of the CdS rod length. Dashed black line is drawn to indicate the trend. (B) Comparison of $C * QE_{HS}(L)$ calculated from measured QE_{H2} and QE_{HT} according to Eq. (4.1) (blue circles) and from measured charge recombination rates according to Eq.4.3 (green diamond).

QE_{HS} is determined by the competition between hole removal to L-cysteine and charge recombination in L^+-CdS-Pt^- (k_{CR3}) according to Eq. (4.3).

$$QE_{HS}(L) = \frac{k_{HS}}{k_{HS}+k_{CR3}(L)} = \frac{1}{1+k_{CR3}(L)/k_{HS}} \qquad (4.3)$$

In Eq. (3), the hole removal process is characterized by a pseudo-first-order rate constant of k_{HS} and charge recombination in in L^+-CdS-Pt^- is a first order process with a rate constant of k_{CR3}. Assuming that $k_{HS} = 1/(43\,\mu s)$ and taking the measured charge recombination rate in Figure 4.4D as k_{CR3}, the calculated $QE_{HS}(L)$ is plotted in Figure 4.6B. The trend of the calculated

$QE_{HS}(L)$ agree well with the trend of $QE_{HS}(L)$ estimated from the measured QE_{H_2} and QE_{ET} according to Eq. (4.1).

The above k_{HS} value is estimated from a previous study of light driven MV^{2+} reduction using mercaptopropionic acid MPA capped CdS QDs.[36] Under condition of pH 7 and 3-mercaptopropionic acid (MPA) as hole scavenger, the quantum yield of MV^{2+} reduction was determined to be 12.61 ± 1.55% and the radical time was ~5.1 μs (or $k_{HS} + k_{CR3} = 0.19\ \mu s^{-1}$). Because of the unity QEs for both electron and hole transfer steps under those conditions, the radical generation QEs is determined solely by QE_{HS}. Using Eq. (4.3), k_{HS} and k_{CR3} can be determined to be $1/(43\ \mu s)$ and $1/(5.8\mu s)$, respectively. Because the hole scavenging rate should not depend on the presence of Pt particle, we assume that this k_{HS} value can be used as an estimate of the hole scavenging rate in the CdS-Pt samples under light driven H_2 generation conditions. Because k_{HS} depends on both the identity and concentration of the hole acceptors and hole scavengers, a more accurate value should be determined from measurements under the same conditions. Furthermore, charge recombination in L^+-CdS-Pt^- in water is also likely different from that of CdS^+-Pt^- in an organic solvent (Figure 4.4D) because in the former, the hole is localized on the thiol group of the surface ligand and in the later at a surface trap site (likely the surface S atom). These approximations will affect the quantitative values of of $QE_{HS}(L)$, but they should not alter the qualitative trend of its dependence on the CdS rod length.

4.4. Conclusion

In this chapter, we use CdS-Pt NR heterostructures as a model system to study the change separation distance-dependence on ET, CR and their impacts on H_2 production. We found with increasing rod length from 4.6±0.9 nm in quantum dot (QD) to 89±15 nm in 1D nanorod (NR), though ET half lifetime increases from 0.7±0.1 to 170.2±29.5 ps, ET efficiency decreases only

from 92% to 70%. The amplitude-weighted average lifetime of CR increases from 4.7±0.4 μs in QD to 149±34 μs in 28±3 nm nanorods and stay the same up to 89±15 nm. The combination of length-dependent ET and CR results in enhanced H_2 production yield from 0.2±0.0 % to 27.8±0.4% when dimension of CdS changes from QD to 28±3 nm NR, and stay around ~20 to 30% for longer rods. Our findings provide guidance on how to rationally design these materials for efficient light driven charge separation and H_2 generation.

References

1. Li, Q.; Zhao, F.; Qu, C.; Shang, Q.; Xu, Z.; Yu, L.; McBride, J. R.; Lian, T., Two-Dimensional Morphology Enhances Light-Driven H2 Generation Efficiency in Cds Nanoplatelet-Pt Heterostructures. *J. Am. Chem. Soc.* **2018**, *140*, 11726-11734.
2. Zhu, H.; Song, N.; Lv, H.; Hill, C. L.; Lian, T., Near Unity Quantum Yield of Light-Driven Redox Mediator Reduction and Efficient H2 Generation Using Colloidal Nanorod Heterostructures. *J Am Chem Soc* **2012**, *134*, 11701-8.
3. Wu, K.; Chen, Z.; Lv, H.; Zhu, H.; Hill, C. L.; Lian, T., Hole Removal Rate Limits Photodriven H2 Generation Efficiency in Cds-Pt and Cdse/Cds-Pt Semiconductor Nanorod-Metal Tip Heterostructures. *J. Am. Chem. Soc.* **2014**, *136*, 7708-7716.
4. Wu, K.; Lian, T., Quantum Confined Colloidal Nanorod Heterostructures for Solar-to-Fuel Conversion. *Chem. Soc. Rev.* **2016**, *45*, 3781-810.
5. Berr, M.; Vaneski, A.; Susha, A. S.; Rodríguez-Fernández, J.; Döblinger, M.; Jäckel, F.; Rogach, A. L.; Feldmann, J., Colloidal Cds Nanorods Decorated with Subnanometer Sized Pt Clusters for Photocatalytic Hydrogen Generation. *Appl. Phys. Lett.* **2010**, *97*, 093108.
6. Carey, G. H.; Abdelhady, A. L.; Ning, Z.; Thon, S. M.; Bakr, O. M.; Sargent, E. H., Colloidal Quantum Dot Solar Cells. *Chem Rev* **2015**, *115*, 12732-63.
7. Panfil, Y. E.; Oded, M.; Banin, U., Colloidal Quantum Nanostructures: Emerging Materials for Display Applications. *Angew Chem Int Ed Engl* **2018**, *57*, 4274-4295.
8. Talapin, D. V.; Lee, J.-S.; Kovalenko, M. V.; Shevchenko, E. V., Prospects of Colloidal Nanocrystals for Electronic and Optoelectronic Applications. *Chemical Reviews* **2010**, *110*, 389-458.
9. Wilker, M. B.; Schnitzenbaumer, K. J.; Dukovic, G., Recent Progress in Photocatalysis Mediated by Colloidal Ii-Vi Nanocrystals. *Isr J Chem* **2012**, *52*, 1002-1015.
10. Li, X. B.; Xin, Z. K.; Xia, S. G.; Gao, X. Y.; Tung, C. H.; Wu, L. Z., Semiconductor Nanocrystals for Small Molecule Activation Via Artificial Photosynthesis. *Chem Soc Rev* **2020**, *49*, 9028-9056.
11. Burke, R.; Bren, K. L.; Krauss, T. D., Semiconductor Nanocrystal Photocatalysis for the Production of Solar Fuels. *J Chem Phys* **2021**, *154*, 030901.
12. Amirav, L.; Alivisatos, A. P., Photocatalytic Hydrogen Production with Tunable Nanorod Heterostructures. *J. Phys. Chem. Lett.* **2010**, *1*, 1051-1054.

13. Simon, T., et al., Redox Shuttle Mechanism Enhances Photocatalytic H2 Generation on Ni-Decorated Cds Nanorods. *Nat. Mater.* **2014**, *13*, 1013-1018.
14. Simon, T.; Carlson, M. T.; Stolarczyk, J. K.; Feldmann, J., Electron Transfer Rate Vs Recombination Losses in Photocatalytic H2 Generation on Pt-Decorated Cds Nanorods. *ACS Energy Letters* **2016**, *1*, 1137-1142.
15. Schweinberger, F. F., et al., Cluster Size Effects in the Photocatalytic Hydrogen Evolution Reaction. *J. Am. Chem. Soc.* **2013**, *135*, 13262-13265.
16. Chen, O., et al., Compact High-Quality Cdse-Cds Core-Shell Nanocrystals with Narrow Emission Linewidths and Suppressed Blinking. *Nat Mater* **2013**, *12*, 445-51.
17. Weiss, E. A., Designing the Surfaces of Semiconductor Quantum Dots for Colloidal Photocatalysis. *ACS Energy Letters* **2017**, *2*, 1005-1013.
18. Harris, R. D.; Bettis Homan, S.; Kodaimati, M.; He, C.; Nepomnyashchii, A. B.; Swenson, N. K.; Lian, S.; Calzada, R.; Weiss, E. A., Electronic Processes within Quantum Dot-Molecule Complexes. *Chem Rev* **2016**, *116*, 12865-12919.
19. She, C.; Fedin, I.; Dolzhnikov, D. S.; Dahlberg, P. D.; Engel, G. S.; Schaller, R. D.; Talapin, D. V., Red, Yellow, Green, and Blue Amplified Spontaneous Emission and Lasing Using Colloidal Cdse Nanoplatelets. *ACS Nano* **2015**, *9*, 9475-9485.
20. Carbone, L.; Kudera, S.; Giannini, C.; Ciccarella, G.; Cingolani, R.; Cozzoli, P. D.; Manna, L., Selective Reactions on the Tips of Colloidal Semiconductor Nanorods. *J. Mater. Chem.* **2006**, *16*, 3952-3956.
21. Habas, S. E.; Yang, P.; Mokari, T., Selective Growth of Metal and Binary Metal Tips on Cds Nanorods. *J. Am. Chem. Soc.* **2008**, *130*, 3294-3295.
22. Ben-Shahar, Y.; Scotognella, F.; Kriegel, I.; Moretti, L.; Cerullo, G.; Rabani, E.; Banin, U., Optimal Metal Domain Size for Photocatalysis with Hybrid Semiconductor-Metal Nanorods. *Nat. Commun.* **2016**, *7*, 10413.
23. Kalisman, P.; Nakibli, Y.; Amirav, L., Perfect Photon-to-Hydrogen Conversion Efficiency. *Nano Lett.* **2016**, *16*, 1776-1781.
24. Wu, K.; Zhu, H.; Liu, Z.; Rodriguez-Cordoba, W.; Lian, T., Ultrafast Charge Separation and Long-Lived Charge Separated State in Photocatalytic Cds-Pt Nanorod Heterostructures. *J. Am. Chem. Soc.* **2012**, *134*, 10337-10340.
25. Ben-Shahar, Y.; Philbin, J. P.; Scotognella, F.; Ganzer, L.; Cerullo, G.; Rabani, E.; Banin, U., Charge Carrier Dynamics in Photocatalytic Hybrid Semiconductor-Metal Nanorods: Crossover from Auger Recombination to Charge Transfer. *Nano Lett.* **2018**, *18*, 5211-5216.
26. Mongin, D.; Shaviv, E.; Maioli, P.; Crut, A.; Banin, U.; Del Fatti, N.; Vallée, F., Ultrafast Photoinduced Charge Separation in Metal–Semiconductor Nanohybrids. *ACS Nano* **2012**, *6*, 7034-7043.
27. Berr, M. J.; Wagner, P.; Fischbach, S.; Vaneski, A.; Schneider, J.; Susha, A. S.; Rogach, A. L.; Jäckel, F.; Feldmann, J., Hole Scavenger Redox Potentials Determine Quantum Efficiency and Stability of Pt-Decorated Cds Nanorods for Photocatalytic Hydrogen Generation. *Applied Physics Letters* **2012**, *100*.
28. Nakibli, Y.; Mazal, Y.; Dubi, Y.; Wachtler, M.; Amirav, L., Size Matters: Cocatalyst Size Effect on Charge Transfer and Photocatalytic Activity. *Nano Lett.* **2018**, *18*, 357-364.
29. Shabaev, A.; Efros, A. L., 1d Exciton Spectroscopy of Semiconductor Nanorods. *Nano Lett.* **2004**, *4*, 1821-1825.
30. Henglein, A.; Ershov, B. G.; Malow, M., Absorption Spectrum and Some Chemical Reactions of Colloidal Platinum in Aqueous Solution. *J. Phys. Chem.* **1995**, *99*, 14129-14136.

31. Yang, W., et al., Surface-Ligand "Liquid" to "Crystalline" Phase Transition Modulates the Solar H2 Production Quantum Efficiency of Cds Nanorod/Mediator/Hydrogenase Assemblies. *ACS Appl. Mater. Interfaces* **2020**, *12*, 35614-35625.
32. Wu, K.; Rodriguez-Cordoba, W.; Lian, T., Exciton Localization and Dissociation Dynamics in Cds and Cds-Pt Quantum Confined Nanorods: Effect of Nonuniform Rod Diameters. *J. Phys. Chem. B* **2014**, *118*, 14062-9.
33. Liu, Y. Y., Wenxing; Chen, Qiaoli; Cullen, David; Xie, Zhaoxiong; Lian, Tianquan, Pt Particle Size Affects Both the Charge Separation and Water Reduction Efficiencies of Cds-Pt Nanorod Photocatalysts for Light-Driven H2 Generation. *Submitted* **2021**.
34. Cline, R. P.; Utterback, J. K.; Strong, S. E.; Dukovic, G.; Eaves, J. D., On the Nature of Trapped-Hole States in Cds Nanocrystals and the Mechanism of Their Diffusion. *J. Phys. Chem. Lett.* **2018**, *9*, 3532-3537.
35. Utterback, J. K.; Wilker, M. B.; Mulder, D. W.; King, P. W.; Eaves, J. D.; Dukovic, G., Quantum Efficiency of Charge Transfer Competing against Nonexponential Processes: The Case of Electron Transfer from Cds Nanorods to Hydrogenase. *J. Phys. Chem. C* **2018**, *123*, 886-896.
36. Zhao, F.; Li, Q.; Han, K.; Lian, T., Mechanism of Efficient Viologen Radical Generation by Ultrafast Electron Transfer from Cds Quantum Dots. *The Journal of Physical Chemistry C* **2018**, *122*, 17136-17142.

Appendix 1

Characterization of CdS QDs and CdS NRs

Table A.4.1. Statistics of nanorods.

	$CdS_{14nm}Pt$	$CdS_{28nm}Pt$	$CdS_{67nm}Pt$	$CdS_{89nm}Pt$	CdS QD
Diameter/nm	4.3±0.6	4.1±0.4	4.2±0.7	4.7±0.8	4.6±0.9
Length/nm	13.8±2.3	27.8.±4.2	66.6±6.6	88.9±15.8	
Pt diameter/nm	3.6±1.1	3.3±0.7	3.4±0.8	4.0±1.0	1.9±0.6

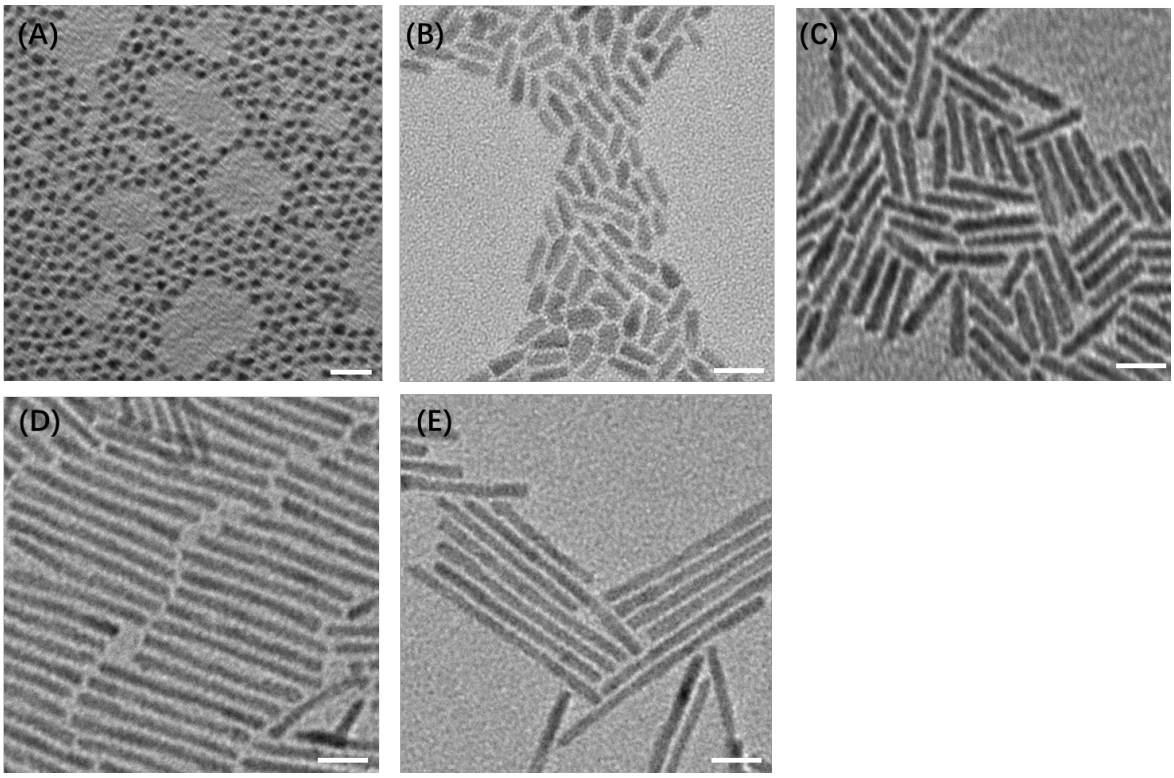

Figure A.4.1. TEM images of CdS. (A-F) are TEM images of CdS_{QD}, CdS_{14nm}, CdS_{28nm}, CdS_{67nm}, CdS_{89nm}, respectively. The white scale bars represent 20 nm.

Appendix 2

Photo-catalytical H_2 production

Table A.4.2. Photocatalytical performance of CdS-Pt.

	$CdS_{QD}Pt$	$CdS_{14nm}Pt$	$CdS_{28nm}Pt$	$CdS_{67nm}Pt$	$CdS_{89nm}Pt$
QY_{H2} (%)	0.2±0.0	9.2±1.2	27.8±0.4	21.5±4.5	32.0±0.7

Appendix 3

Transient absorption spectroscopy results

TA Spectra of $CdS_{14nm}Pt$ and $CdS_{67nm}Pt$

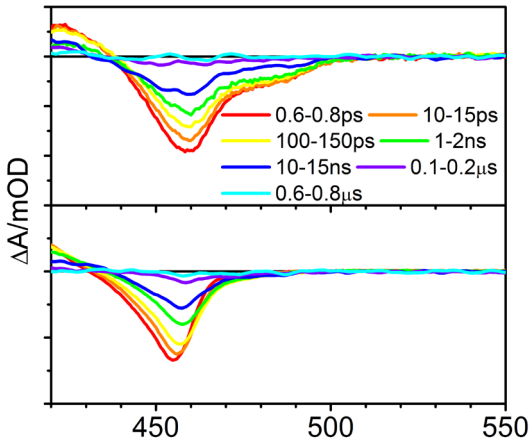

Figure A.4.2. TA spectra of CdS_{14nm} (upper) and CdS_{67nm} (lower) capped with 11-MUA.

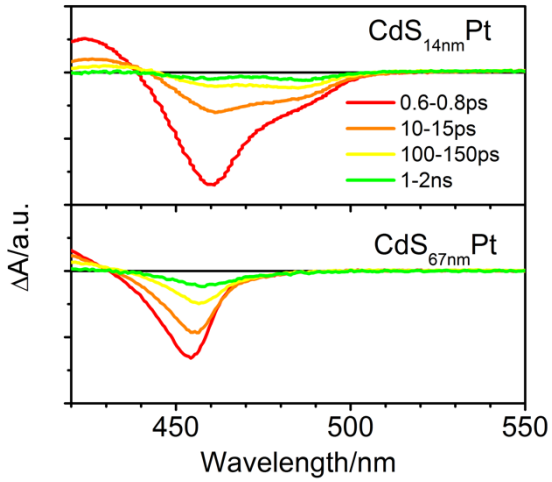

Figure A.4.3. TA spectra of $CdS_{14nm}Pt$ (upper) and $CdS_{67nm}Pt$ (lower) capped with 11-MUA.

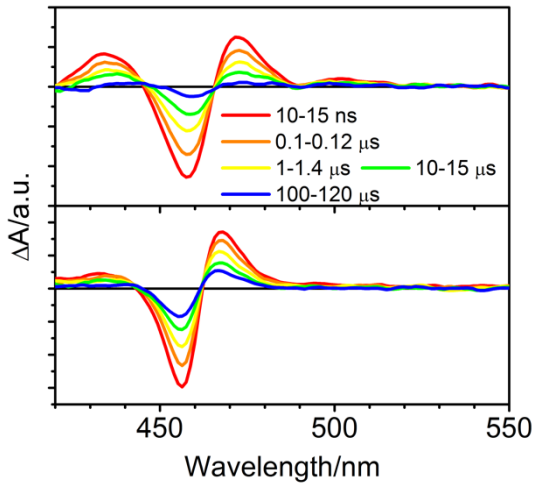

Figure A.4.4. TA spectra of $CdS_{14nm}Pt$ (upper) and $CdS_{67nm}Pt$ (lower) capped with phosphoric acids before ligand exchange.

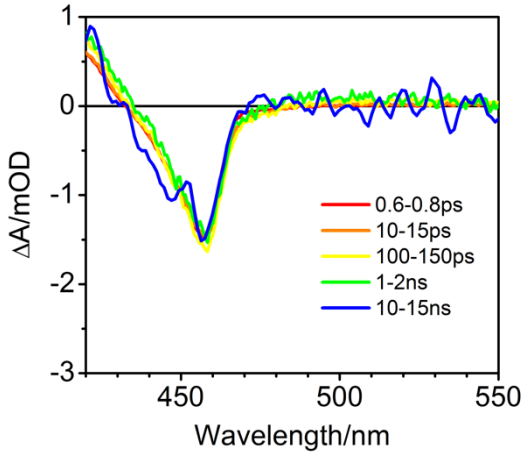

Figure A.4.5. Comparison of spectra of $CdS_{28nm}Pt$ at different time delays. The consistency of spectra at late times and early times indicates no hole signal or charge-separated state signal potentially due to fast hole trapping by L-cysteine.

Fit of Charge transfer kinetics.

The normalized kinetics are fitted with five exponentials, shown as

$$\Delta A = \sum A_i \exp\left(-\frac{t}{\tau_i}\right) \text{ (i=1-5)} \qquad \text{(A.4.1)}$$

A_i is the percentage of the component. τ_i is the lifetime. Below shows the details of the fitting.

Table A.4.3. Fit of charge transfer kinetics.

	$CdS_{QD}Pt$	$CdS_{14nm}Pt$	$CdS_{28nm}Pt$	$CdS_{67nm}Pt$	$CdS_{89nm}Pt$
1	0.3±0.0 ps 39.0±3.3 %	0.5±0.1 ps 39.4±3.2 %	2.2±0.2 ps 27.4±1.3 %	0.8±0.2 ps 10.9±1.2 %	21.3±4.0 ps 21.9±3.1 %
2	1.9±0.2 ps 37.1±3.0 %	3.4±0.7 ps 33.7±3.0 %	31.6±3.0 ps 39.6±1.4 %	15.7±2.2 ps 27.4±2.1 %	171.9±22.4 ps 39.0±2.8 %
3	34.0±5.4 ps 17.6±1.2 %	28.4±11.4 ps 17.4±2.9 %	568.9±80.2 ps 19.7±1.2 %	142.9±13.7 ps 37.7±2.2 %	5169.2±488.5 ps 29.6±1.2 %
4	2259.4± 644.2ps 6.4±0.7 %	216.1±217.7 ps 4.9±3.0 %	14.4±2.1 ns 13.3±0.8 %	5.5±0.5 ns 18.2±0.7 %	91.2±19.5 ns 9.5±0.9 %
5		4.4±1.4 ns 4.6±1.0 %		204.9±34.8 ns 5.8±0.5 %	
Half	0.7±0.1 ps	1.8±0.3 ps	23.4±3.6 ps	52.9±7.9 ps	170.2±29.5 ps

Fit the charge recombination of charge-separated state signal

The normalized kinetics are fitted with four exponentials, shown as

$$\Delta A = \sum A_i \exp\left(-\frac{t}{\tau_i}\right) \text{ (i=1-4)} \qquad \text{(A.4.2)}$$

A_i is the percentage of the component. τ_i is the lifetime. Below shows the details of the fitting.

Table A.4.4. Fit the charge recombination of charge-separated state signal

	$CdS_{QD}Pt$	$CdS_{14nm}Pt$	$CdS_{28nm}Pt$
1	6.6±0.9 ns 23.5±1.5%	9.0±1.5 ns 27.8±2.0 %	0.2±0.1 μs 18.4±15.3%
2	98.3±10.5 ns 28.8±1.3 %	165.8±24.6 ns 27.5±1.7 %	0.9±1.5 μs 12.3±12.6 %
3	1.4±0.1 μs 28.1±1.1 %	3.1±0.4 μs 25.2±1.4 %	8.9±3.0 μs 28.2±5.3 %
4	21.5± 1.8μs 19.5±1.0 %	127.8±15.6 μs 5.3±3.2 %	358.8± 80.7μs 41.1±2.3 %
Ave.	4.7±0.4 μs	25.7±3.3 μs	148.8±33.9 μs

Table A.4.5. Estimation of the Electron Transfer Efficiency

	$CdS_{QD}Pt$	$CdS_{14nm}Pt$	$CdS_{28nm}Pt$	$CdS_{67nm}Pt$	$CdS_{89nm}Pt$
η_{ET} (%)	92.1	91.4	79.9	71.1	70.3

Chapter 5. Auger Recombination and Multiexciton dissociation in CdS-Pt Nanorod Heterostructures

5.1. Introduction

Direct solar-to-fuel conversion, such as H_2 production,[1-4] CO_2 reduction,[5-8] and N_2 fixation[9-10], is a promising approach for generating storable renewable clean energy that can be used on demand. Most solar fuel forming reactions involve multiple proton-coupled electron transfer (PCET) processes, powered by the energetic electrons and/or holes generated by the absorption of multiple photons. For example, photoreduction of water or proton to form H_2 requires the transfer of two electrons and two protons to the catalytic site, often with the two energetic electrons generated by the absorption of two photons. Furthermore, many solar fuels forming reactions involve competition of multiple product pathways that require different number of electrons and protons, and their branching ratio and resulting product selectivity depends on the concentration of electrons and protons.[11-13] For example, recent studies of light driven N_2 fixation in CdS quantum dot (QD)/nitrogenase complexes show that increasing the photon excitation rate can increase the NH_3/ H_2 product ratio.[14-15] Fluence-dependent H_2 production efficiency in CdS-Au heterostructures has also been reported due to the competition between carrier transfer and Auger recombination.[16] It remains unclear how to efficiently couple multiple electron transfer from the light harvesting materials with the multiple PCET reaction of the catalytic center to achieve efficient and selective catalytic conversion.

In the past decades, the mechanism of PCET reactions has been studied using molecular sensitizers coupled with catalysts.[17] In an effort to facilitate the delivery and accumulation of multiple electrons within a molecular sensitizer-catalyst complex, sensitizers with sophisticated chemical structures, such as covalently linked multiple chromophore units, have been used.[18-19]

The recent development of quantum confined colloidal semiconductor nanocrystals provides new opportunities to design simpler, more robust and more cost effective light harvesting materials that can deliver multiple electrons to catalysts to drive solar-fuel generation.[20-22] Unlike molecular chromophores, multiexciton can be generated in these nanocrystals through multiexciton generation processes (in which the absorption of one high energy photon creates two or more lower energy excitons)[23-25] or by the absorption of multiple photons (through intense illumination).[26-28] QDs doped with rare earth metals can undergo quantum cutting, splitting a high energy absorbed photon into two lower energy emitted photons.[29-30] Colloidal nanocrystals can be readily functionalized by attaching metallic nanoparticles,[1, 31-38] molecular catalysts[39-42] and enzymes[9, 43-44] to form artificial photosynthetic systems for various solar-to-fuel transformations. In addition to the ability to control exciton dynamics through the size, shape and composition of nanocrystals, multiple nanocrystal assemblies can be formed through electrostatic interaction and have been shown to funnel excitons and charges to catalysts to enhance photocatalysis.[45-48] The presence of ligands on the QD surface can also be potentially used to judiciously position proton sources to enhance PCET reactions.[49] Although previous studies have shown that multiple electron transfer (ET) from multiple exciton states in QDs can be achieved by adsorbing many acceptors[50-53] (or dimeric molecules[52]) such that each molecule accepts one electron, efficient transfer of multiple electrons to the same catalyst remains challenging.

Transfer of multiple electrons to a catalyst from a nanocrystal multi-exciton state competes with electron-hole Auger recombination within the nanocrystal and interfacial recombination of separated charges across the nanocrystal/catalyst interface,[16, 22, 54-56] as illustrated in Figure 5.1 for the transfer of two electrons from a biexciton state in CdS-Pt nanorods. So far, most mechanistic studies of nanocrystal/catalyst assemblies have focused on charge separation from a single exciton

state and/or charge recombination of one separated electron and hole pair. [26, 37, 50, 53, 57-58] To rationally design QD/catalyst complexes for efficient multiple PCET catalysis, key fundamental challenges in multiple exciton dissociation and charge recombination have to be addressed. It remains unclear how charge separation efficiencies in a multiple exciton state differ from the extensively studied single exciton states.[59-60] A recent report of multiple exciton dissociation in CdSe/CdS-Pt NRs show that the first electron transfer occurs with a time constant of 192 ps, while the second electron transfer is slowed down to 1700 ps, reducing the efficiency of separating multiple charges from multi-exciton states.[55] Can the slowing down of second charge separation process be avoided through nanocrystal design? Furthermore, efficient catalysis also requires long-lived charge separated state. How the recombination of charge separated states with multiple electrons and holes differs from that with a single separated electron and hole pair?

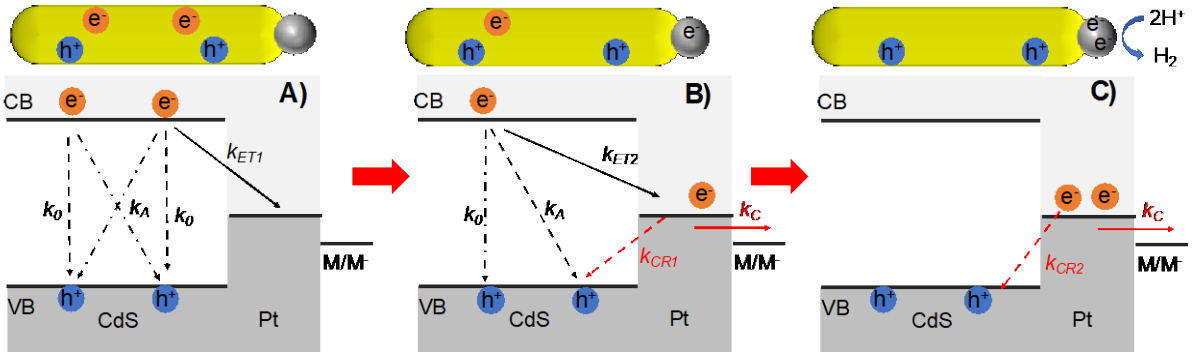

Figure 5.1. Key intermediates (top) and energy level diagrams and processes (bottom) involved in the transfer of two electrons from a bi-exciton state in CdS-Pt heterostructures. A) Transfer of the first electron from the biexciton state competes with intrinsic exciton recombination (k_0) and Auger recombination (k_A) of bi-exciton state. B) Transfer of the second electron from the charge separated state (a positive trion in the CdS and an electron in the Pt) competes with intrinsic exciton recombination (k_0), Auger recombination (k_A) of trion state and charge recombination (k_{CR1}). C)

In two-electron charge separated state, catalytical reactions (k_C) to reduce reactant M competes with charge recombination (k_{CR2}).

In this study, one-dimensional (1D) CdS-Pt nanorods (NRs) are used as a model nanocrystal/catalyst assembly to investigate the competition of charge separation from multi-exciton states with multiexciton auger recombination and charge recombination in multiple charge separated states. In CdS-Pt NRs, the CdS serves as the light absorber and the Pt tip acts as the electron acceptor and catalytic center to reduce protons to H_2. By excitation-fluence dependent transient absorption measurement, we examine how the Auger recombination rate in CdS NRs depends on the number of excitons per NR. In CdS-Pt NRs, electron transfer and charge recombination kinetics are measured as a function of average exciton number to determine the rate and efficiency of multiexciton dissociation and the decay rate and recombination mechanism of multiple-charge separated states.

5.2. Results

5.2.1 CdS NR Characterization

Phosphonate-capped CdS (Figure 5.2A) and CdS-Pt (Figure 5.2B) nanorods were synthesized as reported in literatures with slight modifications, as described in the Chapter 2.[31] According to transmission electron microscopy (TEM) images of CdS (Figure 5.2A and 5.2B), the average length and diameter of the CdS NR are 26.3±2.9 nm and 4.3±0.6 nm, respectively. Pt tips show two peaks in their diameter distributions: 0.8±0.4 nm for small tips and 2.9±0.6 nm for large tips (inset of Figure 5.2B). As previously reported, CdS nanorods are in Wurtzite structure and grow along the <001> direction, terminating with a Cd-rich and a S-rich end. Metal decomposition shows preferential growth on the S-rich end because of its lower ligand coverage.[61-62] Due to defects or the Pt precursor/CdS NR ratio, Pt can also be deposited on the Cd-rich ends. This results

in 50% nanorods with one small Pt tip (~ 1 nm in diameter) and 40% NRs with two Pt tips (a large tip of ~ 3 nm at the S-rich end and small tip of ~ 1 nm at the Cd-rich end). Negligible Pt clusters are observed at the CdS edges within the high-angle annular dark-field scanning transmission electron microscopy (HAADF-STEM) images (Figure 5.2B). The UV-vis absorption spectrum of CdS NRs (Figure 5.2C) shows clear exciton bands with the lowest energy 1Σ band at ~460 nm, consistent with the previous reports of CdS NRs of similar diameters.[63-64] The absorption spectrum within the energy window 2.5 eV to 3.5 eV (500 to 350 nm) can be fitted with four Gaussian peaks, as described in Appendix 1 and Figure A.5.1. The CdS-Pt NRs exhibit a broad Pt d-sp interband transition from the near IR to visible region in addition to the absorption features of CdS nanorods.[65] The absorption of the CdS-Pt can be well fit by the sum of CdS absorption and pure Pt particle absorption, as shown in the yellow curve in Figure 5.2C, indicating negligible modification of CdS exciton bands by the Pt tip.

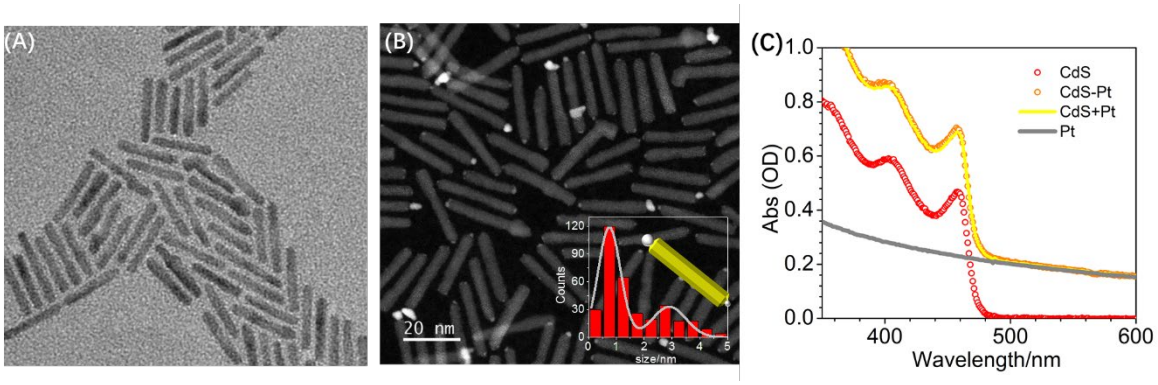

Figure 5.2. (A) TEM image of CdS NRs. (B) HAADF-STEM image of CdS-Pt. (Inset) Distribution of Pt tip diameters. (C) UV-Vis absorption spectra of CdS (red circles) and CdS-Pt (orange circles) NRs. Yellow solid line is a fit to the spectrum of CdS-Pt NRs by the sum of Pt (grey line) and CdS absorption spectra.

5.2.2 Single exciton dynamics in CdS and CdS-Pt NRs

We first examined the single exciton dynamics in CdS and CdS-Pt NRs dispersed in toluene by transient absorption (TA) spectroscopy, following previously reported methods.[66-68] The instrument response time of the measurement is ~ 140 fs and the details of the TA spectroscopy setup is described in chapter 2. Figure 5.3A shows the spectral evolution of the CdS NR at a 400 nm excitation fluence of 8 nJ/pulse, which corresponds to a pulse excitation energy density of 1.4 mW/cm^2 (beam diameter of ~600 micrometers) and an average initial exciton number per NR of <N>~0.2. The estimation of <N> is discussed in Appendix 4. Under this fluence, the TA signal is dominated by single exciton states. The TA spectra show three transient features: a) a bleach of 1Σ exciton band centered at 460 nm due to the electron state filling at the conduction band (CB) edge which reduces the 1Σ exciton absorption in excited NRs; b) an increased absorption at ~420 nm that is attributed to the red-shift of a higher energy transitions in the presence of 1Σ exciton (i.e. biexciton interaction); c) a weak broad absorption signal at 520-600nm (inset in Figure 5.3A) due to the photoinduced absorption (PA) signals of trapped holes in the NRs. Similar TA features have been reported and assigned previously in similar CdS NRs.[66-68] Spectral fitting of the exciton features in the TA spectra are described in Appendix 3 and shown in Figure A.5.4. It has been shown previously that the PA signal grows in with a time constant of ~0.8 ps due to fast valence band (VB) hole trapping, which forms a trapped exciton state with electron in the conduction band edge bound to the trapped hole. [38, 67] Thus, the kinetics of the CB electron can be followed by the time-dependent amplitude of the 1Σ exciton bleach as shown in Figure 5.3C. It can be fit to an exponential growth with a time constant of 91±4 fs, reflecting the relaxation of electrons from the initially excited levels to the conduction band edge, and a stretched exponential decay $\Delta A = e^{-\left(\frac{t}{\tau_1}\right)^{\beta}}$ with a time constant τ_1 of 102±1 ns and β=0.48, which corresponds to an average lifetime

of 204±2 ns for the recombination of the CB electron with trapped hole (process ii in Figure 5.3D).[38] The small decay of the CdS signal within 1 ps is previously attributed to the exciton localization from the CdS rod into the bulb region of a larger diameter.[66]

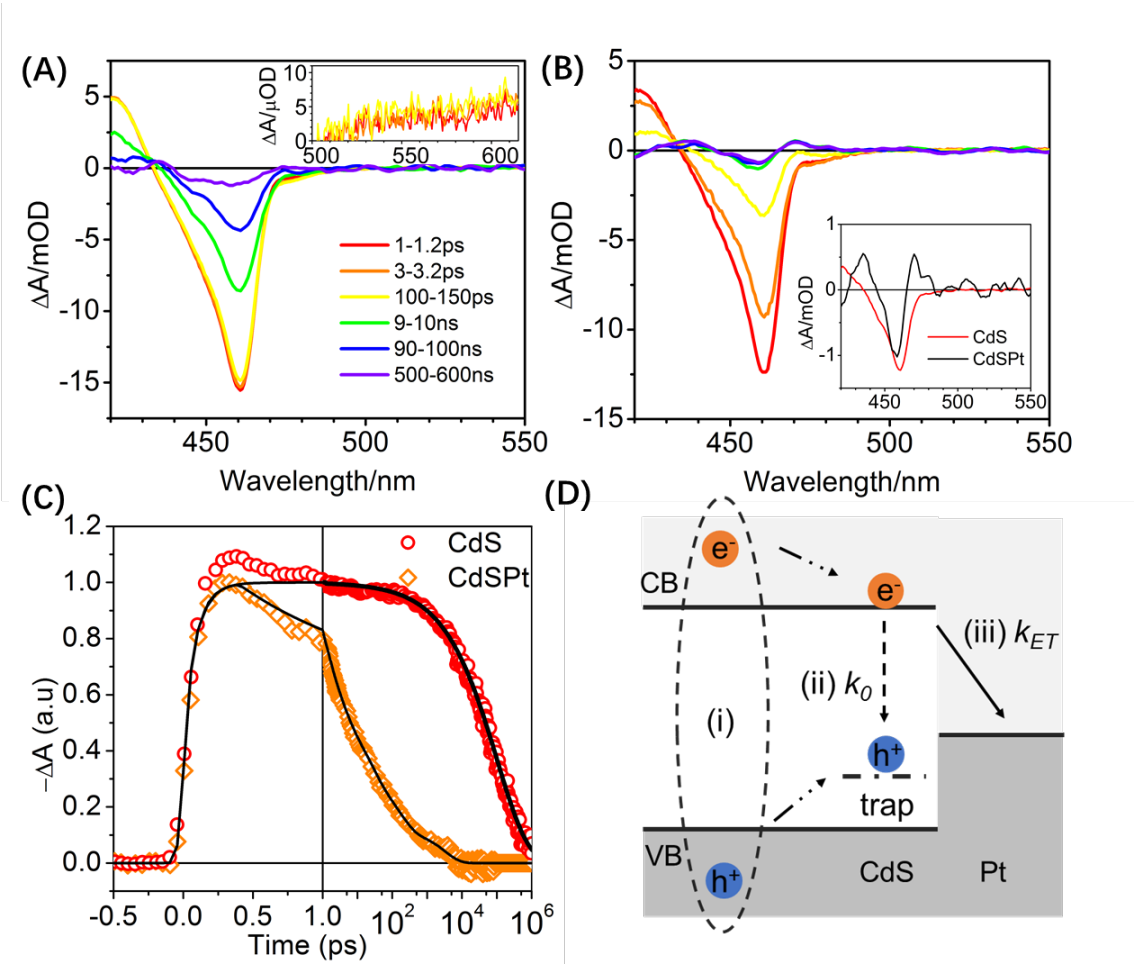

Figure 5.3. Single exciton dynamics in CdS and CdS-Pt NRs. (A) TA spectra of CdS NRs measured at an excitation fluence of 1.4 mW/cm^2 (average initial number of excitons per NR of <N>~0.2). Inset: expanded view of the PA spectral signature. (B) TA spectra of CdS-Pt NRs measured at an excitation fluence of 2.8 mW/cm^2 (<N>~0.3). Inset: comparison of scaled TA spectra of CdS and CdS-Pt at 9-10 ns. The derivative feature shown in CdS-Pt indicates the presence of a charge separated state. Selected time delays are same for (A) and (B) and are specified in (A). (C) Comparison of 1Σ exciton bleach recovery kinetics of CdS monitored at

bleach maximum ~461 nm and CdS-Pt NRs monitored at 466 nm. The TA signal of CdS-Pt at this wavelength, an isosbestic point of the charge separated state spectrum (inset of Figure 5.3B), contains only the exciton bleach amplitude, reflecting the kinetics of electron at the CdS conduction band edge. The faster exciton bleach recovery kinetics in CdS-Pt indicates electron transfer from the CdS to Pt. (D) Schematic energy level diagram of CdS-Pt NRs and key processes of photogenerated carriers: (i) Electron relaxation to the band edge (91±4 fs) and hole localization to the trap sites, (ii) exciton recombination (204±2 ns), (iii) Electron transfer from the CdS conduction band to the Pt tip (5.6±0.6 ps) and (iv) recombination of the electron in the Pt with the trapped hole in CdS.

The spectral evolution of CdS-Pt under single exciton condition (<N>~0.3) is plotted in Figure 5.3B. At early delay times (1-3 ps), the transient spectra show the same spectral features as CdS NRs. However, these features decay on a much faster time scale. At later delay times, after the decay of the CdS 1□exciton bleach, the TA spectra show a second derivative feature that differs from those in CdS NRs (inset of Figure 5.3B). This feature is assigned to the charge separated (CS) state signal, in which the remaining hole in the NR shifts the exciton transition energy, giving rise to the second derivative like TA difference signal.[38] The CS state spectrum shows a clear isosbestic point at 466 nm (with zero amplitude) and 1□exciton bleach kinetics at this wavelength can be used to follow the decay of the CB edge electrons in the CdS. The comparison of 1□exciton bleach recovery kinetics of CdS NRs a 461nm and CdS-Pt NRs at 466 nm measured under similar excitation fluence (Figure 5.3C) shows a faster bleach recovery in CdS-Pt, which can be attributed to electron transfer from the CdS conduction band edge to the Pt tip (i.e. process iii in Figure 5.3D). Multiexponential fit of the 1□exciton bleach recovery kinetics gives a half lifetime of electron transfer of 5.6±0.6 ps.

5.2.3 Auger recombination in CdS NRs

To investigate multiexciton dynamics, we have measured the transient spectra as a function of excitation fluence. Figure 5.4A shows the transient spectral evolution of CdS NRs with <N>~20. Compared to those at lower fluence (Figure 5.3A), these TA spectra shows larger bleach amplitudes and faster bleach recovery, as well as broaden exciton bleach spectra at the higher energy side of the 1Σ exciton band at early delay times. The difference in the TA spectra can be more clearly seen in Figure A.5.2A which compares the transient spectra at 0.5 ps for various excitation fluences. As shown in Figure A.5.3B, the initial 1Σ exciton bleach amplitude at 0.5-1 ps increases linearly for the excitation fluence from 1.4 mW/cm^2 to 8.4 mW/cm^2 and saturates at higher fluences, where the bleach amplitude equals the steady-state absorbance of the sample. The PA signal amplitude increases linearly with the pump fluence over the entire range (Figure A.5.3A), and reflects the linear increase of the total number of excitons in the NR. This indicates that at higher fluences, after the 1Σ exciton states are fully occupied, additional excitons occupy higher excitons states, which leads to the bleach at the higher energy side of the 1Σ band. A comparison of TA spectra at long delay time (50 ns) measured at different excitation fluences (Figure A.5.2B and C) shows that all these spectra are the same within a normalization factor, indicating that all multiple exciton states have decayed to the single exciton states in these NRs. As described in detail in Appendix 2 and shown in Figure A.5.3, from the excitation fluence dependence of PA and 1Σ exciton bleach signal, we can estimate the number of initial total number of excitons per NR <N> and 1Σ excitons at any fluences by assuming a Poisson distribution of total absorbed photons per NR. This analysis also shows the maximum number of 1Σ exciton to be ~ 6 at the saturation fluence. Our model assumes that each electron at the band edge contributes to the same

state filling exciton bleach signal amplitude in NRs, although it has been reported that in CdSe quantum dots that the biexciton state filling amplitude is only 1.6 times of the single exciton.[69]

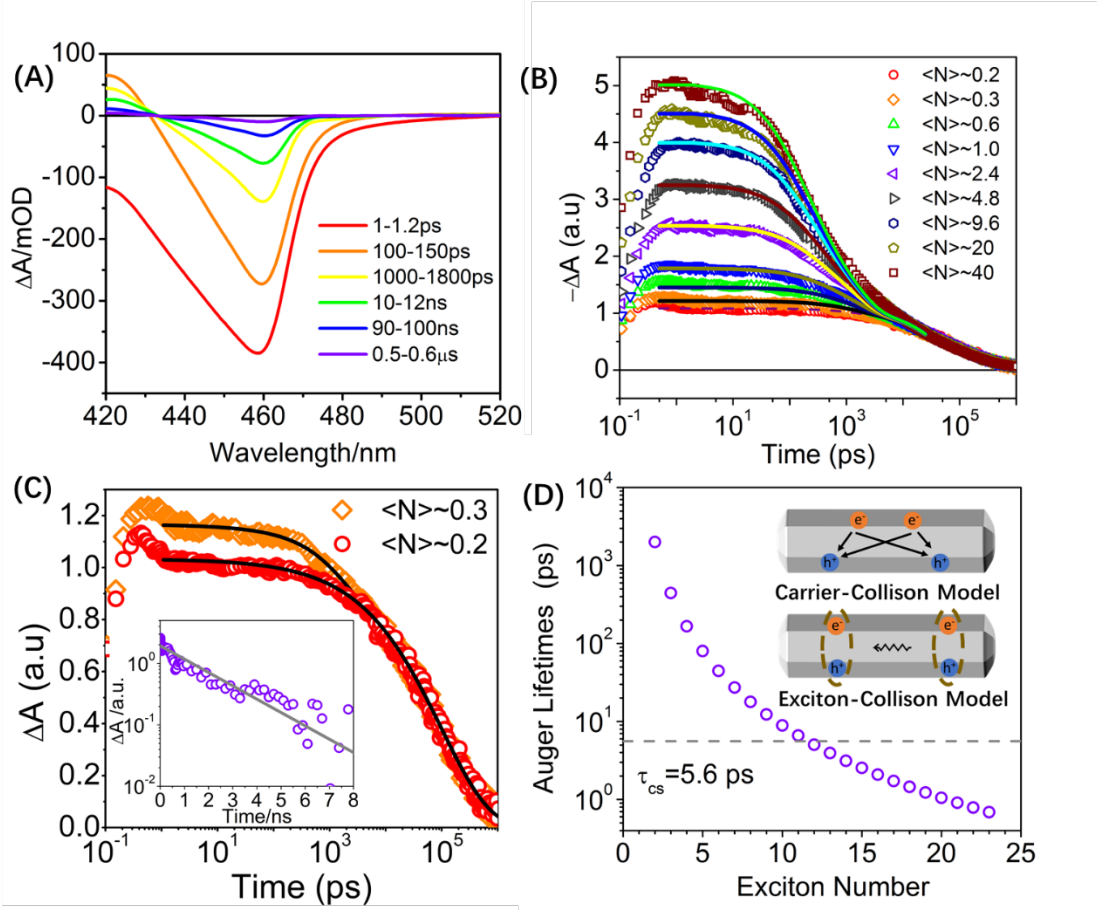

Figure 5.4. Multiple exciton dynamics in CdS NRs. (A) TA spectra of CdS NRs measured at excitation fluence of 175 mW/cm^2 (initial average number of excitons per NR of <N>~20) at selected delay times. (B) Comparison of normalized 1Σ exciton bleach recovery kinetics measured under various fluences (<N> ~0.2 to 40> and their fit according to the carrier-collision model described in the main text. These bleach kinetics have been normalized to the same amplitude at 100 ns, and show excellent agreement at 50 ns to 1 μs, when only single exciton states remain in these NRs. (C) Comparison of exciton bleach kinetics measured at <N>~0.2 (red circles) and <N>~0.3 (orange diamonds). (Inset) Biexciton decay kinetics (purple open circles) obtained by subtracting the normalized 1Σ exciton bleach kinetics measured at <N>~0.2 from that of <N>~0.3

and its fit to a single exponential decay function with a time constant of 2.0±0.2 ns (gray line). (D) Auger lifetime of N exciton states in CdS NRs obtained through the fit shown in Figure 5.4B according to carrier-collision model (purple open circles) and the charge separation half lifetime of a single exciton state in CdS-Pt (grey dashed line, from Figure 5.3C). (Inset) Scheme of the carrier-collision (top panel) and exciton-collision (bottom panel) models for multiexciton Auger recombination.

The fluence-dependent 1Σ bleach recovery kinetics of CdS NRs are compared in Figure 5.4B. These kinetics have been normalized to the same amplitude at 100 ns and show good agreement with each other on the 10 -500 ns time scale, indicating that at these long delay times all multiple states have decayed and only the single exciton state remain, consistent with the comparison of TA spectra shown in Figure A.5.2C. At higher excitation fluence, 1Σ bleach recovery kinetics show a larger amplitude of fast decay components at < 10 ns, indicative of multi-exciton decay by Auger recombination, in which an exciton decays by exciting another carrier (electron or hole) to a higher energy level.

The population kinetics of the n exciton state (X_n) can be described by the cascade decay model, in which n exciton states decay to the n-1 exciton states until reaching the ground (n=0) state, as shown in Figure A.5.5. This population kinetics of n exciton states is described in equation (eq). 5.1:

$$\frac{dX_n(t)}{dt} = k_{n+1}X_{n+1}(t) - k_nX_n(t) \qquad (5.1)$$

The transient 1Σ exciton bleach amplitude can be related to the population of n exciton states by eq. 5.2:

$$\Delta A(t) = \sum_{n=1}^{5} nX_n(t) + 6[1 - \sum_{n=1}^{5} X_n(t)] \qquad (5.2)$$

The first term in eq. 5.2 represents the contribution of n=1 to n=5 exciton states, in which n exciton leads to the n/6 bleach of the 1Σ exciton transition, and the second term is the contribution of n>5 exciton states, which leads to the complete bleach of the 1Σ exciton transition.

The decay rate of single exciton states(k_1) has been determined above by the measurement at low fluence when biexciton and higher exciton state populations are negligible (Figure 5.3C). k_2^A can also be determined at low excitation fluence, when transient signal is dominated by n=1 and 2 states. As shown in Figure 5.4C, by subtracting the 1Σ exciton bleach kinetics measured at <N>~0.2 from that of <N>~0.3, the biexciton recombination can be obtained with a single exponential lifetime of 2.0±0.2 ns, as shown in the inset in Figure 5.4C. The biexciton lifetime is more than one order of magnitude shorter than a quarter of the average single exciton lifetime, $\tau_1/4$ ~50ns. The latter is the estimated lifetime of biexciton states if electron-hole pairs undergo two-particle recombination without the contribution of Auger recombination pathways.[70] This suggests that the biexciton recombination in CdS NRs is dominated by the Auger recombination pathways.

The Auger recombination rate constant for an n exciton state (k_n^A) can be related to that of a biexciton state (k_2^A) through a scaling relationship that accounts for the ratio of all possible three-particle (i.e. an electron-hole pair plus an additional e or h) Auger recombination processes. For Auger recombination that involves the collision of independently moving electrons and holes (referred to as Carrier-Collision Model), such as in 0D quantum dots, Auger recombination rate constant has been shown to follow a scaling relationship of $\frac{k_n^A}{k_2^A} = \frac{n^2(n-1)}{4}$.[28] In 1D or 2D nanostructures, such as polyethylenimine-capped CdS, CdSe nanorods and nanoplatelets, the Auger recombination rate constant has been shown to follow a different scaling relationship,$\frac{k_n^A}{k_2^A} = \frac{n(n-1)}{2}$, which reflects that electrons and holes move as a pair (exciton) and Auger recombination

involves the collision of 2 excitons (referred to as Exciton-Collision Model).[16, 71-72] These two pathways are illustrated in the inset of Figure 5.4D. With independently determined k_2^A *and* k_1 values, the 1Σ exciton bleach kinetics shown in Figure 5.4B can be fit by eqs. (5.1) and (5.2) to evaluate how the lifetime of multiple exciton states scale with n. It is assumed that at t=0, the exciton distribution follows the Poisson statistics, $X_n(t=0) = \frac{<N>^n e^{-<N>}}{n!}$, and <N> is the average number of excitons per NR at t=0. As shown in Figure 5.4B, the excitation power dependent 1Σ exciton bleach kinetics can be well fit to the Carrier-Collision Model. These kinetics cannot be adequately described by the Exciton-Collision Model (Figure A.5.6). The lifetimes of n exciton states estimated using the Carrier-Collision model are plotted in Figure 5.4D. It has been reported previously that the multiple exciton decay rate constants of CdSe NRs dispersed in organic solvents follows the Exciton-Collision model.[72-73] Furthermore, the biexciton lifetimes of CdSe NRs with a similar morphology (diameter of 4.6 nm and length of 29 nm) was reported to be ~260 ps, [73], which is an order of magnitude shorter than the biexciton lifetime of CdS NRs.. We hypothesize that because of the fast hole trapping, excitons in CdS NRs are localized to hole trap sites, in which the hole mobility is low and electron can move on a much faster time scale by thermal ionization from the hole. As a result, electrons and holes do not move as bound excitons and Auger recombination can be described by the Carrier-Collision Model. The trapped holes also slow down the biexciton Auger recombination rate. A similar idea has been proposed in a recent study of the effect of hole trapping on Auger recombination lifetime in QDs.[56] A recent study of polyethylenimine-capped CdS NRs (diameter of 4.2 nm and length of 49 nm) dispersed in water has reported a biexciton lifetime of 180 ps and multi-exciton lifetimes that follow the biexciton collision model, differing significantly from this work.[16] These samples differ from our work (phosphonic acid capped CdS NRs dispersed in toluene) in both the capping ligand and solvent.

To allow better comparison, we also measured the multiexciton lifetimes of the same CdS NRs capped with 11-mercaptoundecanoic acid (MUA) and dispersed in water, as discussed in Appendix 5. The biexciton lifetime of these NRs is 165±26 ps, much shorter than that in organic solvent and is closer to that for polyethylenimine capped CdS NRs dispersed in water. [16] Interestingly, multi-exciton lifetimes can be fit equally well to both the Carrier and Exciton Collision models. These results suggest that the multi-exciton Auger recombination process of NRs depends sensitively on their chemical composition and the solvent environment, although the mechanisms of such dependences remained to further examined.

The decay of exciton in energy levels above 1Σ results in the fast decay of the exciton bleach on the higher side and faster decays of the PA signals than the 1Σ exciton bleach at early delay times (Figure A.5.7). At later times, the decay of PA signal agrees with the 1Σ exciton bleach, when only band edge excitons remain, as indicated by process iii) to iv) in Figure A.5.5 (Appendix 4). The recombination of excitons above the 1Σ level can be analyzed from the decay of PA signals (process (i) to (iii) in Figure A.5.5). As shown in Figure A.5.7, these PA decay kinetics can also be qualitatively accounted for by the Carrier-Collision Model, although the agreement is not as good as the fit to band edge exciton states, which may suggest a different scaling law for the Auger recombination rate of these higher energy exciton states.[74]

5.2.4 Multiexciton dissociation in CdS-Pt NRs

The results in Figure 5.4D show that the lifetime of multiple exciton states in CdS NRs ranges from ~0.7 ps for the 20 exciton states to ~ 2 ns for the biexciton states. For exciton number below 11, their Auger lifetimes are longer than the electron transfer halftime (~5.6 ps) from the CdS to Pt in CdS-Pt NRs measured under single exciton condition, suggesting the possibility of multiexciton dissociation by transferring multiple electrons to the Pt tip. To examine the

multiexciton dissociation kinetics, we carried out transient absorption study of CdS-Pt heterostructures as a function of 400 nm excitation fluence. The spectral evolution of CdS-Pt under high excitation fluence (<N>~20) is plotted in Figure 5.5A for delay times from 1 ps to 2 ns. Compared to the transient spectra of CdS NRs under the same excitation fluence (Figure 5.4A), the TA spectra show similar XB spectral features at early decay times, but decay on a faster time scale, indicative of electron transfer. The transfer kinetics of the CdS conduction band edge electrons in the multiple exciton states can be followed by the 1Σ exciton bleach decay kinetics of CdS-Pt at 466 nm, which is compared in Figure 5.5B for excitation fluences from <N>~0.3 to <N>~22.9. These XB recovery kinetics, normalized at 20 ps-100 ns to facilitate comparison, show similar decays, independent of the excitation fluence. Also shown (black solid line) for comparison is the 1Σ exciton XB kinetics of CdS NRs (without Pt) at <N>~20, which shows that XB in CdS-Pt NRs under all fluences decay much faster than that in CdS NRs at the highest fluence. The XB decay kinetics reflects the decay of CdS conduction band edge electrons and are sensitive to the decay of multiple exciton states with n<7. These results suggest that electron transfer from the CdS conduction band edge to Pt in CdS-Pt NRs out-competes exciton Auger recombination to achieve efficient multiple electron transfer for n<7 exciton states. However, the XB decay is not sensitive to the decay of n=7 or higher exciton states. As shown in Figure 5.4D, the Auger recombination in these higher states (n>11) become faster than the ET time, which would reduce the multiple exciton dissociation efficiency. The kinetics at higher fluence shows an additional fast recovery component with decay time of ~ 2.6 ps (Figure A.5.10), which is likely caused by multiple exciton induced spectral shift at early delay time. Such spectral shift exists at high excitation fluence (Figure 5.5A) and may lead to additional change of XB amplitudes monitored at 466 nm that are not related to electron transfer.

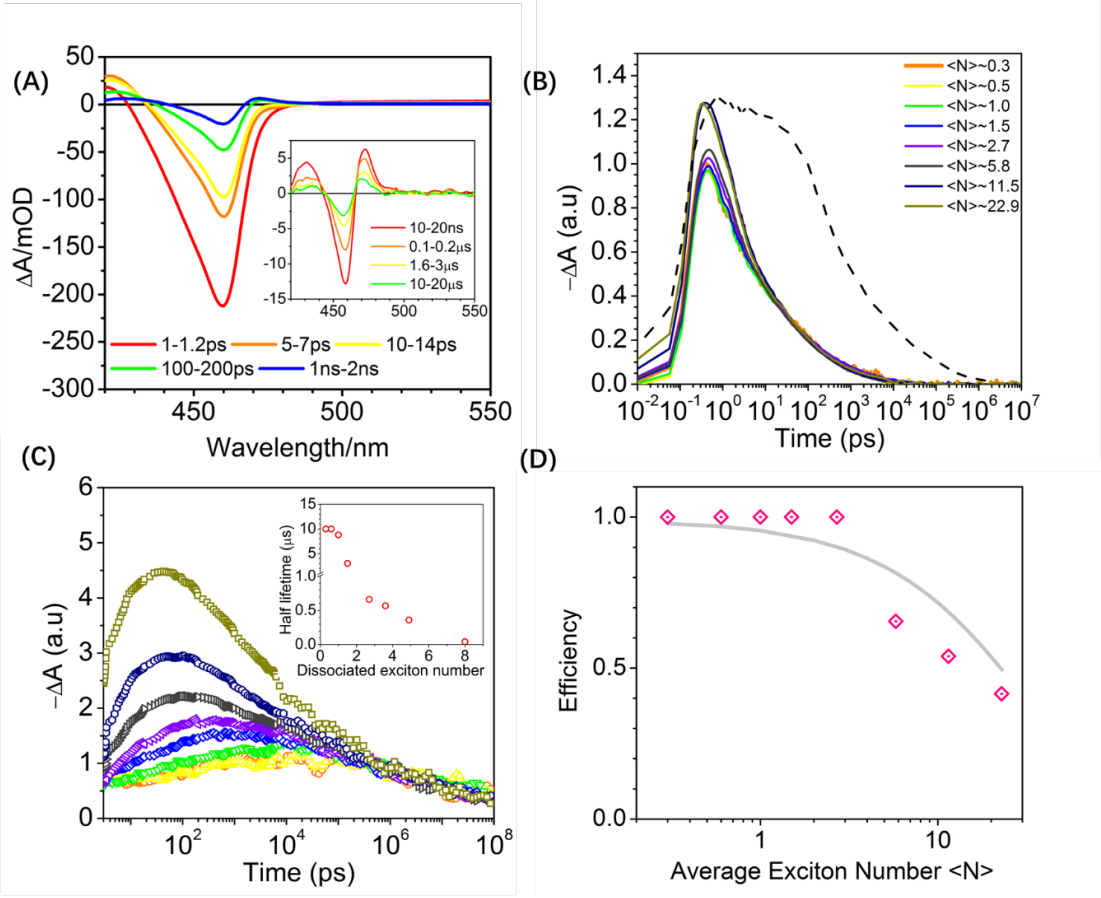

Figure 5.5. Multiple exciton dissociation in CdS-Pt NRs. (A) TA spectra of CdS-Pt NRs measured at an initial average number of excitons per NR of <N>~22.9 at 1 ps -2 ns after 400 nm excitation. Inset: same data at longer delay time (10 ns – 20 μs). (B) Normalized comparison of 1Σ exciton bleach recovery kinetic (at 466 nm) measured under excitation fluences from <N>~0.3 to <N>~22.9 (Colored solid lines). These kinetics are normalized to the same amplitude at delay time > 20 ps to facilitate comparison. Also shown is the 1Σ exciton bleach of CdS NRs measured <N>~20 (black dashed line). (C) Comparison of normalized charge separated (CS) state decay (i.e. charge recombination) kinetics for CdS-Pt NRs measured at different excitation fluences (open circles). The CS state population is obtained by subtracting the CdS 1Σ exciton bleach contribution (from Figure 5.5B) from the total TA signal at 472 nm to obtain the CS state signal. These kinetics have been normalized to the same amplitude at 10^6-10^8 ps. Each color represents a different <N>, same

as those shown in Figure 5.5B. (Inset) Half lifetime of charge separated state recombination versus the total number of dissociated exciton. (D) Estimated exciton dissociation efficiency (pink diamonds) as a function of average initial exciton number per NR <N>. The gray curve represents the estimated dissociation efficiency according to a model that accounts for the competition of multiple electron transfer with Auger recombination, discussed in Appendix 6.

The amount of transferred electrons can be determined from the amplitude of the charge separated state signal, which shows a peak at 472 nm. Because the TA signal at 472 nm contains both CS state signal as well as CdS exciton bleach at early times, the latter is subtracted from the total signal to obtained pure CS state signal as described in Appendix 6 and Figure A.5.11. The subtracted kinetics at 472 nm, representing the CS state signal, has been normalized and compared in Figure 5.5C. The normalized kinetics at different fluences show good agreement with each other at delay time of 10^5-10^8 ps, suggesting that multiple charge separated states have recombined and only single charge separated state remain at these long delay times.

To determine the number of total dissociated excitons, we analyzed the maximum amplitude of the charge separated (CS) state signal at 472 nm as a function of the excitation fluence. As shown in Figure A.5.12A-D, in the single exciton condition, the CS state signal reaches its peak amplitude when the XB recovery is completed, suggesting the peak CS state amplitude should reflect the total number of transferred electrons before charge recombination occurs (see below). Furthermore, as shown in Figure A.5.16, fitting of the charge separated state spectra at 6.3 ns shows that their spectral shape is independent of the excitation fluence, suggesting that the peak amplitude of the CS state signal should scale linearly with the number of separated charges. The peak CS state signal amplitudes at 472 nm as a function of pump fluences are plotted in Figure A.5.13. For each fluence, the average number of initial excitons per NR has also been determined

(Appendix 2). The number of separated charges at each fluence can be calculated from the peak CS signal amplitude using the linear relationship between these quantities and the fact that at the lowest fluence (single exciton conditions) the exciton dissociation efficiency is nearly 100% (Figure 5.3C). The measured number of dissociated excitons as a function of total average number of initial excitons per NR is shown in Figure A.5.13 and the calculated multiexciton dissociation efficiency is shown in Figure 5.5D. It shows the charge separation efficiency maintains 100% with <N> up to 2.7 excitons per nanorod and decreases at higher fluence due to the competition multi-exciton Auger recombination. Under the highest fluence, where 22.9 excitons are generated per nanorod, dissociation of 9.5 excitons is observed, corresponding to an efficiency at 41%. This indicates that some of higher energy excitons (above the band edge) can also be dissociated. The dissociation efficiency of n-exciton state can also be estimated using the measured n-exciton state Auger recombination rate and the fluence independent charge separation rate, as described in Table A.5.4 and Appendix 6. Thus, the average exciton dissociation efficiency for each excitation flux (or average <N>) can be calculated, as shown by the gray curve in Figure 5.5D. Its trend is qualitatively consistent with the measured charge separation efficiency. The predicted efficiencies under high fluences are slightly larger than the values calculated from the measured values. This may be attributed to the underestimate of the initial signal amplitudes as described in Appendix 6 and shown in Figure A.5.11.

5.2.5 Charge separated state recombination in CdS-Pt NRs

The lifetime of charge separated state is also of great importance as charge transfer lifetime, as it limits the overall efficiency of slow catalysis systems.[75] However, its fluence-dependent behavior has not been clearly addressed before. In CdS-Pt NRs, it can be determined from the decay of the CS kinetics shown in Figure 5.5C. With increasing excitation fluence, initial decay

of the CS state becomes faster, which is attributed to recombination in charge separated states with multiple electrons in Pt and holes in CdS NRs. The estimated half lifetimes of the charge separated state decreases at larger number of dissociated excitons, as shown in Figure 5.5C inset. In single charge separated state <N>~0.3 and 0.6, the half lifetime is estimated to be around 10 μs. At <N>~22.9, when 9.5 excitons are dissociated, the charge recombination half-life decreases to 42 ns. As shown in Figure A.5.17, the fluence dependent charge recombination kinetics at 472 nm can also be fitted by an empirical cascade decay model described in eq. A.5.6.1-3 and Appendix 8. The model assumes n-charge separated state decays by recombining one electron in Pt with one hole in CdS to form n-1 charge separated state. The best fit reveals that the recombination rate constant scales with $n^{3.5}$, $\frac{\tau_n^R}{\tau_2^R} = \left(\frac{n}{2}\right)^{-3.5}$, where τ_n^R is the recombination time of the CS state with n -pair of separated electrons and holes and $\tau_2^R = 90$ ns. The physical meaning of this scaling law remains unclear to us.

Our observation of fluence independent band edge exciton dissociation in CdS-Pt differs significantly from a recent report of multiple exciton dissociation in CdSe/CdS-Pt NR, in which the first electron transfer is report to occur with a time constant of 192 ps, while the second electron transfer is slowed by the trion Coulombic interaction down to 1700 ps.[55] One key difference is that in CdSe/CdS-Pt, the excitons are localized in the CdSe seed, which upon the dissociation of the first exciton generates a trion state with increased Coulomb binding energy. In multiple exciton states in CdS-Pt NRs, excitons are spatially separated due to the spatial separation of the trapped holes. This gives rise to the exceptionally long biexciton lifetime of 2.0±0.2 ns for CdS NRs compared to CdSe NRs or CdSe/CdS dot-in-rod NRs,[55, 76] and a lack of dependence of electron transfer rate with the number of excitons on the CdS NR.

Our findings are consistent with a recent study of the fluence-dependence of multiexciton dissociation kinetics in Au tipped CdS NRs.[16] It was observed that with larger gold tips (diameter ~ 7.1 nm), the ultrafast electron transfer process outcompetes the Auger recombination and 1Σ exciton bleach recovery shows fluence-independent kinetics; and with a smaller Au tip size (diameter ~ 1.5 nm), ET is slower and is outcompeted by Auger recombination at high fluences. In our CdS-Pt samples, despite a large distribution of Pt diameters (from ~0.8 to ~2.9 nm), the ET rates of band edge excitons are much faster than their Auger recombination rates (Figure 5.4D), which leads to fluence independent band exciton decay kinetics, consistent with their observation of the sample of large Au tips. These different size-dependent behaviors can be attributed to much faster ET rates and slower exciton Auger recombination rates of our CdS-Pt NRs in toluene compared to previous CdS-Au NRs in water.[16, 22] In the previous study of CdS-Au NRs with large Au tip (7.1 ± 0.8 nm), the transfer times of band edge and hot electrons were estimated to be ~ 44 ps and 0.25 ps, respectively, by the fitting of band edge exciton decay kinetics.[16] In our estimate the multiexciton dissociation efficiency (Figure 5.5D), we assume that the electron transfer rate from states above 1Σ is same as band edge electrons. This assumption is based on the consideration that the CdS CB edge is at ~ -2 eV (~ -4 eV versus vacuum level)[22] above the Pt Fermi level (-6 eV)[77] and the Pt densities of states for hot and band edge electron transfer from the CdS are similar. Assuming a faster hot electron transfer rate in our analysis would increases the multiple exciton dissociation efficiency at high fluences, which would further deviate from the experimental observations (Figure 5.5D). Unfortunately, due to lack of spectroscopic signal of the electrons above 1Σ, we are unable to directly measure the rate of hot electron transfer into Pt and the energy dependence of electron transfer rate remains an open questions.

Efficient separation of multiple electron-hole pairs in CdS-Pt NRs provides interesting possibility of designing hydrogen evolution catalysts suitable for intense light illumination conditions. Under AM 1.5 condition (assume absorption cut-off by CdS at 580 nm), each nanorod absorbs one photon per ~700 μs; accumulation of two electrons at the Pt requires sequential absorption of two photons, coupled with efficient hole removal.[36] Our result shows that under intense illumination, the CdS-Pt NR can transfer two or more electrons simultaneously, avoiding the need of sequential absorption of photons and sequential separation of single excitons. However, our finding also indicates that the lifetime of multiple-charge separated states decrease sharply with the increasing number of separated electron-hole pairs (n). In CdS-Au system, an decrease of H_2 production quantum efficiency was reported under high fluences due to competition between electron transfer and Auger recombination. Faster charge-separated state recombination can further hinder its performance under intense illumination. Thus, such system would require fast hole removable from the CdS and/or the stabilization of the electrons in metal domains by protons or ions to suppress accelerated recombination, which is of equal importance of addressing the competition between electron transfer and Auger recombination.

5.3 Conclusion

We have studied multiple electron transfer from the CdS NR to the Pt tip in multiexciton states in CdS-Pt NRs and the competitive exciton Auger recombination and charge recombination processes. The Auger recombination rate of n-exciton states in CdS NRs follows the Carrier-Collison model with $\frac{k_n^A}{k_2^A} = \frac{n^2(n-1)}{4}$ and $1/k_2^A$ of 2.0±0.2 ns. The Auger rates are slower than and scaling relationship differ from CdSe NRs, which can be attributed to the rapid trapping of excitons in CdS NRs. Electron transfer from the CdS NR to the Pt tip was found to show a half-life of

5.6±0.6 ps and the transfer kinetics shows negligible dependence on the number of excitons in CdS NRs. Because the lifetime of the multiple exciton states decreases from 2ns in biexciton state to ~0.7 ps in multiexciton states with <N>=22.9, multiexciton dissociation efficiency decreases at higher <N>, from ~100% in biexciton states to ~ 41% at <N> = 22.9. The charge separated state decay by recombination of the transferred electrons in the Pt with the holes in CdS, and the half lifetime of the charge separated state decreases from 10 μs with single e-h pair to 42 ns with ~9 e-h pairs. The ability of CdS-Pt nanorods to efficiently absorb multiple photons simultaneously and transfer multiple electrons to Pt suggests the possibility of driving multiple electron photoreduction reactions under conditions significantly different from the 1 sun illumination, which may offer a way to control the branching ratio of reactions that require different number of electrons.

References

1. Amirav, L.; Alivisatos, A. P., Photocatalytic Hydrogen Production with Tunable Nanorod Heterostructures. *J. Phys. Chem. Lett.* **2010**, *1*, 1051-1054.
2. Ahmed, M. E.; Dey, S.; Darensbourg, M. Y.; Dey, A., Oxygen-Tolerant H2 Production by [Fefe]-H2ase Active Site Mimics Aided by Second Sphere Proton Shuttle. *J. Am. Chem. Soc.* **2018**, *140*, 12457-12468.
3. Fujishima, A.; Honda, K., Electrochemical Photolysis of Water at a Semiconductor Electrode. *Nature* **1972**, *238*, 37-38.
4. Sun, L.; Hammarström, L.; Åkermark, B.; Styring, S., Towards Artificial Photosynthesis: Ruthenium–Manganese Chemistry for Energy Production. *Chem. Soc. Rev.* **2001**, *30*, 36-49.
5. Sheng, H.; Oh, M. H.; Osowiecki, W. T.; Kim, W.; Alivisatos, A. P.; Frei, H., Carbon Dioxide Dimer Radical Anion as Surface Intermediate of Photoinduced Co2 Reduction at Aqueous Cu and Cdse Nanoparticle Catalysts by Rapid-Scan Ft-Ir Spectroscopy. *J. Am. Chem. Soc.* **2018**, *140*, 4363-4371.
6. Chang, X.; Wang, T.; Gong, J., Co2 Photo-Reduction: Insights into Co2 Activation and Reaction on Surfaces of Photocatalysts. *Energy Environ. Sci.* **2016**, *9*, 2177-2196.
7. Wang, W. N.; An, W. J.; Ramalingam, B.; Mukherjee, S.; Niedzwiedzki, D. M.; Gangopadhyay, S.; Biswas, P., Size and Structure Matter: Enhanced Co2 Photoreduction Efficiency by Size-Resolved Ultrafine Pt Nanoparticles on Tio2 Single Crystals. *J. Am. Chem. Soc.* **2012**, *134*, 11276-81.
8. Costentin, C.; Drouet, S.; Passard, G.; Robert, M.; Savéant, J.-M., Proton-Coupled Electron Transfer Cleavage of Heavy-Atom Bonds in Electrocatalytic Processes. Cleavage of a C–O Bond in the Catalyzed Electrochemical Reduction of Co2. *J. Am. Chem. Soc.* **2013**, *135*, 9023-9031.

9. Brown, K. A., et al., Light-Driven Dinitrogen Reduction Catalyzed by a Cds:Nitrogenase Mofe Protein Biohybrid. *Science* **2016**, *352*, 448-450.
10. Pappas, I.; Chirik, P. J., Catalytic Proton Coupled Electron Transfer from Metal Hydrides to Titanocene Amides, Hydrazides and Imides: Determination of Thermodynamic Parameters Relevant to Nitrogen Fixation. *J. Am. Chem. Soc.* **2016**, *138*, 13379-13389.
11. Li, X.; Yu, J.; Jaroniec, M.; Chen, X., Cocatalysts for Selective Photoreduction of Co2 into Solar Fuels. *Chem. Rev.* **2019**, *119*, 3962-4179.
12. Guo, W.; Zhang, K.; Liang, Z.; Zou, R.; Xu, Q., Electrochemical Nitrogen Fixation and Utilization: Theories, Advanced Catalyst Materials and System Design. *Chem. Soc. Rev.* **2019**, *48*, 5658-5716.
13. Cui, X.; Tang, C.; Zhang, Q., A Review of Electrocatalytic Reduction of Dinitrogen to Ammonia under Ambient Conditions. *Adv. Energy Mater.* **2018**, *8*, 1800369.
14. Chica, B.; Ruzicka, J.; Kallas, H.; Mulder, D. W.; Brown, K. A.; Peters, J. W.; Seefeldt, L. C.; Dukovic, G.; King, P. W., Defining Intermediates of Nitrogenase Mofe Protein During N2 Reduction under Photochemical Electron Delivery from Cds Quantum Dots. *J. Am. Chem. Soc.* **2020**, *142*, 14324-14330.
15. Brown, K. A.; Ruzicka, J.; Kallas, H.; Chica, B.; Mulder, D. W.; Peters, J. W.; Seefeldt, L. C.; Dukovic, G.; King, P. W., Excitation-Rate Determines Product Stoichiometry in Photochemical Ammonia Production by Cds Quantum Dot-Nitrogenase Mofe Protein Complexes. *ACS Catal.* **2020**, *10*, 11147-11152.
16. Ben-Shahar, Y.; Philbin, J. P.; Scotognella, F.; Ganzer, L.; Cerullo, G.; Rabani, E.; Banin, U., Charge Carrier Dynamics in Photocatalytic Hybrid Semiconductor-Metal Nanorods: Crossover from Auger Recombination to Charge Transfer. *Nano Lett.* **2018**, *18*, 5211-5216.
17. Huynh, M. H. V.; Meyer, T. J., Proton-Coupled Electron Transfer. *Chem. Rev.* **2007**, *107*, 5004-5064.
18. Pannwitz, A.; Wenger, O. S., Photoinduced Electron Transfer Coupled to Donor Deprotonation and Acceptor Protonation in a Molecular Triad Mimicking Photosystem Ii. *J. Am. Chem. Soc.* **2017**, *139*, 13308-13311.
19. Nomrowski, J.; Wenger, O. S., Exploiting Potential Inversion for Photoinduced Multielectron Transfer and Accumulation of Redox Equivalents in a Molecular Heptad. *J. Am. Chem. Soc.* **2018**, *140*, 5343-5346.
20. Alivisatos, A. P., Semiconductor Clusters, Nanocrystals, and Quantum Dots. *Science* **1996**, *271*, 933-937.
21. Kalisman, P.; Nakibli, Y.; Amirav, L., Perfect Photon-to-Hydrogen Conversion Efficiency. *Nano Lett.* **2016**, *16*, 1776-1781.
22. Ben-Shahar, Y.; Scotognella, F.; Kriegel, I.; Moretti, L.; Cerullo, G.; Rabani, E.; Banin, U., Optimal Metal Domain Size for Photocatalysis with Hybrid Semiconductor-Metal Nanorods. *Nat. Commun.* **2016**, *7*, 10413.
23. Nozik, A. J., Multiple Exciton Generation in Semiconductor Quantum Dots. *Chem. Phys. Lett.* **2008**, *457*, 3-11.
24. Sambur, J. B.; Novet, T.; Parkinson, B. A., Multiple Exciton Collection in a Sensitized Photovoltaic System. *Science* **2010**, *330*, 63-66.
25. Beard, M. C.; Knutsen, K. P.; Yu, P.; Luther, J. M.; Song, Q.; Metzger, W. K.; Ellingson, R. J.; Nozik, A. J., Multiple Exciton Generation in Colloidal Silicon Nanocrystals. *Nano Letters* **2007**, *7*, 2506-2512.

26. Zhu, H.; Yang, Y.; Wu, K.; Lian, T., Charge Transfer Dynamics from Photoexcited Semiconductor Quantum Dots. *Annu. Rev. Phys. Chem.* **2016**, *67*, 259-281.
27. Beard, M. C., Multiple Exciton Generation in Semiconductor Quantum Dots. *J. Phys. Chem. Lett.* **2011**, *2*, 1282-1288.
28. Klimov, V. I., Multicarrier Interactions in Semiconductor Nanocrystals in Relation to the Phenomena of Auger Recombination and Carrier Multiplication. *Annu. Rev. Condens. Matter Phys.* **2014**, *5*, 285-316.
29. Timmerman, D.; Izeddin, I.; Stallinga, P.; Yassievich, I. N.; Gregorkiewicz, T., Space-Separated Quantum Cutting with Silicon Nanocrystals for Photovoltaic Applications. *Nature Photonics* **2008**, *2*, 105-109.
30. Milstein, T. J.; Kroupa, D. M.; Gamelin, D. R., Picosecond Quantum Cutting Generates Photoluminescence Quantum Yields over 100% in Ytterbium-Doped Cspbcl3 Nanocrystals. *Nano Lett.* **2018**, *18*, 3792-3799.
31. Habas, S. E.; Yang, P.; Mokari, T., Selective Growth of Metal and Binary Metal Tips on Cds Nanorods. *J. Am. Chem. Soc.* **2008**, *130*, 3294-3295.
32. Berr, M. J.; Wagner, P.; Fischbach, S.; Vaneski, A.; Schneider, J.; Susha, A. S.; Rogach, A. L.; Jackel, F.; Feldmann, J., Hole Scavenger Redox Potentials Determine Quantum Efficiency and Stability of Pt-Decorated Cds Nanorods for Photocatalytic Hydrogen Generation. *Appl. Phys. Lett.* **2012**, *100*, 223903.
33. Han, Z.; Qiu, F.; Eisenberg, R.; Holland, P. L.; Krauss, T. D., Robust Photogeneration of H2 in Water Using Semiconductor Nanocrystals and a Nickel Catalyst. *Science* **2012**, *338*, 1321-1324.
34. Li, Q.; Zhao, F.; Qu, C.; Shang, Q.; Xu, Z.; Yu, L.; McBride, J. R.; Lian, T., 2d Morphology Enhances Light-Driven H2 Generation Efficiency in Cds Nanoplatelet-Pt Heterostructures. *J. Am. Chem. Soc.* **2018**, 11726–11734.
35. Kalisman, P.; Nakibli, Y.; Amirav, L., Perfect Photon-to-Hydrogen Conversion Efficiency. *Nano Letters* **2016**, *16*, 1776-1781.
36. Simon, T., et al., Redox Shuttle Mechanism Enhances Photocatalytic H2 Generation on Ni-Decorated Cds nanorods. *Nature Materials* **2014**, *13*, 1013.
37. Wu, K.; Lian, T., Quantum Confined Colloidal Nanorod Heterostructures for Solar-to-Fuel Conversion. *Chem. Soc. Rev.* **2016**, *45*, 3781-3810.
38. Wu, K.; Zhu, H.; Liu, Z.; Rodriguez-Cordoba, W.; Lian, T., Ultrafast Charge Separation and Long-Lived Charge Separated State in Photocatalytic Cds-Pt Nanorod Heterostructures. *J. Am. Chem. Soc.* **2012**, *134*, 10337-10340.
39. Martindale, B. C. M.; Hutton, G. A. M.; Caputo, C. A.; Reisner, E., Solar Hydrogen Production Using Carbon Quantum Dots and a Molecular Nickel Catalyst. *J. Am. Chem. Soc.* **2015**, *137*, 6018-6025.
40. Meng, P.; Wang, M.; Yang, Y.; Zhang, S.; Sun, L., Cdse Quantum Dots/Molecular Cobalt Catalyst Co-Grafted Open Porous Nio Film as a Photocathode for Visible Light Driven H2 Evolution from Neutral Water. *J.Mater.Chem.A* **2015**, *3*, 18852-18859.
41. Kuehnel, M. F.; Orchard, K. L.; Dalle, K. E.; Reisner, E., Selective Photocatalytic Co2 Reduction in Water through Anchoring of a Molecular Ni Catalyst on Cds Nanocrystals. *J. Am. Chem. Soc.* **2017**, *139*, 7217-7223.
42. Huang, J.; Mulfort, K. L.; Du, P.; Chen, L. X., Photodriven Charge Separation Dynamics in Cdse/Zns Core/Shell Quantum Dot/Cobaloxime Hybrid for Efficient Hydrogen Production. *J. Am. Chem. Soc.* **2012**, *134*, 16472-16475.

43. Sakimoto, K. K.; Kornienko, N.; Yang, P., Cyborgian Material Design for Solar Fuel Production: The Emerging Photosynthetic Biohybrid Systems. *Acc.Chem.Res.* **2017**, *50*, 476-481.
44. Chica, B.; Wu, C.-H.; Liu, Y.; Adams, M. W. W.; Lian, T.; Dyer, R. B., Balancing Electron Transfer Rate and Driving Force for Efficient Photocatalytic Hydrogen Production in Cdse/Cds Nanorod–[Nife] Hydrogenase Assemblies. *Energy Environ. Sci.* **2017**, *10*, 2245-2255.
45. He, C.; Nguyen, T. D.; Edme, K.; Olvera de la Cruz, M.; Weiss, E. A., Noncovalent Control of the Electrostatic Potential of Quantum Dots through the Formation of Interfacial Ion Pairs. *J. Am. Chem. Soc.* **2017**, *139*, 10126-10132.
46. Kodaimati, M. S.; Lian, S.; Schatz, G. C.; Weiss, E. A., Energy Transfer-Enhanced Photocatalytic Reduction of Protons within Quantum Dot Light-Harvesting–Catalyst Assemblies. *PNAS* **2018**, 8290-8295.
47. Wu, M.; Mukherjee, P.; Lamont, D. N.; Waldeck, D. H., Electron Transfer and Fluorescence Quenching of Nanoparticle Assemblies. *J. Phys. Chem. C* **2010**, *114*, 5751-5759.
48. Liu, R.; Bloom, B. P.; Waldeck, D. H.; Zhang, P.; Beratan, D. N., Controlling the Electron-Transfer Kinetics of Quantum-Dot Assemblies. *J. Phys. Chem. C* **2017**, *121*, 14401-14412.
49. Chen, J.; Wu, K.; Rudshteyn, B.; Jia, Y.; Ding, W.; Xie, Z.-X.; Batista, V. S.; Lian, T., Ultrafast Photoinduced Interfacial Proton Coupled Electron Transfer from Cdse Quantum Dots to 4,4′-Bipyridine. *J. Am. Chem. Soc.* **2016**, *138*, 884-892.
50. Wu, K.; Zhu, H.; Lian, T., Ultrafast Exciton Dynamics and Light-Driven H2 Evolution in Colloidal Semiconductor Nanorods and Pt-Tipped Nanorods. *Acc.Chem.Res.* **2015**, *48*, 851-859.
51. Zhu, H.; Lian, T., Enhanced Multiple Exciton Dissociation from Cdse Quantum Rods: The Effect of Nanocrystal Shape. *J. Am. Chem. Soc.* **2012**, *134*, 11289-11297.
52. Chan, W.-L.; Ligges, M.; Jailaubekov, A.; Kaake, L.; Miaja-Avila, L.; Zhu, X. Y., Observing the Multiexciton State in Singlet Fission and Ensuing Ultrafast Multielectron Transfer. *Science* **2011**, *334*, 1541-1545.
53. Zhu, H.; Song, N.; Rodríguez-Córdoba, W.; Lian, T., Wave Function Engineering for Efficient Extraction of up to Nineteen Electrons from One Cdse/Cds Quasi-Type Ii Quantum Dot. *J. Am. Chem. Soc.* **2012**, *134*, 4250-4257.
54. Nakibli, Y.; Mazal, Y.; Dubi, Y.; Wachtler, M.; Amirav, L., Size Matters: Cocatalyst Size Effect on Charge Transfer and Photocatalytic Activity. *Nano Lett.* **2018**, *18*, 357-364.
55. Wang, J.; Ding, T.; Wu, K., Coulomb Barrier for Sequential Two-Electron Transfer in a Nanoengineered Photocatalyst. *J. Am. Chem. Soc.* **2020**, *142*, 13934-13940.
56. Yan, C., et al., Uncovering the Role of Hole Traps in Promoting Hole Transfer from Multiexcitonic Quantum Dots to Molecular Acceptors. *ACS Nano* **2021**, *15*, 2281-2291.
57. Zhao, F.; Li, Q.; Han, K.; Lian, T., Mechanism of Efficient Viologen Radical Generation by Ultrafast Electron Transfer from Cds Quantum Dots. *J. Phys. Chem. C* **2018**, *122*, 17136-17142.
58. Li, Q.; Lian, T., Exciton Dissociation Dynamics and Light-Driven H2 Generation in Colloidal 2d Cadmium Chalcogenide Nanoplatelet Heterostructures. *Nano Research* **2018**, *11*, 3031-3049.
59. Wang, J.; Ding, T.; Wu, K., Charge Transfer from N-Doped Nanocrystals: Mimicking Intermediate Events in Multielectron Photocatalysis. *J. Am. Chem. Soc.* **2018**, *140*, 7791-7794.
60. Wang, J.; Ding, T.; Wu, K., Electron Transfer into Electron-Accumulated Nanocrystals: Mimicking Intermediate Events in Multielectron Photocatalysis Ii. *J. Am. Chem. Soc.* **2018**, 10117−10120.
61. Kim, D.; Lee, Y. K.; Lee, D.; Kim, W. D.; Bae, W. K.; Lee, D. C., Colloidal Dual-Diameter and Core-Position-Controlled Core/Shell Cadmium Chalcogenide Nanorods. *ACS Nano* **2017**, *11*, 12461-12472.

62. Schlicke, H.; Ghosh, D.; Fong, L. K.; Xin, H. L.; Zheng, H.; Alivisatos, A. P., Selective Placement of Faceted Metal Tips on Semiconductor Nanorods. *Angew. Chem. Int. Ed.* **2013**, *52*, 980-982.
63. Shabaev, A.; Efros, A. L., 1d Exciton Spectroscopy of Semiconductor Nanorods. *Nano Lett.* **2004**, *4*, 1821-1825.
64. Efros, A. L.; Rosen, M., The Electronic Structure of Semiconductor Nanocrystals. *Annu. Rev. Mater. Sci.* **2000**, *30*, 475-521.
65. Henglein, A.; Ershov, B. G.; Malow, M., Absorption Spectrum and Some Chemical Reactions of Colloidal Platinum in Aqueous Solution. *J. Phys. Chem.* **1995**, *99*, 14129-14136.
66. Wu, K.; Rodriguez-Cordoba, W.; Lian, T., Exciton Localization and Dissociation Dynamics in Cds and Cds-Pt Quantum Confined Nanorods: Effect of Nonuniform Rod Diameters. *J. Phys. Chem. B* **2014**, *118*, 14062-9.
67. Cline, R. P.; Utterback, J. K.; Strong, S. E.; Dukovic, G.; Eaves, J. D., On the Nature of Trapped-Hole States in Cds Nanocrystals and the Mechanism of Their Diffusion. *J. Phys. Chem. Lett.* **2018**, *9*, 3532-3537.
68. Utterback, J. K.; Grennell, A. N.; Wilker, M. B.; Pearce, O. M.; Eaves, J. D.; Dukovic, G., Observation of Trapped-Hole Diffusion on the Surfaces of Cds Nanorods. *Nat. Chem.* **2016**, *8*, 1061-1066.
69. Labrador, T.; Dukovic, G., Simultaneous Determination of Spectral Signatures and Decay Kinetics of Excited State Species in Semiconductor Nanocrystals Probed by Transient Absorption Spectroscopy. *J. Phys. Chem. C* **2020**, *124*, 8439-8447.
70. Wu, K.; Lim, J.; Klimov, V. I., Superposition Principle in Auger Recombination of Charged and Neutral Multicarrier States in Semiconductor Quantum Dots. *ACS Nano* **2017**, *11*, 8437-8447.
71. Li, Q.; Lian, T., Area-and Thickness-Dependent Biexciton Auger Recombination in Colloidal Cdse Nanoplatelets: Breaking the "Universal Volume Scaling Law". *Nano Lett.* **2017**, *17*, 3152-3158.
72. Zhu, H.; Lian, T., Enhanced Multiple Exciton Dissociation from Cdse Quantum Rods: The Effect of Nanocrystal Shape. *J. Am. Chem. Soc.* **2012**, *134*, 11289-97.
73. Htoon, H.; Hollingsworth, J. A.; Dickerson, R.; Klimov, V. I., Effect of Zero- to One-Dimensional Transformation on Multiparticle Auger Recombination in Semiconductor Quantum Rods. *Phys Rev Lett* **2003**, *91*, 227401.
74. Klimov, V. I.; Mikhailovsky, A. A.; McBranch, D. W.; Leatherdale, C. A.; Bawendi, M. G., Quantization of Multiparticle Auger Rates in Semiconductor Quantum Dots. *Science* **2000**, *287*, 1011-1013.
75. Wu, K.; Chen, Z.; Lv, H.; Zhu, H.; Hill, C. L.; Lian, T., Hole Removal Rate Limits Photodriven H2 Generation Efficiency in Cds-Pt and Cdse/Cds-Pt Semiconductor Nanorod-Metal Tip Heterostructures. *J. Am. Chem. Soc.* **2014**, *136*, 7708-7716.
76. Htoon, H.; Hollingsworth, J. A.; Dickerson, R.; Klimov, V. I., Effect of Zero- to One-Dimensional Transformation on Multiparticle Auger Recombination in Semiconductor Quantum Rods. *Phys. Rev. Lett.* **2003**, *91*, 227401.
77. Gong, C.; Colombo, L.; Wallace, R. M.; Cho, K., The Unusual Mechanism of Partial Fermi Level Pinning at Metal-Mos2 Interfaces. *Nano Lett* **2014**, *14*, 1714-20.

Appendix 1

Spectral fit of Abs of CdS NRs

The Absorption of CdS within energy window 2.5 eV-3.5 eV is fitted with 4 Gaussian peaks, shown as eq. A5.1.

$$Abs\ (ground\ state) = \sum_1^4 \frac{A_i}{\sqrt{2\pi}\sigma_i} e^{-\frac{(E-E_i)^2}{2\sigma_i^2}} \qquad (A5.1)$$

A_i is the peak intensity. E_i is the center of the peak. σ_i is the width of the peak. The fitting results are shown in Figure A.5.1 and Table A.5.1.

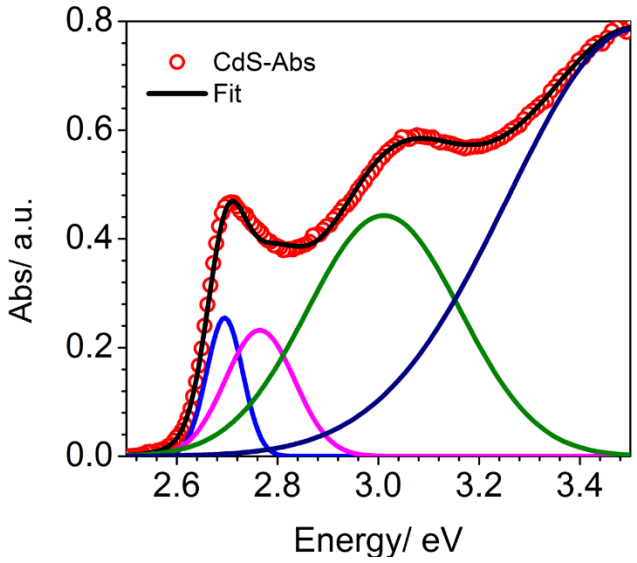

Figure A.5.1. Fit of the UV-vis absorption spectrum of CdS NRs to the sum of four Gaussian peaks according to eq. A.5.1. Fitting parameters can be found in Table A.5.1.

Table A.5.1. Fitting parameters of CdS UV-Vis absorption shown in Figure A.5.1.

Peak i	1	2	3	4
E_i /eV	2.69±0.00	2.77±0.00	3.04±0.00	3.50±0.01
σ_i/meV	36.1±0.1	68.7±3.1	151.7±5.9	254.0±18.5

$A_i \times 10^{-3}$	23.8±1.9	40.0±3.7	168.5±16.5	500.1±39.5

Appendix 2

Estimation of the exciton number in CdS.

Estimation of the 1Σ exciton number. Shown in Figure A.5.2A and A5.2B are the TA spectra under different fluences at 0.5 ps and 50 ns, respectively. The shape of TA spectra at 0.5 ps depends on the excitation fluence, indicate fluence dependence of multi-exciton features. The shape of TA spectra at 50 ns are independent of excitation fluence, which can be shown by the comparison of normalized TA spectra at 50 ns (Figure A.5.2C). Thus, this result suggests that at 50 ns, all the multiple exciton states have decayed and only the single exciton states exist in the NR. Figure A.5.3 compares the excitation fluence dependences of the signal amplitudes of 1Σ exciton bleach at 0.5 ps at 50 ns and PA signal at 1 ps. The 1Σ exciton bleach amplitude at 0.5 ps increases linearly with fluence at low excitation power, from 1.4 mW/cm^2 up to 8.4 mW/cm^2, corresponding to <N>~0.2 to <N>~1 .The signal saturates at higher fluence to a value close to the optical density of the ground state absorption shown in Figure 5.2C. It suggests that at the saturation fluence the 1Σ exciton transition is completed bleached and all 1Σ exciton states are fully occupied. The 1Σ exciton bleach signal amplitudes at 50 ns also saturates to a value ~ 40 mOD, indicating all rods contains a single exciton at this delay. The PA signal amplitude increases linearly with the excitation fluence as indicated by the black linear fit shown in Figure A.5.3A. Under 1.4 mW/cm^2 excitation fluence (single exciton condition), the ratio of 1Σ bleach amplitudes at 0.5 ps and 50 ns, S(1Σ, t=0.5ps)/S(1Σ,t=50ns), is ~2, suggesting that the 50% of rods with 1 exciton at t=0.5ps have

decayed into 0 exciton at t=50ns. At the highest excitation fluence, when all NRs are excited, the saturated value of S(1Σ,t=50ns) =40 mOD. Thus, it can be estimated that S(1Σ) ~80 mOD if every NR has one 1Σ exciton. Thus, the number of initial 1Σ exciton under various fluences can be calculated as S(1Σ, t=0.5ps)/80mOD. For example, under 1.4 mW/cm^2, S(1Σ, t=0.5ps)= -17 mOD, corresponding to <N>~0.2. As shown in Figure A.5.3A, this initial 1Σ exciton saturates at opposite value of O.D at the highest excitation fluence, suggesting that each nanorod can accommodate at most around 6 1Σ excitons.

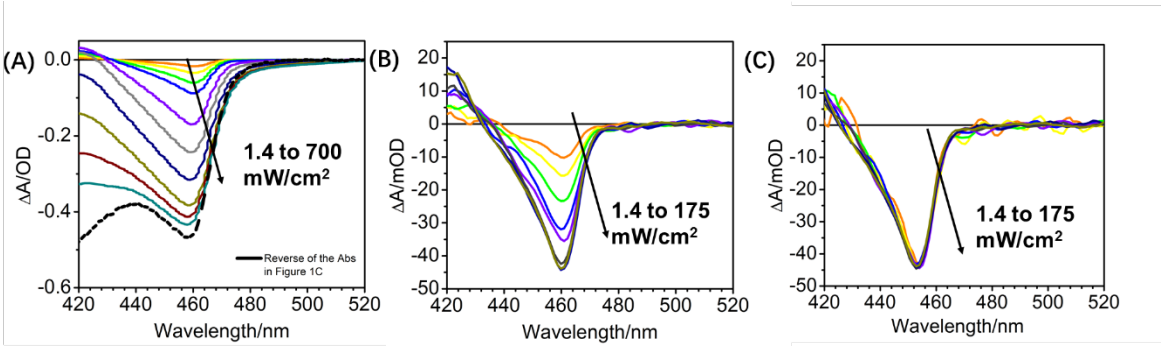

Figure A.5.2. Comparison of TA spectra at different fluences. (A) Comparison of the TA spectra of CdS NRs at t=0.5 ps measured with excitation fluences from 1.4 mW/cm^2 to 700 mW/cm^2 (colored solid lines). Also shown for comparison is the absorption spectrum of the NR (black dashed line) that has inverted for better comparison with exciton bleach amplitude. (B) Comparison of the TA spectra of CdS NRs at t=50 ns measured with excitation fluences from 1.4 mW/cm^2 to 700 mW/cm^2. Indicated by the highest three fluences, the bleach saturates at ~40 mOD indicating single exciton per nanorod.(C) Normalized comparison of TA spectra of (B), indicating that only the single exciton state remains at 50 ns regardless of excitation fluence.

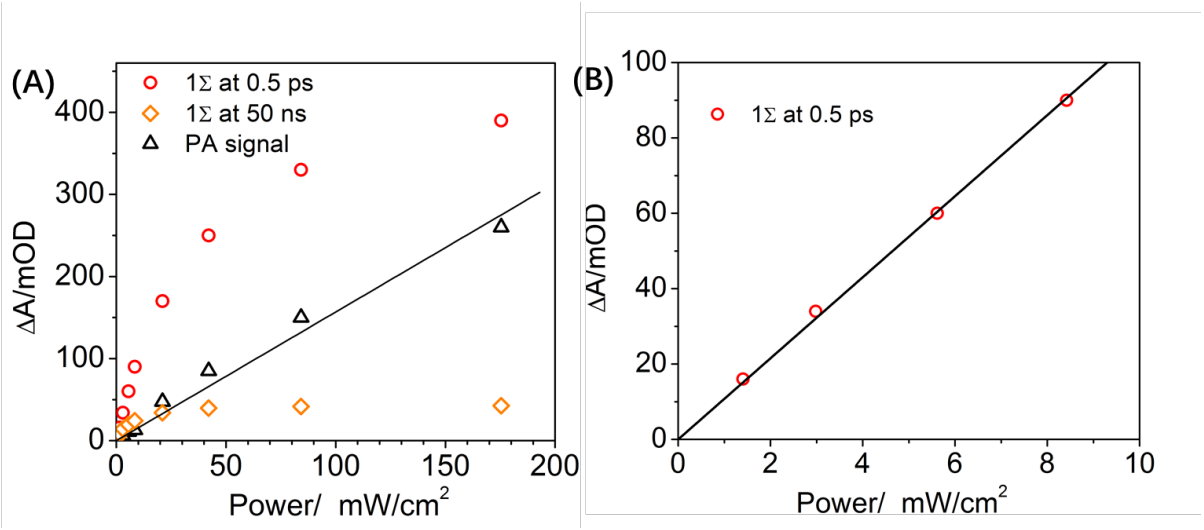

Figure A.5.3. (A) Excitation fluence dependences of amplitudes of 1Σ exciton bleach signal at 0.5 ps (1Σ at 0.5 ps, red open circles) and at 50 ns (1Σ at 50 ns, orange open diamonds) and PA signal of trapped holes at 1 ps (black open triangles). (B) Zoom-in of 1Σ at 0.5 ps at low fluences. The signal amplitudes increases linearly with fluences.

Estimation of the total exciton number. The total exciton number increases linearly with fluences, as indicated by the PA signal shown in Figure A.5.3A. At pump fluences from 1.4 mW/cm^2 to 8.4 mW/cm^2, the 1Σ state is not saturated and there is negligible higher energy excitons. The number of 1Σ excitons equals the total exciton number. The slope of the linear fit (1.89±0.02 mOD /(mW/cm^2), shown in Figure A.5.3B) of the 1Σ exciton number *vs* fluence represents the total number of excitons generated per unit fluence. Exciton number under higher fluences can be estimated by using this slope times photon fluence/80mOD. Our estimation of the exciton numbers in higher powers may contain ±~25% error considering the error in extrapolation using this slope.

Appendix 3

Spectral Fit of TA results of CdS NRs.

The TA spectrum of the CdS can be fitted as the absorbance difference between the excited state and ground state, as shown in eq. A.5.2.1 and A.5.2.2. In the excited state, the peak center is shifted by X_i due to the biexciton interaction.

$$Abs\ (excited\ state) = \sum_1^4 C_i \frac{A_i}{\sqrt{2\pi}\sigma_i} e^{-\frac{(E-E_i+X_i)^2}{2\sigma_i^2}} \quad \text{(A.5.2.1)}$$

$$\Delta A = [Abs\ (excited\ state) - Abs\ (ground\ state)] * < 1\Sigma N > \quad \text{(A.5.2.2)}$$

E_i, σ_i and A_i are same as the fitting results shown in Table A.5.1.C_i is the modified transition possibility caused by state filling of one electron the band edge (BE).[1] For i=1,2, C_i=5/6, reflecting that one electron reduces the band edge exciton transition strength by 1/6 because of the maximum occupancy of 6 electrons at the conduction band edge. For i=3,4, C_i=1, indicating the lack of state filling signals at higher exciton transitions under single exciton conditions. X_i is the biexciton energy. < 1Σ N> is average 1Σ exciton number, equals to 0.2 for this excitation fluence, which is the same fluence shown in Figure 5.3A. The fitting results of <N>~0.2 are shown in Figure A.5.4 and Table A.5.2.

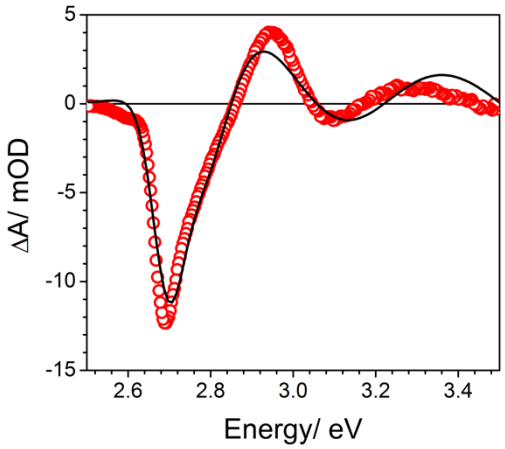

Figure A.5.4. Fit of CdS TA spectrum at 4.9 ns with average exciton number of 0.2.

Table A.5.2. The fitting parameters of CdS TA.

Peak i	1	2	3	4
X_i /meV	0.0±0.1	1.4±0.2	10.1±0.1	8.3±0.1

Appendix 4

Multiexciton dynamics in CdS

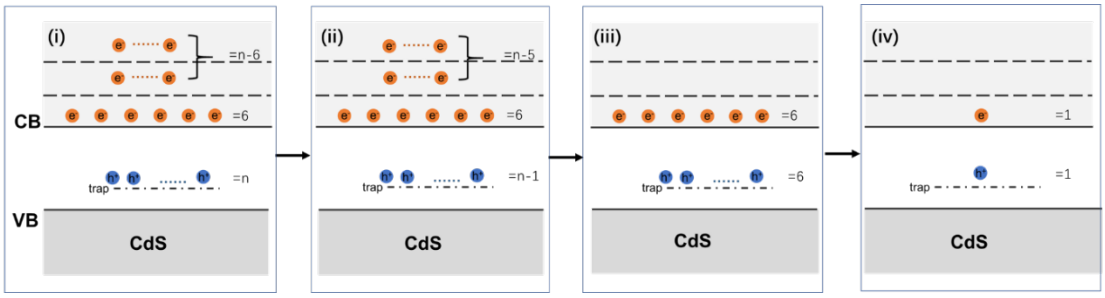

Figure A.5.5. Scheme for multiexciton decay in CdS. (i) n exciton states with 6 band edge electrons, and n-6 electrons above the band edge. (ii) Cascade decay of excitons states, from n exciton state to n-1 exciton state. (iii) 6 exciton state where electrons occupy the band edge levels.

(iv) The 1Σ excitons recombine with time constant described by the scaling law described in the main text until reaching the single exciton state.

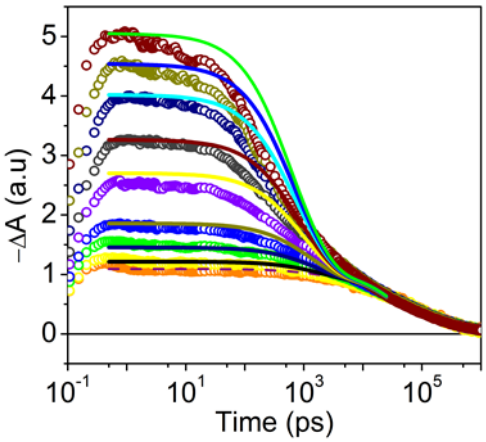

Figure A.5.6. Normalized comparison of 1Σ exciton bleach kinetics at different exciton fluence (open symbols) and their fit according to the exciton-collision model (solid lines) .

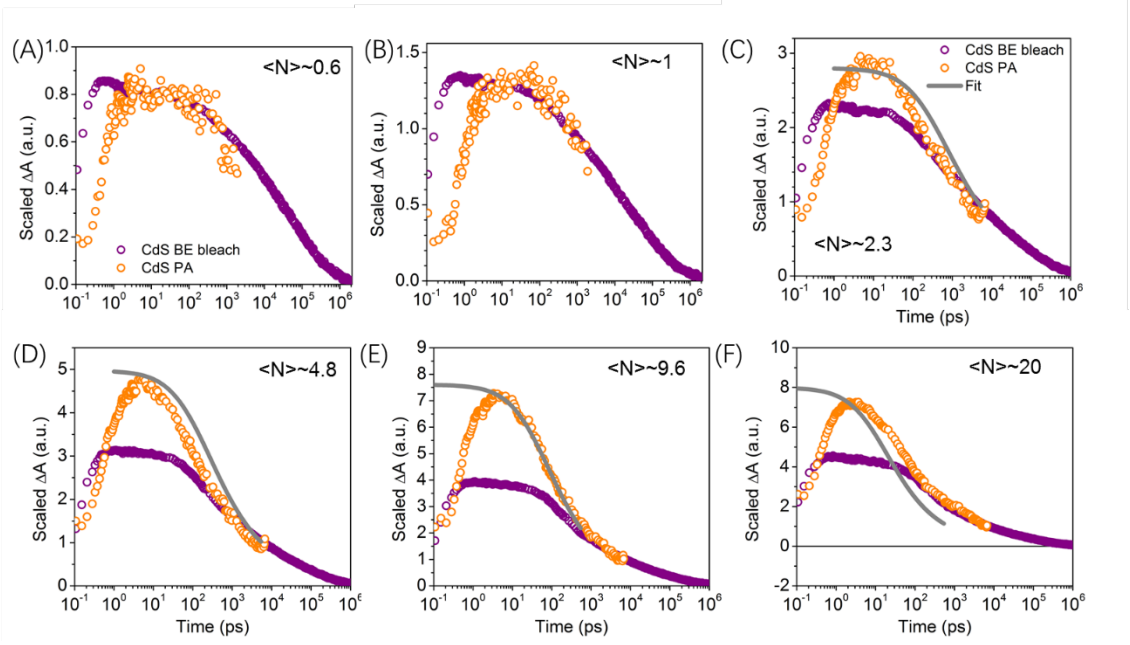

Figure A.5.7. The comparison of the CdS 1Σ exciton bleach recovery and PA signal (averaged from 550 - 600nm). The grey curve represents the fitting of the decay of exciton states above 1Σ band according to carrier -collision model described in the main text. The amplitudes of the PA

signal is modified into $\Delta A(t) = \sum_{n=1}^{n} nX_n(t)$ instead of eq. 5.2 to reflect linear increase of PA signal with the number of excitons.

Appendix 5

Auger recombination of 11-Mercaptoundecanoic acid (MUA) capped CdS NRs

The ligand exchange with 11-Mercaptoundecanoic acid (MUA) is carried out as previously described in our other papers.[2] Briefly, ~100 mg KOH was added to 10 mL water with 20 mg MUA. 5 mL of above solution was mixed with 2 mL CdS NR with OD=1 at 460 nm with 1 mm pathlength. The mixture was stirred until the NRs were fully exchanged into aqueous phase. The aqueous phase was then transferred into a 15 mL centrifuge tube and excess ethanol was added to precipitate the CdS NRs. The obtained precipitation is re-dissolved by 1 mL water and excess ethanol was added again to purify the NR. The final product is re-dispersed in DI water with pH=7. Under single exciton condition (we still assume the maximum band edge exciton is 6), the MUA capped CdS NR shows same spectral feature (Figure A.5.8A) as Figure 5.3A. However, the 1Σ bleach recovery shows a faster decay compared to the one capped with phosphonates (Figure A.5.8B). Stretched exponential fit gives a lifetime of 11.1±0.4 ns with β=0.34±0.01, corresponding to average lifetime 62.1±2.2 ns.

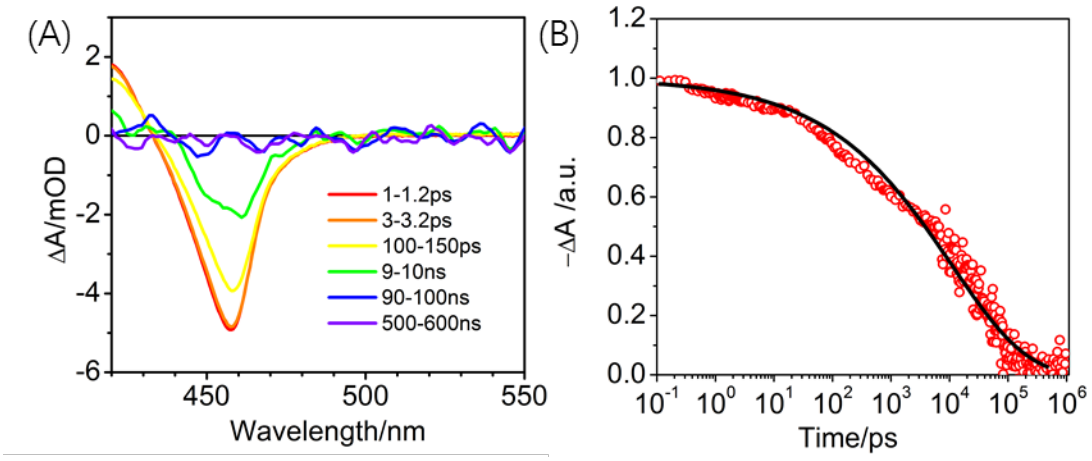

Figure A.5.8. (A) TA spectra of MUA capped CdS NRs with initial average number of excitons per NR of <N>~0.3 at selected delay times. (B). Normalized 1Σ exciton bleach recovery kinetics. Black line represents the stretched exponential fit.

Then, fluence dependent multiexciton recombination of MUA capped CdS was measured same as phosphonate capped CdS illustrated before. Figure A.5.9A shows the TA spectra with <N>~20, which is again similar to the one in Figure 5.4A. The fluence dependent kinetics are shown in Figure A.5.9B, normalized at 10^4-10^6 ps. Figure A.5.9C show the kinetics of <N>~0.3 and <N>~0.5. Biexciton kinetics obtained by subtracting the kinetics of <N>~0.3 from <N>~0.5 gives a lifetime of 165±26 ps. This value is consistent with biexciton lifetime reported in polyethylenimine-capped CdS dispersed in water before.[3] Similar to the analysis in the main text, we also test both Carrier-Collision and Exciton-Collision models. We notice increasing the fluence results in the appearance of a long lived component showing around 300 ps -10 ns when n>2. To get better fitting, we add another exponential component with lifetime ~2600 ps to eq. 5.2. This component is slower than the biexciton Auger recombination. It may come from trion interaction because thiol-ligands can serve as hole acceptor.

The fit according to Carrier-Collision model and Exciton-Collision model are shown in Figure A.5.9B and A.5.9D, respectively. Generally, the carrier-collision model gives a faster band edge decay. However, we are unable to differentiate which model explains the scaling law here, since they both fits the model well. The insensitivity of these two fits may come from the biexciton lifetime is about 165 ps, which gives Auger recombination lifetime of 6 exciton states of 3 ps and 11 ps in Carrier-Collision model and Exciton-Collision model. Because of the refilling of the band edge states from electron at high levels, band edge kinetics doesn't decay too much, leading to the fit is not sensitive to differentiate the difference between 3 ps and 11 ps.

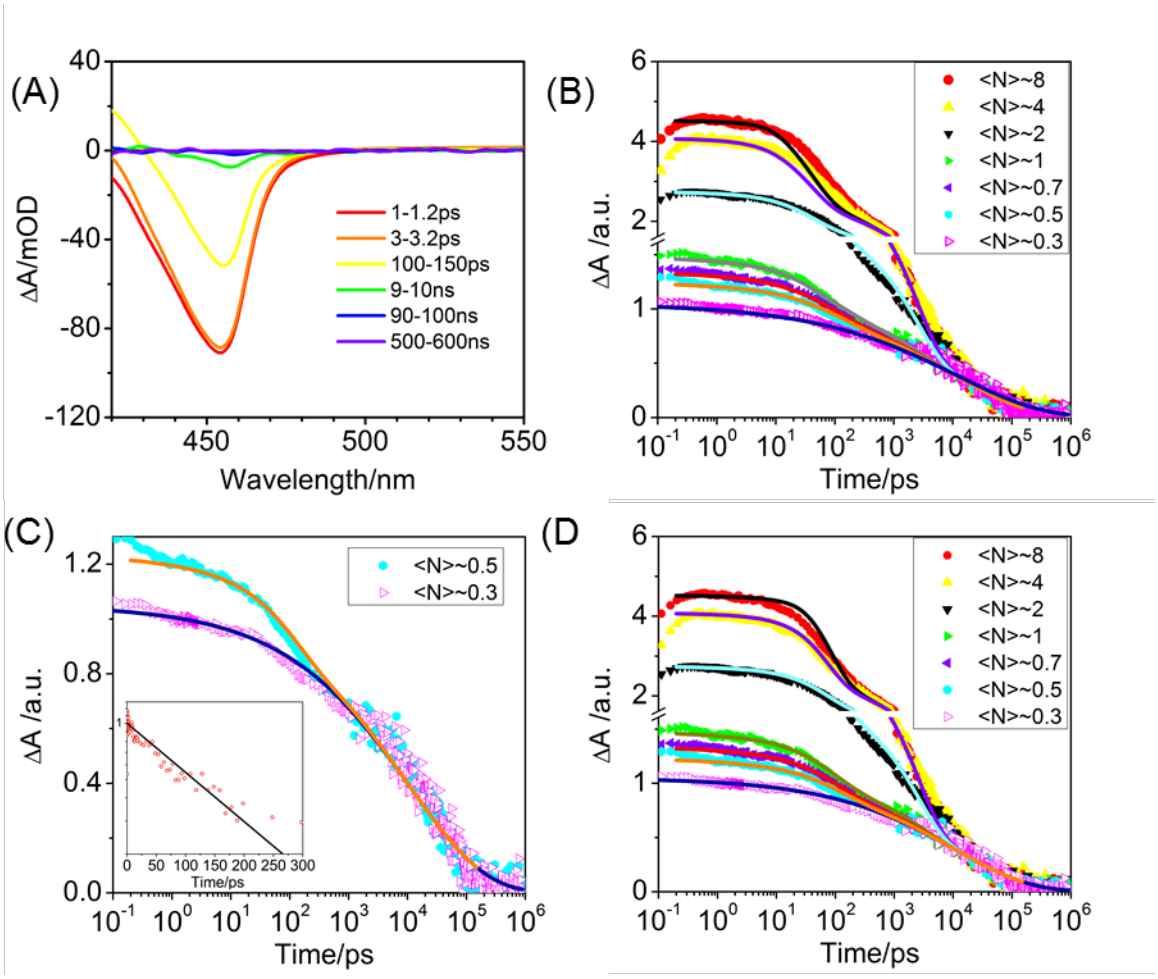

Figure A.5.9. (A) TA spectra of MUA capped CdS NRs with initial average number of excitons per NR of <N>~20 at selected delay times. (B). Comparison of normalized 1Σ exciton bleach recovery kinetics measured under various fluences <N> ~0.3 to 20. The solid lines indicates the fit to the Carrier-Collision model. (C) Kinetics of <N> of 0.3 and 0.5 in (B) are shown to obtain the biexciton decay kinetics in inset (red open circles) by subtracting the normalized 1Σ exciton bleach kinetics measured at <N>~0.3 from that of <N>~0.5. It fits to a single exponential decay function with a time constant of 165±26 ps (black line). (D) Normalized kinetics in (B) are shown again. The kinetics are fit to the Exciton-Collision model.

Appendix 6

Fit of the exciton bleach recovery and Charge Separated (CS) state kinetics

As shown in Figure 5.5A, after the completion of electron from the excited NRs to Pt, the TA spectra consists of the absorption of charge separated state, which shows a clear isosbestic point at 466 nm. Thus, the TA spectra at earlier delay time is a sum of the exciton bleach of the excited NR and the charge separated state. This kinetics at the 466 nm represents the pure contribution of exciton bleach recovery, which reflects the electron transfer kinetics from the NR to Pt. This kinetics can be fitted to a five exponential decay, according to eq. A.5.3.

$$\Delta A = \sum_{i=1}^{5} A_i \exp\left(-\frac{t}{\tau_i}\right) \qquad \text{(A.5.3)}$$

Table A.5.3. Fitting parameter of decay kinetics in <N>~0.3 CdS-Pt in eq. A.5.3

i	1	2	3	4	5
A_i/%	34.3±8.1	22.6±7.7	17.5±3.0	16.2±2.6	9.5±0.7
τ_i/ps	0.9±0.2	3.3±1.6	23.2±8.9	168.5±38.6	3297.2±344.4

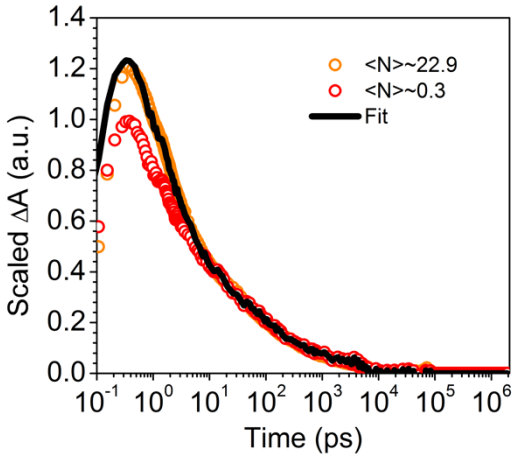

Figure A.5.10. The Fit of the fast decay component in comparison of <N>~0.3 and <N>~22.9. The additional fast decay can be fitted by a single exponential component with lifetime of 2.6 ps. This rate is faster than the Auger recombination of the 1Σ excitons. It is likely caused by multiple exciton induced spectral shift at early delay time.

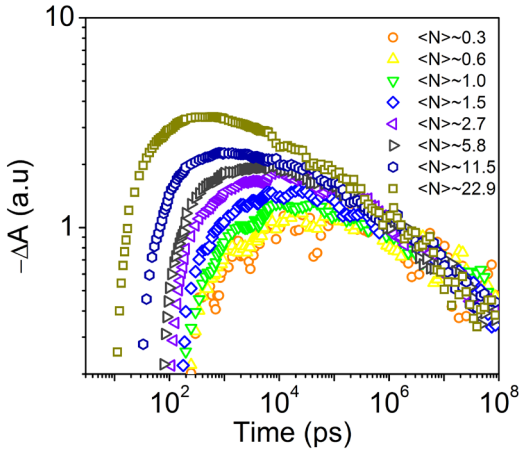

Figure A.5.11. The kinetics at 472nm with increasing <N> from 0.3 to 22.9.

The TA signal at other wavelength, especially 472 nm, is a sum of CdS exciton bleach and charge separated state. The kinetics containing growth and decay of charge separated state is obtained by using the kinetics at 472 nm subtracts the kinetics at 466 nm. The goal of this

calculation is to subtract the CdS signal contribution from the total signal at 472 nm. The remaining part is from charge separated state signal.

Considering the intrinsic decay of charge separated state, charge separated state kinetics can be represented by eq. A5.4.

$$\Delta A = \sum_{j=1}^{5} A_j \, exp\left(-\frac{t}{\tau_{CR,j}}\right) - C \sum_{i=1}^{5} A_i \, exp\left(-\frac{t}{\tau_i}\right)] \qquad \text{(A.5.4)}$$

$\tau_{CR,i}$ represents the charge separated state recombination lifetime. C is a scaling factor. The first term in A.5.4 represents the decay due to charge separated state recombination. The second term represents the growth of charge separated states due to the electron transfer. The results are shown in Figure A.5.10. As can be seen, up to <N>~2.7, we can fully subtract the CdS contribution at 472 nm, indicated by the consistency between the red dots and orange lines. The early fast decay before 3 ps is due to the exciton cooling to be band edge which was reported before.[1] The gray line represents the first term in eq. A.5.4 which only considers the intrinsic recombination. Under higher fluence, we are unable to subtract the CdS contribution perfectly at early times. This may be attributed to some spectral shift as shown in Figure A.5.8.

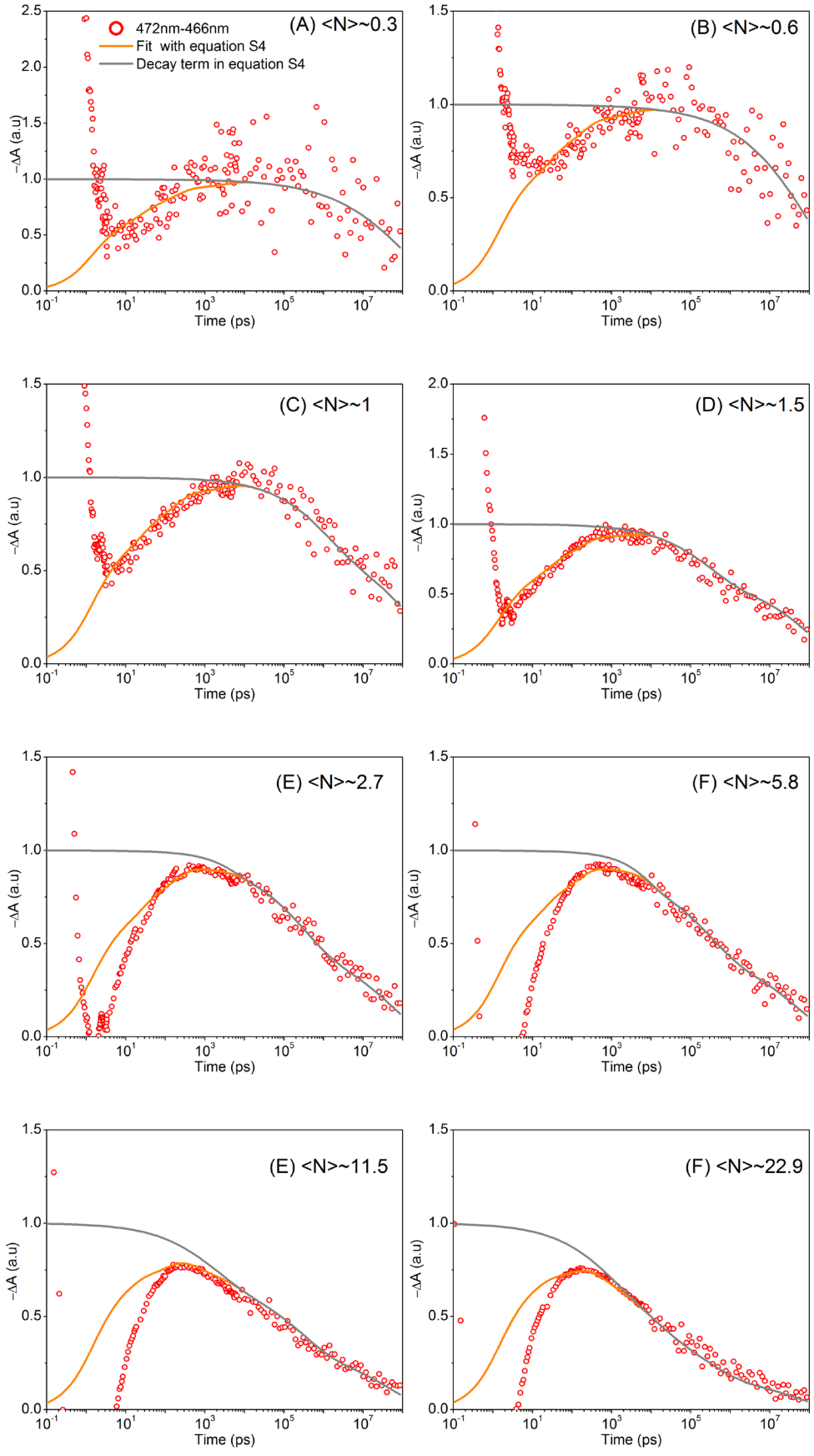
472nm-466nm
Fit with equation S4
Decay term in equation S4
(A) <N>~0.3
(B) <N>~0.6
(C) <N>~1
(D) <N>~1.5
(E) <N>~2.7
(F) <N>~5.8
(E) <N>~11.5
(F) <N>~22.9
−ΔA (a.u)
Time (ps)

Figure A.5.12. Charge separated state kinetics using 472nm kinetics subtract 466nm kinetics, shown as red open circles. The orange solid line represents the estimated Charge separated state kinetics considering the growth from electron transfer and its intrinsic recombination, as shown by eq. A.5.4. The gray line represents the recombination term in eq. A.5.4 only.

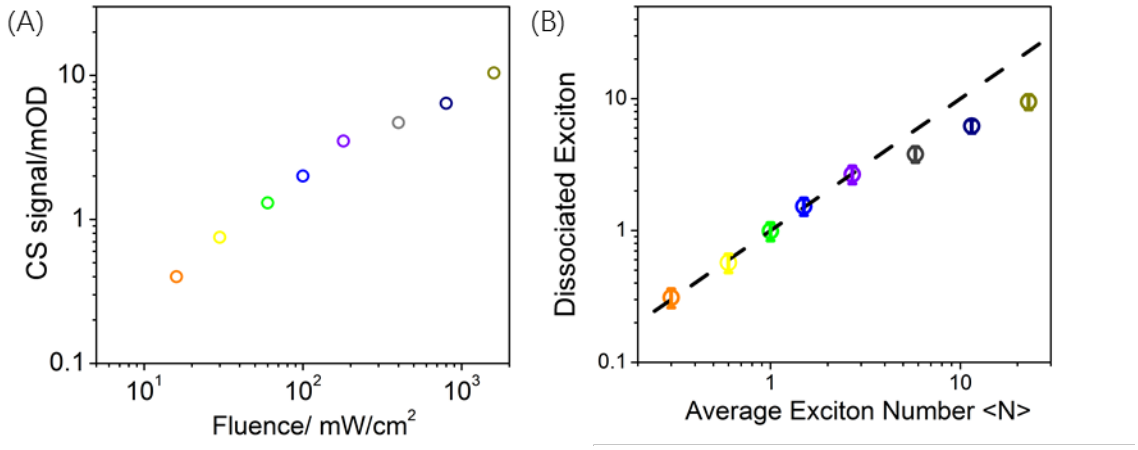

Figure A.5.13. (A) The charge separated signal amplitudes at 472nm versus pump fluence.(B) Estimate the dissociation exciton using signal amplitudes after subtracting CdS bleach as described above. After the subtraction, the signal amplitudes is about 10-20% larger under high fluences (N>3). The black line represents 100% dissociation efficiency. The efficiency calculated by dissociated exciton /average exciton number is shown in Figure 5.5D. Those observed efficiencies set the lower bound of dissociation efficiency due to the underestimate of the signal amplitudes.

Table A.5.4. Estimate of n-exciton state (X_n) dissociation efficiency into n-1 state

State	X_n	……	X_3	X_2	X_1
τ_n^A/ps	1970/[n^2(n-1)/4]		438	1970	200000

η_n	$\sum A_i \frac{K_i^{CS}}{K_i^{CS} + K_n^A}$		85.6%	91.9%	98.9%

The n-exciton state can either undergo fast Auger recombination with first order rate constant K_n^A (Eq. 5.1) or electron transfer with rate constant K_i^{CS}. Auger recombination constant has been determined from fitting of multiple exciton bleach recovery data shown in Figure 5.4D and are listed in Table A.5.4. The electron transfer rate constants are determined from the five-exponential fit to Figure 5.3B, and the amplitude and rate constants (A_i, K_i^{CS}) are listed in Table A.5.3, which is independent of the excitation fluence. Thus, the exciton dissociation efficiency for n-exciton state can be calculated using $\eta_n = \sum A_i \frac{K_i^{CS}}{K_i^{CS}+K_n^A}$ and are listed in Table A.5.4 and plot in Figure A.5.14.

We denote all possible states in CdS-Pt by (n,j,k), where n is the number of electrons in CdS, j (j>=n) holes in CdS, and k electrons in Pt. The biexciton state in CdS-Pt with 2 electrons and 2 holes in CdS and 0 electrons in Pt can be denoted as (2,2,0). We first start with (2,2,0) to illustrate possible decay channels, as shown in Figure A.5.15(A). It can recombination into (1,1,0) with a probability of 1-η_2 or it can dissociate into (1,2,1) with possibility η_2. (1,1,0) state can recombination into ground state with a probability of 1-η_1 or dissociate into (0,1,1) with a probability of η_1. The (1,2,1) state is a positive trion state in the CdS (one electron and two holes), which is assumed to have a lifetime similar to the exciton intrinsic lifetime because the holes are trapped and positive trion Auger recombination pathway can be neglected. Thus, (1,2,1) can transfer electron to form (0,2,2) state with a probability η_1 or (0,1,1) state with a probability of 1-η_1. The total probability of electron transfer into Pt is $\eta_1 + \eta_2$ by summing all pathways, as shown in Figure A.5.15(A).

More generally, starting from state (n,j,k), when n is larger than 1, the multiexciton Auger recombination is always faster than trion Auger recombination, thus trion interaction can be neglected. Thus, the electron transfer efficiency is same as (n,n,0), as shown in (B). We denote the final number of electrons transferred to Pt from state (n,j,k) as $N_{n,k}$. It can be shown that $N_{n,k+1}= N_{n,k}+1$, because j doesn't influence $N_{n,k}$ when the positive trion interaction is neglected.

Thus, as shown in Figure A.5.2(B), one can prove that $N_{n,k}=(1-\eta_n)N_{n-1,k}+\eta_n N_{n-1,k+1}=(1-\eta_n)N_{n-1,k}+ \eta_n (N_{n-1,k}+1)= N_{n-1,k}+ \eta_n$. With $N_{2,0}= \eta_1 + \eta_2$, and $N_{1,0}= \eta_1$, it can be shown that $N_{n,0}=\sum_{i=0,1,\ldots,n} \eta_i$. Consequently, the total dissociation efficiency from n exciton state is $\frac{\sum_{i=0,1,\ldots,n} \eta_i}{n}$. The values of η_i are listed in Table A.5.4. A plot of the dissociation efficiency of n-exciton state is shown in Figure A.5.14.

The average exciton dissociation efficiency at an excitation fluence <N> can be calculated by considering the Poisson distribution of initial exciton numbers per nanorod, and is plotted in Figure 5.5D as gray line.

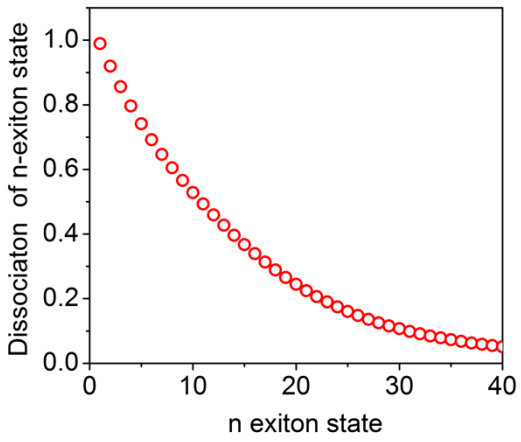

Figure A.5.14. The dissociation efficiency of n-exciton state.

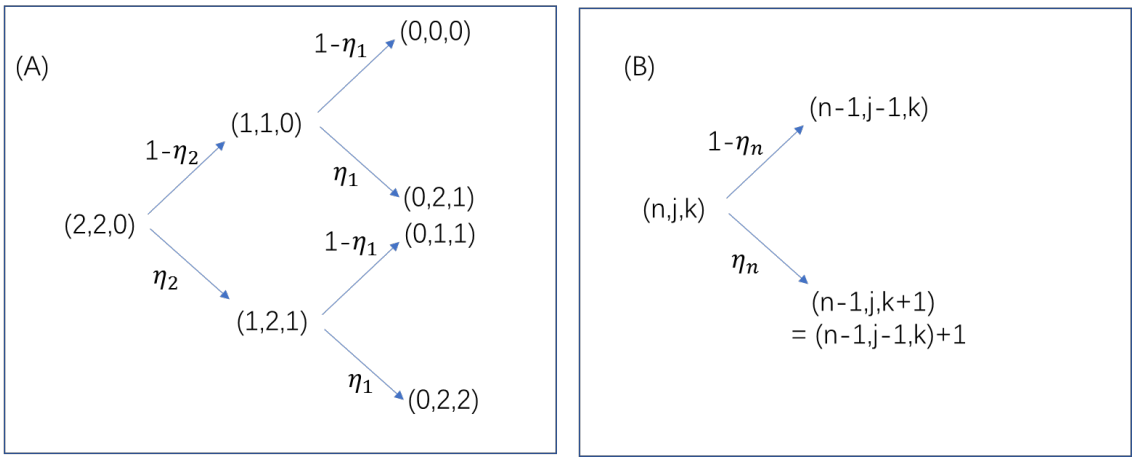

Figure A.5.15. The decay pathways of exciton state. (A) Taking 2- exciton state as an example. (B) More generally, with n electrons, j holes in CdS, k electrons in Pt.

Appendix 7

Fit of the TA spectrum of CdS-Pt NRs

After the completion of electron transfer from the CdS NR to Pt (~ 1 ns, Figure A.5.8), the TA spectra of CdS-Pt are dominated by the charge separated state, which can be fitted as the difference between the shifted absorption of charge separated state (CS) and the ground state (GS), showing the characteristic derivative shape of the Stark effect spectra. The absorption spectrum of ground state has been fit above, as shown in Figure A.5.1 and the fitting parameters are listed in Table A.5.1. The absorption of the charge separated state can be described by.

$$Abs\ (CS) = \sum_1^4 \frac{A_i}{\sqrt{2\pi}\sigma'_i} e^{-\frac{(E-E_i+SE_i)^2}{2\sigma'^2_i}} \quad \text{(A.5.5.1)}$$

Where $SE_i\ and\ \sigma'_i$ are peak shift and peak width of CdS exciton bands in the charge separated state. A_i and E_i are the amplitude and peak position of these exciton bands in the ground state of CdS, as determined in Table A.5.1. Thus, the TA spectra are given by:

$$\Delta A = [Abs\ (CS) - Abs\ (GS)] * \frac{1}{6} * <\ Pt\ N\ > (t = 6.3ns) \quad \text{(A.5.5.2)}$$

$< \mathrm{Pt\ N} > (\mathrm{t} = 6.3\ \mathrm{ns})$ is the number of electrons in the Pt at 6.3 ns after the excitation. The 1/6 factor comes from that there are up to 6 electrons in the conduction band. <Pt N> =$\eta_{CS} * < 1\Sigma\ N >$, where <1ΣN> is average number of 1Σ excitons, and η_{CS} is the exciton dissociation efficiency at t=6.3ns. At low fluence, η_{CS}~ 100% gives a good fit to the TA spectra. Under high fluences, η_{CS} is used as a fitting parameter. As shown in Figure A.5.16, the TA spectra under all fluences can be well fit by this model, especially at the low energy side. The fitting parameters are listed in and Table A.5.5-6. The spectra of the charge separate state at different excitation fluences (with different number of separated excitons) can be fit with the same spectra shape, indicating the negligible spectral shift with increasing hole densities in the CdS NRs. Thus, the amplitude at 472nm, the lower energy peak of the charge separated signal, increases linearly with the population of charge separated states, and can be used to determine the number of dissociated excitons. The charge separated state amplitudes as a function of fluence is plotted in Figure A.5.11. Because at low fluence, the exciton dissociation efficiency is 100%, we can also determine the number of dissociated excitons from Figure A.5.11, which is shown in Figure A.5.13B.

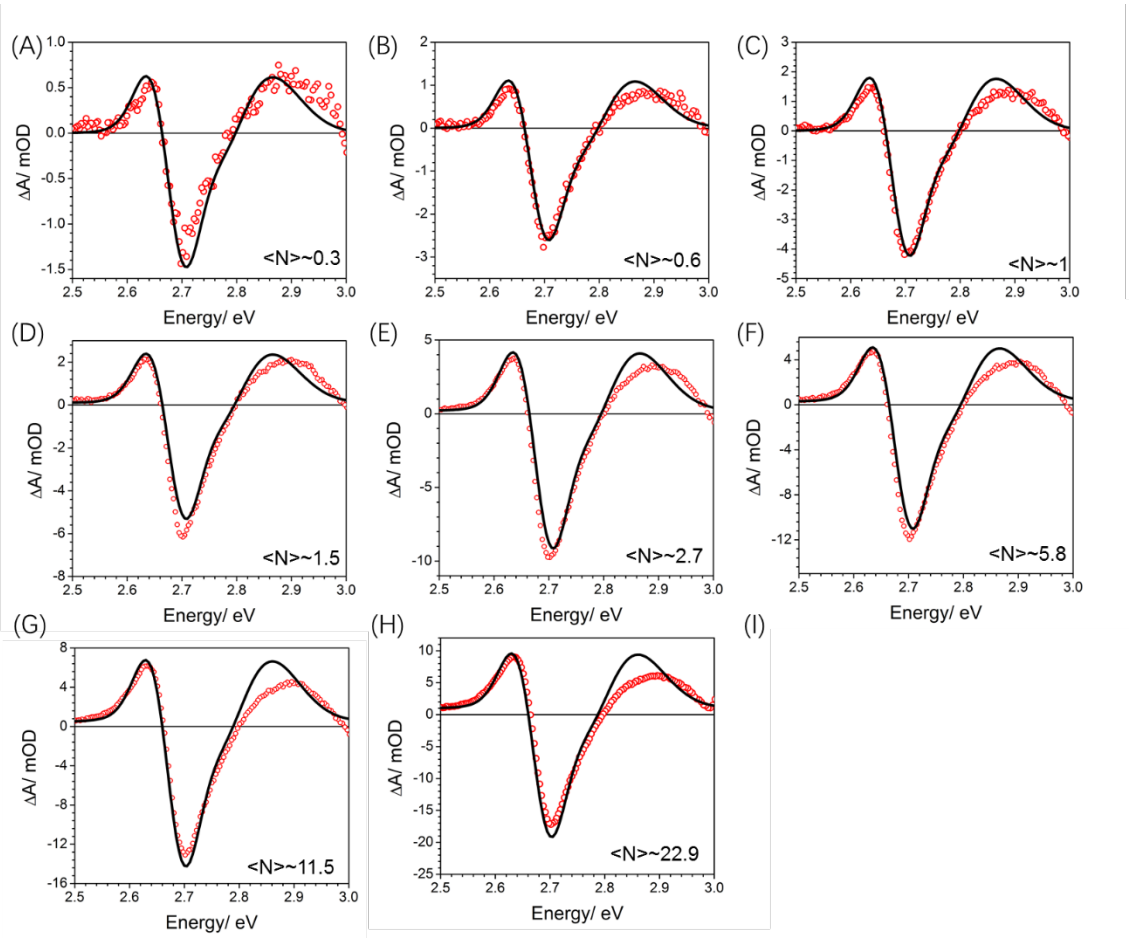

Figure A.5.16. Fit of CdS-Pt TA charge-separation spectrum under various fluence at 6.3 ns with eq. A.5.5.1-2.

Table A.5.5. Fitting parameters of charge separation spectrum of CdS-Pt in eq. A.5.5.1

i	1	2	3	4
SE_i/meV	-2	5	0	0
σ'_i/meV	38.5	72.0	151.7	254

Table A.5.6. < Pt N> for different fluences in eq.A.5.5.2

	<Pt N> (t=6.3ns)

Figure A.5.16 A	0.3
Figure A.5.16 B	0.53
Figure A.5.16 C	0.86
Figure A.5.16 D	1.1
Figure A.5.16 E	1.9
Figure A.5.16 F	2.3
Figure A.5.16 G	3
Figure A.5.16 H	4.1

Appendix 8

Fit of charge recombination in CdS-Pt

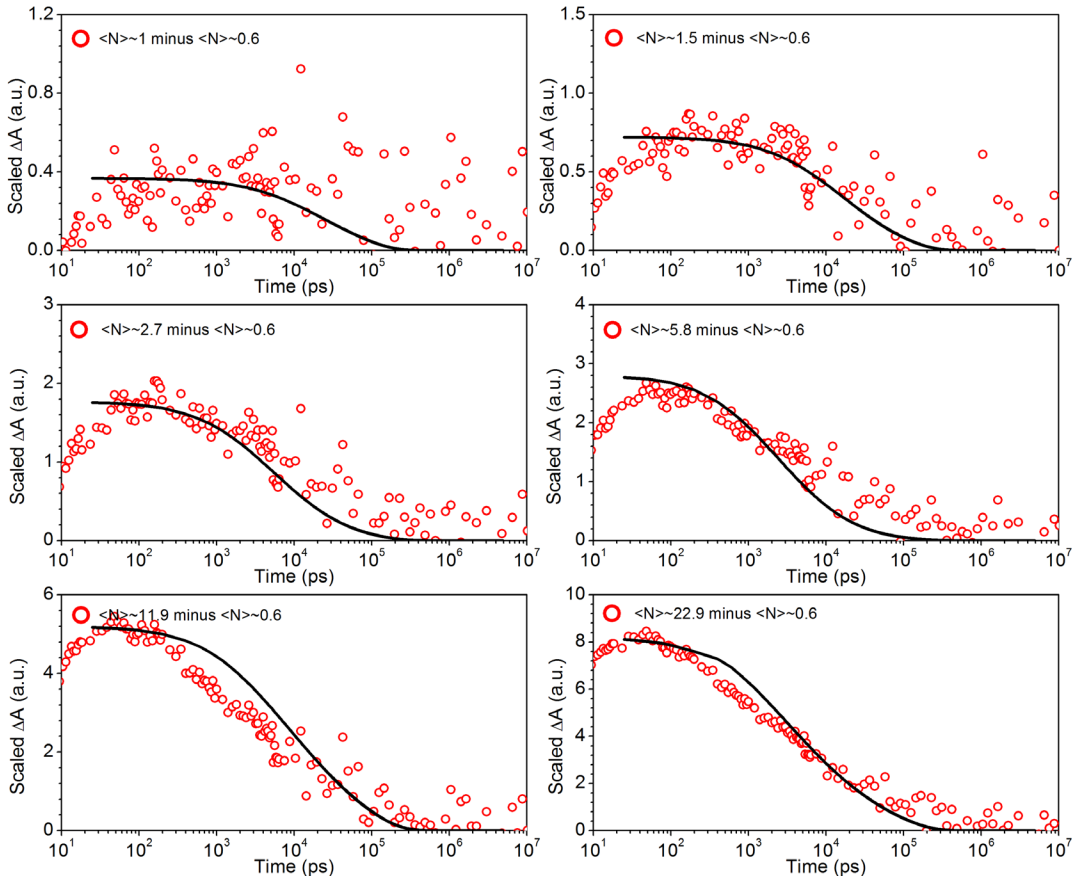

Figure A.5.17. Charge recombination kinetics in CdS-Pt. Measured CR kinetics at 472 nm (open symbols) at indicated excitation fluxes and their fit (solid line) to a bimolecular recombination model described by eq. A.5.6.1-6.3

Due to the non-exponential recombination in charge separated state, simulating the kinetics is difficult. To avoid dealing with this non-exponential feature, the single charge separated state recombination is subtracted. For example, in Figure A above, the red dots represent the kinetics obtained by using the kinetics with <N>~1 minus the <N>~0.6. Due to limited signal-to -noise ratio at lowest fluences, we have used fluence C (<N>~ 0.6) to represent the single exciton condition. This signal represents the decay from n charge separated state with n>=2.

The kinetics is fitted according to eqs. A.5.6.1-6.3.

$$\frac{d}{dt}\begin{bmatrix} X_n \\ X_{n-1} \\ \vdots \\ X_2 \\ X_1 \end{bmatrix}_{n\times 1} = \begin{bmatrix} k_n^A & & & & \\ k_n^A & -k_{n-1}^A & & & \\ & \ddots & \ddots & & \\ & & k_3^A & k_2^A & \\ & & & k_2^A & -k_1^A \end{bmatrix}_{n\times n} \begin{bmatrix} X_n \\ X_{n-1} \\ \vdots \\ X_2 \\ X_1 \end{bmatrix}_{n\times 1} \quad \text{(A.5.6.1)}$$

$$\frac{\tau_n^R}{\tau_2^R} = \frac{n-a}{2} \quad \text{(A.5.6.2)}$$

$$\Delta A = \sum(n-1)X_n \quad (n\,max \geq n \geq 2). \text{5.6.3)}$$

X_n is the population of charge separated state with n electrons in the Pt. The power a and τ_1^R representing the single e-h pair recombination lifetime in A.5.6.2 is the fitting parameter and the lifetime of higher charge separated states are determined by Eq. A.5.6.2. Note in A.5.6.3, the ΔA doesn't equal to $\sum nX_n$ due to subtraction of single charge separated state. For simplicity, the initial population of each state is assumed to follow Poisson distribution with average number of dissociation exciton shown in Figure 5.5C. For Figure A.5.17 A-D, n maximum=10 is used in the kinetics modelling, since there are negligible contributions of higher charge separated states. For E and F, n maximum=16 is used due to higher carrier density. The fits of the charge recombination kinetics with τ_2^R=90 ns and a=3.5 are shown as solid lines in Figure A.5.17, which qualitatively fits the data.

1. Wu, K.; Zhu, H.; Liu, Z.; Rodriguez-Cordoba, W.; Lian, T., Ultrafast charge separation and long-lived charge separated state in photocatalytic CdS-Pt nanorod heterostructures. *J. Am. Chem. Soc.* **2012,** *134* (25), 10337-10340.
2. Li, Q.; Zhao, F.; Qu, C.; Shang, Q.; Xu, Z.; Yu, L.; McBride, J. R.; Lian, T., 2D Morphology Enhances Light-driven H2 Generation Efficiency in CdS Nanoplatelet-Pt Heterostructures. *J. Am. Chem. Soc.* **2018**, 11726–11734.
3. Ben-Shahar, Y.; Philbin, J. P.; Scotognella, F.; Ganzer, L.; Cerullo, G.; Rabani, E.; Banin, U., Charge Carrier Dynamics in Photocatalytic Hybrid Semiconductor-Metal Nanorods: Crossover from Auger Recombination to Charge Transfer. *Nano Lett.* **2018,** *18* (8), 5211-5216.

Chapter 6. Plasmon-Induced Hot Electron Transfer in Metal-semiconductor Heterostructures

6.1 Introduction

Photoexcitation of plasmons in metal nanoparticles has been shown to drive chemical transformations in plasmonic hot carrier photocatalysts,[1-11] and generate photocurrents in plasmonic photo-detectors.[12-15] These processes can often be understood by the conventional plasmon-induced hot electron transfer (PHET) model, in which hot carriers are first generated in the metal by plasmon decay, and then undergo interfacial transfer to molecular or semiconductor acceptors.[16] The quantum efficiency of the PHET process is determined by two factors: 1) the initial populations of hot electrons (holes) with sufficient energy to be transferred to the acceptor and 2) the transfer efficiency of these hot electrons (holes) to the acceptor.[17-20] As shown in Figure 6.1, in small nanoparticles, in which radiative decay or scattering is weak, the plasmon decays mainly by creating electron-hole (e-h) pairs through the d-sp interband or sp-sp intraband transitions. The intraband pathway generates nearly uniform distribution of hot electrons and holes above and below the Fermi level, respectively. However, in bulk metals, this pathway cannot simultaneously satisfy both the energy and momentum conversation requirements, because of different energy-momentum dispersion relationships of an electron and a plasmon in a metal; and therefore, can only occur with the participation of phonons and/or surface scattering. Thus, for metals with the d-sp band transition near the plasmon energy, such as Au, the interband decay pathway may dominate because it can satisfy both the momentum and energy conservation requirements. Because of the location of the d-band (Figure 6.1A), this process generates hot holes

at the d band and electrons near the Fermi level with small excess energy.[17] For a metal/semiconductor junction (Figure 6.1B), the successful transfer of hot electrons across the interface requires that hot electrons have energy above the semiconductor conduction band (CB) edge and sufficient momentum to cross the interface,[21] as well as fast interfacial hot electron transfer (HET) rate to compete with ultrafast hot electron relaxation within the metal.[17, 22-24] Thus, for many plasmonic metals, such as Au, Ag, and Cu, both the small initial hot electron energy and the competition of interfacial transfer with ultrafast hot carrier relaxation limits the overall PHET efficiency. As a result, most reported quantum efficiencies of plasmonic hot carrier devices and processes are low, which may limit their potential applications.[12-14]

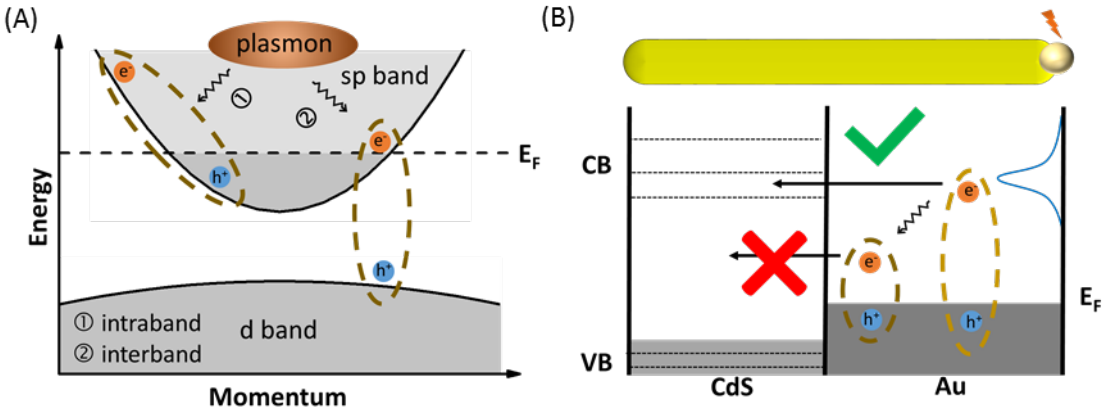

Figure 6.1. (A) Plasmon induced hot electron transfer at metal/semiconductor junction. Interband (d-sp) and intraband (sp-sp) decay pathways for plasmon in metals. (B) Sequential plasmon decay and hot carrier transfer at Au nanoparticle/CdS nanorod interface.

In recent years, intensive efforts have been devoted to developing approaches to improve the hot carrier generation and transfer efficiencies. [15, 17, 25-29] It has been reported that in strongly coupled metal/semiconductor nano-heterostructures, plasmons can decay through the plasmon induced

interfacial charge transfer transition (PICTT) pathway by directly exciting the interfacial charge transfer transition,[28] similar to the well-studied chemical interface damping mechanism.[30-33] This pathway can satisfy both momentum and energy conversation requirements and avoid competition with hot electron relaxation by directly exciting electrons to the CB of the semiconductor, making it a highly efficient approach for plasmon induced hot electron transfer. PHET efficiencies can also be improved through the choice of the plasmonic metals. For example, materials or alloys with appropriate bulk band structures can alter the initial distribution of hot electrons.[17, 18, 20, 34] Furthermore, theoretical studies have also shown that in small plasmonic nanoparticles, plasmon can decay by surface scattering, which enhances the contribution of intraband decay pathway and increases the probability of generating hot electrons,[17-19, 35] although these predictions have yet to be experimentally verified.

In this chapter, we report an experimental study to directly measure how the PHET efficiency at Au/CdS interface depends on the size of the Au nanoparticle. This study exploits Au tipped CdS nanorods (NRs) as a unique platform to allow direct transient absorption measurement of PHET efficiencies and systematic variation of the Au particle size without changing the CdS NR.[27] We show that with decreasing Au tip diameter from 5.5 to 1.6 nm, the PHET quantum efficiency (QE) increases from ~ 1% to ~18%. Analysis of size dependences of the PHET efficiency suggest that decreasing the particle size enhances the initial distribution of hot electrons generated by plasmon decay, reduces the barrier of hot electron transfer, and increases the rate of hot electron transfer. The combination of these factors leads to the large increase of PHET QEs at small particle sizes. Our finding demonstrates an important approach for enhancing the efficiencies of plasmonic hot carrier devices.

6.2. Results and Discussion

6.2.1 Absorption Spectra and TEM images of CdS-Au NRs

CdS-Au NR heterostructures with the same CdS rod (length and diameter) and six different Au tip sizes were synthesized following reported procedures with slight modifications, as described in the chapter 2.[27, 36, 37] From the TEM image of CdS NRs prior to the addition of the Au tip (Figure A.6.1), the length and diameter of CdS NRs are determined to be 35.3±3.5 nm and 4.1±0.7nm, respectively (inset of Figure A.6.1). The UV-Vis absorption spectrum of CdS NRs (Figure 6.2A) shows clear exciton bands with the lowest energy band at 2.67eV, consistent with previous reports of CdS NRs of a similar diameter.[27, 38] According to the TEM images of CdS-Au, these NRs mostly have one Au particle at one end of the CdS NR (Figure A.6.2 and Figure 6.2B), consistent with previously reported morphology,[36] and the diameters of the Au particles are 1.6±0.5, 1.7±0.5, 1.9±0.9, 3.3±1.3, 5.0±0.9, and 5.5±1.1 nm in these samples. These samples are referred to as CdSAux.xnm, where x.xnm is the average diameter of the Au tip. The HAADF-STEM image of CdSAu5.0nm sample (Figure 6.2C) shows a direct contact between the CdS and Au with atomic resolution, indicating a clean interface between these domains. The normalized comparison of the UV-Vis absorption spectra of six CdS-Au samples (Figure 6.2A) show both the Au surface plasmon resonance and the CdS exciton bands. In all samples, the CdS exciton band of the CdS-Au NRs are similar to the NRs prior to the addition of Au tip. With decreasing Au tip sizes, the plasmon intensity at ~2.36eV decreases and peak width broadens, which is consistent with published results,[39] and will be further analyzed below. These spectra have been normalized at ~ 2.9 eV to better illustrate how the relative contributions of Au plasmon band increase at larger Au particle sizes. The actual concentrations of CdS-Au NRs have been adjusted to ensure sufficient

absorption of Au plasmon band for reliable transient absorption spectroscopy measurement to be discussed below.

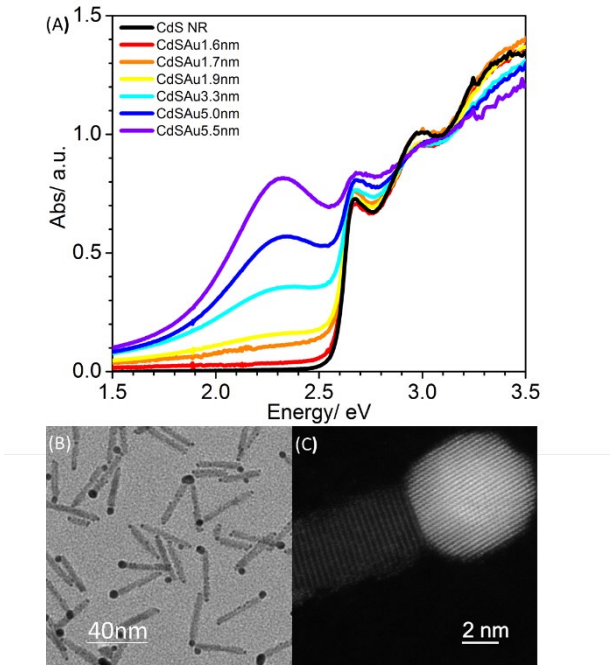

Figure 6.2. (A) UV-Vis absorption spectra of CdS-Au NRs with the same CdS NRs and different Au tip sizes. (B) TEM and (C) HAADF-STEM images of CdS-Au NRs with the Au diameter of 5.0±0.9 nm (CdSAu5.0nm).

6.2.2 Analysis of the plasmon width in UV-vis absorption of CdS-Au NRs

We first analyze the size dependence of the width of the surface plasmon resonance (SPR). To obtain the SPR band width, the absorption spectra of CdS-Au are fitted to a sum of three components as shown in Figure 6.3A: the absorption of CdS NR (green line), Au SPR band (gray line) and continuous Au interband transition with an onset at around 2.4 eV (violet line). The CdS NR absorption is taken to be the same as that prior to the addition of the Au tip, which is

independently measured (black line in Figure 6.2A). The fit for the CdSAu5.0nm sample is shown in Figure 6.3A and the fits for other samples are shown in Figure A.6.4 A-C. For samples with Au diameter >1.9 nm, the plasmon band is well defined and the position and width can be accurately determined from the fit. For the two lowest size (diameter < 1.9nm), the SPR bands cannot be well determined and thus are not fitted. To examine whether the attachment on the CdS NR affects the width the Au plasmon band, we also prepared colloidal gold particles (without CdS) of similar diameters following a published procedure (see chapter 2 and Figure A.6.3 A-C).[40, 41] Their UV-Vis absorption spectra (Figure A.6.3 D-F) show that the widths of their plasmon band also change with size and these spectra can be fitted by a sum of the SPR band and interband transition. The details of fitting procedures for both Au nanoparticles and CdS-Au NRs are described in Appendix 2. As shown in Figure 6.3B, the SPR band widths obtained from the fits show a linear dependence on 1/R (Au tip radius) for both the gold colloidal nanoparticles and CdS-Au NRs.

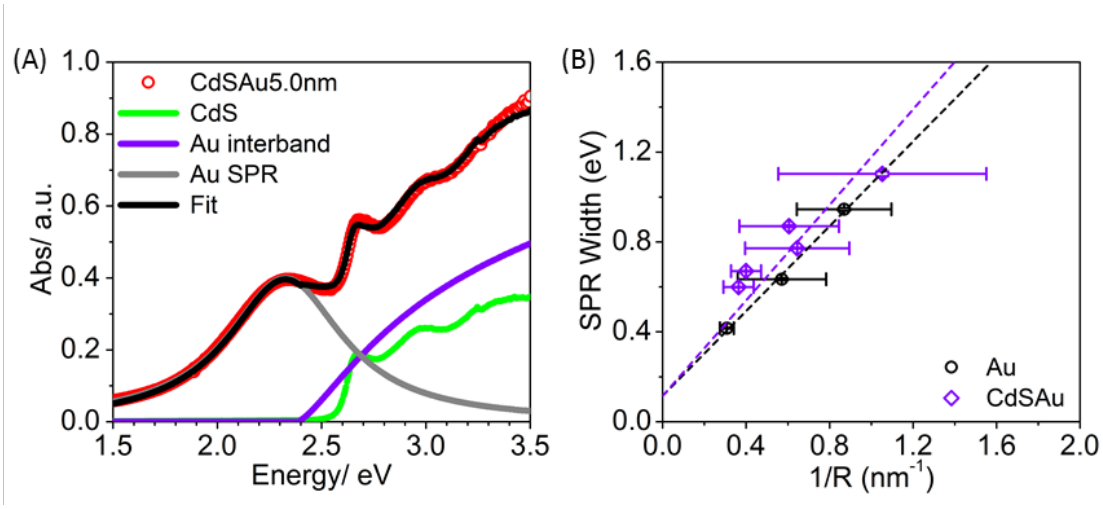

Figure 6.3. Size dependent width of Au plasmon band in CdS-Au NRs and Au nanoparticles. (A) The measured absorption spectrum of CdSAu5.0nm sample (red circles) and its fit (black line) to the sum of three 3 components: free CdS NR absorption (green line), Au interband absorption (violet line), and Au SPR band (gray line). (B) The SPR band widths in pure Au nanoparticles and

CdS-Au NRs as a function of 1/R (R is the radius of Au particle) and their linear fits (Eq 6.1 and 6.2).

The SPR width is determined by the total plasmon dephasing rate, if inhomogeneous broadening due to size and shape distributions can be neglected.[42, 43] The total plasmon dephasing rate (γ_{total}) can be described by the sum of bulk dephasing rate, surface dephasing and interfacial dephasing, as shown in Equation (Eq) (6.1).

$$\Gamma_{tot} = \gamma_{bulk} + \gamma_{sur} + \gamma_{int} \qquad (6.1)$$

The bulk plasmon dephasing rate (γ_{bulk}) contains both the interband and intraband contributions (Figure 6.1A). The former involves the excitation of the electron from the d to sp band; The latter process involves excitation of electrons within the sp band and requires the scattering with phonons, impurities, or defects within the bulk crystal. [30, 43] When the particle size is smaller than or comparable to the mean free path (~50nm in Au[42]), electron scattering with surface leads to additional surface dephasing contribution (γ_{sur}). The surface dephasing rate can be expressed by Eq. (6.2), where A is a dimensionless scaling factor and R is the radius of the Au particle.[43]

$$\Gamma_{sur} = A\frac{V_F}{R} \qquad (6.2)$$

The third term γ_{int} in Equation (6.1) accounts an additional plasmon damping resulted from the interaction of the plasmonic particle with another material, such as semiconductors or molecules, through energy transfer,[44, 45] chemical interface damping[30, 31, 46, 47] or PICTT.[28]

As shown in Figure 6.3B, the total SPR dephasing rates of Au nanoparticles in solution and on CdS-Au NRs depend linearly on 1/R and can be well fit by Eq. (6.1) and (6.2). The bulk SPR width of pure Au obtained from the intercepts of the linear fit is 0.11±0.04 eV, which correspond to a bulk dephasing rate of 11.9±4.3 fs, consistent with previously reported values (~70 meV in gold nanorod) [47, 48]. To fit the CdS-Au band widths, the bulk dephasing rate is fixed at 0.11 eV, same

as pure Au. The slopes of the linear fit for Au and CdS-Au samples are 0.94±0.06 eVnm, 1.06±0.08 eVnm, respectively, from which the scaling factor A in Eq. (6.2) is estimated to be 0.51±0.03 and 0.57±0.04 for these samples. These A values are consistent with the reported results, ranging from 0.2 to around 2.[39, 43] Within the error of this measurement, the fitted values of the slope are the same for Au colloidal nanoparticles and CdS-Au nanorods, which indicates negligible broadening of the Au plasmon band by the CdS NR (i.e. negligible γ_{int}). Thus, the broadening of the SPR band with decreasing Au sizes can be attributed mainly to increased Au surface scattering contributions.[39]

6.2.3 Transient IR absorption of CdS-Au NRs

We used transient absorption (TA) spectroscopy to directly measure the PHET QE from the Au tip to CdS NR as a function the Au particle size following previously developed procedures.[27, 28] In these measurements, CdS-Au NRs are excited at 595 nm to selectively excite the Au particle and the transfer of electrons to the CdS nanorod is monitored at 3700 nm, the mid-IR intraband electron transition from the $1\sum$ to $1\prod$ level within the CdS conduction band.[27, 49] The TA kinetics of CdSAu1.7nm is shown in Figure 6.4A, and the kinetics of other CdS-Au samples are shown in Figure A.6.5. Previous studies have also shown that 590 nm excitation of a control sample consisted of separated Au nanoparticles and CdS nanorods of the same concentrations (adjusted to reach the same CdS and Au ODs as the CdS-Au sample) produces negligible TA signals in the mid IR region and the observed signal in the CdS-Au samples can be attributed to the transferred electrons in the CdS conduction band.[27, 28] Electron transfer from the Au tip to CdS can also be probed by transient absorption spectroscopy in the visible, monitoring the bleach of the CdS exciton band. [27] Visible pump-probe results for selected samples are shown in Appendix 4. As shown in Figure A.6.6A and C, an instrument response time limited formation of CdS exciton

bleach is observed, which is consistent with the instantaneous formation of the transient IR signal (Figure 6.4A and Figure A.6.5), confirming hot electron transfer from the Au to CdS upon the excitation of the Au plasmon band. We have also shown previously that in a control sample of isolated CdS NRs and Au, excitation of the Au plasmon band does not lead to CdS exciton bleach signal, which confirms that hot electron transfer occurs only in CdS NRs with Au tips.[27] Because of the overlap of the CdS exciton bleach and the Au plasmon band in the visible region, a reliable extract of the CdS exciton signal amplitude and kinetics at early delay time is difficult. For this reason, we focus on transient IR measurement and analysis in the remainder of this chapter.

The rise of the signal can be attributed to the electron transfer for the Au nanoparticle to the CdS NR. The best fits of the data, as shown in Figure 6.4A and Figure A.6.5, reveal a rise time of ~ 10 fs in all samples (see Table A.6.3), much faster than the instrument response time of 140±5 fs. Thus, neither the accurate value of the rise time nor its Au size dependence are well determined in this measurement. The decay is attributed tentatively to back electron transfer from CdS to Au nanoparticle, although it can also be caused by trapping of electron by defect states. The decay process can be fit to biexponential decay functions and the fitting parameters are listed in **Table A.6.3**. The decay consists of a fast decay component with lifetime ~1-10 ps and a slow component with lifetime of 100s ps. The half lifetime time ranges from 15.6±0.3 ps in CdSAu1.6nm to ~1-2 ps in larger size. These hot electron transfer and decay times are similar to that reported previously for CdS-Au sample, 1.83±0.22 ps with Au size of 5.4±1.4 nm.[27] Furthermore, the comparison of the kinetics of CdS-Au samples of different Au sizes (Figure A.6.5) shows that the decay kinetics appears to become faster in samples with larger Au sizes, with the exception of CdSAu3.3nm sample, which shows the fastest decay. The rate of electron recombination from the CdS conduction to Au nanoparticle depends on the coupling strength of Au/CdS interface and the

density of Au states at the energy of CdS conduction band. We speculate that the coupling strength likely increases with larger Au size due to the increase of CdS/Au contact areas until the Au size exceeds the CdS NR diameter. The density of states in Au should also increases with larger Au diameter. Both factors suggest that the recombination rate should increase with the Au particle size. The observed non-single exponential recombination kinetics likely reflects the heterogeneity of coupling strength and density of states at the Au/CdS interface. The observed Au size dependence of the recombination kinetics is largely consistent with this expected trend, although there are exceptions to this trend, suggesting the complexity of the CdS/Au interface and the presence of other factors that have not been considered in the simple model.

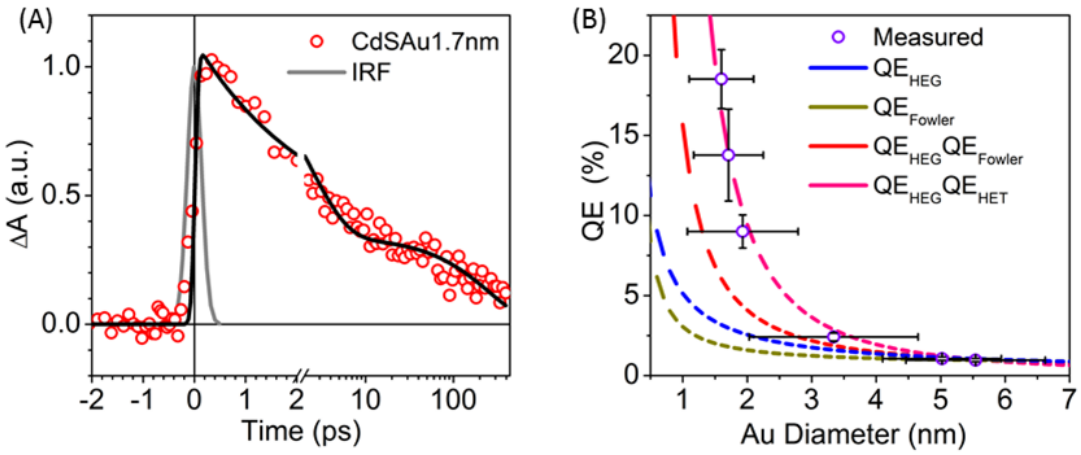

Figure 6.4. Size dependence PHET in CdS-Au NRs probed by transient absorption (TA) spectroscopy with 595 nm excitation. (A) TA kinetics of PHET in CdSAu1.7nm (red circles) monitored by the intraband absorption of electrons in CdS conduction band at 3700 nm and its fit (black curve) to an instrument response limited rise and biexponential decay function. Also shown is the instrument response function (IRF) measured in a 1mm silicon wafer (gray dashed line). (B) The measured Au to CdS PHET QE as a function of Au sizes (violet circles) and its fit by functions that account for $QE_{HEG}(R)$ (Eq.(6.4), dashed blue curve), $QE_{Fowler}(R)$ (Eq. (6.5), dashed olive

curve), $\mathrm{QE_{HEG}(R)QE_{Fowler}(R)}$ (dashed red curve), and $\mathrm{QE_{HEG}(R)QE_{HET}(R)}$ (Eq.(6.6),dashed pink line).

6.2.4 Quantification of plasmon-induced hot electron transfer quantum yield

The PHET QEs of CdS-Au NRs are calculated from the peak amplitude of the TA IR signal.[27] The details of efficiency calculation are described in Appendix 5. The measured electron signal amplitudes increase linearly with the excitation fluence (see Figure A.6.7 for an example), suggesting that the hot electron transfer efficiency is independent of the excitation flux under our experimental conditions. The measured PHET QEs are plotted as a function of the Au tip size in Figure 6.4B, showing that the QE increases from ~1% to ~18% as the particle size decreases from 5.5±1.1 nm to 1.6±0.5 nm. As discussed above (Figure 6.3B), the damping of the SPR band in CdS-Au NRs contains negligible contribution of CdS. Thus, the PHET process can be described by the conventional model, in which the hot electron is first generated by plasmon decay and then transferred to CdS. The PHET QE is a product of the QEs of hot electron generation (QE_{HEG}) in Au and hot electron transfer to CdS (QE_{HET}), as shown in Eq. (6.3).[27]

$$QE_{PHET}(R) \propto QE_{HEG}(R)QE_{HET}(R) \qquad (6.3)$$

6.2.5 Understanding the size-dependence of quantum yields

The Au particles studied in this chapter have diameters < 6 nm. At this size regime, the plasmon decays predominately by exciting e-h pairs through the d-sp interband transitions and/or sp-sp intraband transitions, with negligible contributions of radiative decay/scattering.[30] Recent computational studies have shown that the decay of plasmons in Au through the interaband pathway generates hot holes in the d band that is 1.6-1.8 eV below the Fermi level and electrons near the Fermi level (Figure 6.1A); plasmon decay through the sp-sp intraband transition produces

nearly uniform distribution of hot electrons and hot holes up to the photon energy above and below, respectively, the Fermi level (Figure 6.1A), although this process is inefficient in bulk Au because it requires the involvement of phonons.[17, 18] At small particle size, strong surface scattering and spatial confinement relaxes momentum conservation requirement and can induce plasmon decay by exciting the sp-sp intraband transitions to produce hot electrons with sufficient energy above the barrier E_b. Following the model of Govorov and co-workers, the hot electron generation efficiency in our samples can be thought to be proportional to the ratio of the surface damping to the total plasmon damping rate, as shown in Eq. (6.4).[18]

$$\mathrm{QE_{HEG}(R)} \propto \frac{\gamma_{sur}(R)}{\gamma_{\mathrm{total}}(R)} \qquad (6.4)$$

Among the hot electrons above the Fermi level, only a portion of them has the required energy and momentum to cross the metal/semiconductor interface, which can be accounted for by Fowler's model.[21] The competition of hot electron transfer with hot carrier relaxation further reduces the quantum efficiency by a factor of α. As a result, the total hot electron transfer efficiency is given by Eq. (6.5)

$$\mathrm{QE_{HET}(R)} = \alpha(R)\mathrm{QE_{Fowler}(R)} = \alpha(R)\frac{\left(\hbar\omega - \mathrm{E_b}(R)\right)^2}{\hbar\omega} \qquad (6.5)$$

In Eq. (6.5), $\hbar\omega$ is the photon energy.

From the fitting parameters obtained in Figure 6.3B and using Eq. (6.4), we can calculate $\mathrm{QE_{HEG}}$® as a function of Au size. As shown by the blue line in Figure 6.4B, the calculated $\mathrm{QE_{HEG}}$® increases at small Au particle size due to an increase in the surface damping contribution. Because of a barrier between the Au and CdS conduction band, as shown in Figure 6.1B, only hot electrons with energy above this barrier can be transferred to CdS. The barrier height (E_b) is determined by the energy difference between the CdS conduction band edge (E_{CB}=-3.6 eV vs vacuum)[50, 51] and gold Fermi level (E_f). It has been reported that the E_f of small Au particle size

can differ from its bulk value (E_{bulk} =-5.1 eV vs vacuum)[50, 52] due to the charging energy of small particles: $E_f(R)=E_{bulk}+\frac{e^2}{4\pi\varepsilon\varepsilon_0 R}$ (versus vacuum),[52, 53] in which e is the electron charge, ε is the relative permittivity (=4.8 for chloroform[54]) and ε_0 is the vacuum permittivity. $E_b(R)$ values are estimated to decrease from ~1.5 eV in CdSAu5.5nm to ~1.1 eV in CdSAu1.6nm. As a result, the calculated $QE_{Fowler}(R)$ increases at smaller R due to a decrease in the barrier height (Figure 6.4B, olive line).

It is clear that both QE_{HEG}® and $QE_{Fowler}(R)$ alone are insufficient to account for the observed size dependence of QE_{PHET}®. Also shown in Figure 6.4B (red line) is the product of QE_{HEG}® and $QE_{Fowler}(R)$ as a function of size, which better captures the overall trend of the size dependence of the measured PHET QE. At smaller Au particle sizes both the QE for hot electron generation and transfer increases, which combine to give rise to a rapid increase of hot electron efficiency. However, it still cannot fully account for the observed size dependence and additional size dependence factors are needed. It is possible that the scaling factor α in Eq. (6.5) also changes with particle size. Assuming that □scales with 1/R, the computed efficiency according to Eq. (6.3) fits the observed trend well, as shown by the pink line in Figure 6.4B. α is given by the competition of hot electron transfer and thermalization according to Eq. (6.6).

$$\alpha(R) = \frac{k_{ET}(R)}{k_{ET}(R) + k_{Th}(R)} \qquad (6.6)$$

In Eq (6.6), $k_{ET}(R)$, and $k_{Th}(R)$ are hot electron transfer and relaxation rates, respectively. The square module of the electron coupling strength should be proportional to the integral of electron density at Au surface ($\propto 1/R^3$) over the CdS/Au contact surface($\propto R^2$), giving rise to $k_{ET}(R)$ that approximately scales with 1/R. $k_{Th}(R)$ is dominant by the electron-electron scattering for high energy electrons. It has been reported that the electron scattering life time decreases with particle

size, which can be attributed to reduced screening between the conduction band electrons and core electrons near the nanoparticle surface. [55] The difference in the size dependence of hot electron transfer and thermalization complicates the analytical expression of $\alpha(R)$. In the limit that $k_{Th}(R) \ll k_{ET}(R)$, $\alpha(R)$ should approach 1 and becomes size independent, which clearly is not consistent with our observation. In the limit of $k_{Th}(R) \gg k_{ET}(R)$, and the size dependence of ET rate is more pronounced than the thermalization rate, $\alpha(R)$ becomes proportional to 1/R and is <<1. Our result appears to be consistent with this limit. Furthermore, A*b initio* calculation results have shown that the electron scattering lifetime of electron energy about 2 eV above the Fermi level is around 10-20 fs.[56] This value is close to our fit of the TA IR signal growth time constant, which is also consistent with the limit of $k_{Th}(R) \gg k_{ET}(R)$.

It should be noted that in the analysis above, we have not accounted for the heterogeneous distribution of Au particle sizes in the samples. This can be done by convoluting the computed curves shown in Figure 6.4 with the experimentally determined size distribution (Table A.6.2). The calculated results are shown in Figure A.6.8 and further details are provided in Section Appendix 6. It is clear that accounting for the Au size distribution leads to notable changes in the computed values for the various efficiencies described above, but it does not affect the overall trend and qualitative conclusions.

Another possible reason for the deviation at smaller particle size may be caused by a change in the nature of electronic transitions. For Au nanoparticles with diameters <2 nm, a previous theoretical study has suggested that there may exist discrete dipolar transitions that can be coupled to plasmon decay;[18] and the particles may even become non-metallic with optical absorption spectra that are dominated by discrete electronic transitions instead of plasmon bands.[57-60] This

non-metallicity may open a band gap, which may shift the energy levels of Au in small particles, similar to what we discussed in the Fowler's model.

6.3 Conclusion

In summary, in this chapter, we examine how the plasmon-induced hot electron transfer efficiency depends on the size of the Au tip in CdS-Au nanorod heterostructures. These colloidal nanorods enable systematic variation of Au tip size without changing the CdS NRs. Using time-resolved visible pump/IR probe spectroscopy, both the kinetics and the quantum efficiency of plasmon-induced hot electron transfer are directly measured. We show that for CdS-Au nanorods, the Au SPR band width increases linearly with 1/R and this trend is the same as isolated colloidal Au nanoparticles, suggesting that the increases of plasmon dephasing rate at smaller Au size can be attributed to enhanced surface dephasing rates with negligible contribution from CdS/Au interaction. Optical excitation of the Au particle at 595nm leads to plasmon-induced hot electron transfer from the Au to CdS with a time constant much faster than the instrument response time of this measurement (<<140 fs) and the transferred electron decay back to Au on the 1 to 10 ps time scale; the plasmon induced hot electron transfer QE increases from ~1% to~18% as the particle size decreases from 5.5±1.1 nm to 1.6±0.5 nm. The overall photon to hot electron transfer process can be understood by the conventional hot electron transfer model, in which hot electrons are first generated in Au by plasmon decay and then undergo interfacial transfer to CdS. With decreasing Au particles size, the efficiency of hot electron generation increases due to enhanced surface damping contribution; the efficiency of hot electron transfer increases due to decrease barrier height and possibly enhanced electronic coupling at the Au/CdS interface; and these factors combine to give rise to the observed size dependent PHET QEs. Our findings suggest that an efficient approach to increase the efficiency of plasmon induced hot electron transfer is to decrease

the size of the plasmon particle, which offers important guidance for the rational design of efficient plasmonic hot carrier-based devices.

References

1. Clavero, C., Plasmon-induced hot-electron generation at nanoparticle/metal-oxide interfaces for photovoltaic and photocatalytic devices. *Nat. Photon.* **2014,** *8* (2), 95-103.
2. Linic, S.; Christopher, P.; Ingram, D. B., Plasmonic-metal nanostructures for efficient conversion of solar to chemical energy. *Nat. Mater.* **2011,** *10* (12), 911-921.
3. Warren, S. C.; Thimsen, E., Plasmonic solar water splitting. *Energy Environ. Sci.* **2012,** *5*, 5133-5146.
4. Kang, Y.; Najmaei, S.; Liu, Z.; Bao, Y.; Wang, Y.; Zhu, X.; Halas, N. J.; Nordlander, P.; Ajayan, P. M.; Lou, J.; Fang, Z., Plasmonic hot electron induced structural phase transition in a MoS2 monolayer. *Adv. Mater.* **2014,** *26* (37), 6467-6471.
5. Seemala, B.; Therrien, A. J.; Lou, M.; Li, K.; Finzel, J. P.; Qi, J.; Nordlander, P.; Christopher, P., Plasmon-Mediated Catalytic O2 Dissociation on Ag Nanostructures: Hot Electrons or Near Fields? *ACS Energy Lett.* **2019**, 1803-1809.
6. Brongersma, M. L.; Halas, N. J.; Nordlander, P., Plasmon-induced hot carrier science and technology. *Nat. Nanotechnol.* **2015,** *10* (1), 25-34.
7. Zhou, L.; Swearer, D. F.; Zhang, C.; Robatjazi, H.; Zhao, H.; Henderson, L.; Dong, L.; Christopher, P.; Carter, E. A.; Nordlander, P.; Halas, N. J., Quantifying hot carrier and thermal contributions in plasmonic photocatalysis. *Science* **2018,** *362* (6410), 69-72.
8. Kamarudheen, R.; Castellanos, G. W.; Kamp, L. P. J.; Clercx, H. J. H.; Baldi, A., Quantifying Photothermal and Hot Charge Carrier Effects in Plasmon-Driven Nanoparticle Syntheses. *ACS Nano* **2018,** *12* (8), 8447-8455.
9. Linic, S.; Aslam, U.; Boerigter, C.; Morabito, M., Photochemical transformations on plasmonic metal nanoparticles. *Nat. Mater.* **2015,** *14* (6), 567-576.
10. Mukherjee, S.; Libisch, F.; Large, N.; Neumann, O.; Brown, L. V.; Cheng, J.; Lassiter, J. B.; Carter, E. A.; Nordlander, P.; Halas, N. J., Hot electrons do the impossible: plasmon-induced dissociation of H2 on Au. *Nano Lett.* **2013,** *13* (1), 240-247.
11. Yu, Y.; Wijesekara, K. D.; Xi, X.; Willets, K. A., Quantifying Wavelength-Dependent Plasmonic Hot Carrier Energy Distributions at Metal/Semiconductor Interfaces. *ACS Nano* **2019,** *13* (3), 3629-3637.
12. Knight, M. W.; Sobhani, H.; Nordlander, P.; Halas, N. J., Photodetection with Active Optical Antennas. *Science* **2011,** *332* (6030), 702-704.
13. Mubeen, S.; Hernandez-Sosa, G.; Moses, D.; Lee, J.; Moskovits, M., Plasmonic photosensitization of a wide band gap semiconductor: converting plasmons to charge carriers. *Nano Lett.* **2011,** *11* (12), 5548-5552.
14. Sobhani, A.; Knight, M. W.; Wang, Y.; Zheng, B.; King, N. S.; Brown, L. V.; Fang, Z.; Nordlander, P.; Halas, N. J., Narrowband photodetection in the near-infrared with a plasmon-induced hot electron device. *Nat. Commun.* **2013,** *4*, 1643.
15. Giugni, A.; Torre, B.; Toma, A.; Francardi, M.; Malerba, M.; Alabastri, A.; Proietti Zaccaria, R.; Stockman, M. I.; Di Fabrizio, E., Hot-electron nanoscopy using adiabatic compression of surface plasmons. *Nat. Nanotechnol.* **2013,** *8* (11), 845-852.

16. Furube, A.; Du, L.; Hara, K.; Katoh, R.; Tachiya, M., Ultrafast plasmon-induced electron transfer from gold nanodots into TiO2 nanoparticles. *J. Am. Chem. Soc.* **2007,** *129* (48), 14852-14853.
17. Brown, A. M.; Sundararaman, R.; Narang, P.; Goddard, W. A.; Atwater, H. A., Nonradiative Plasmon Decay and Hot Carrier Dynamics: Effects of Phonons, Surfaces, and Geometry. *ACS Nano* **2016,** *10* (1), 957-966.
18. Besteiro, L. V.; Kong, X.-T.; Wang, Z.; Hartland, G.; Govorov, A. O., Understanding Hot-Electron Generation and Plasmon Relaxation in Metal Nanocrystals: Quantum and Classical Mechanisms. *ACS Photonics* **2017,** *4* (11), 2759-2781.
19. Manjavacas, A.; Liu, J. G.; Kulkarni, V.; Nordlander, P., Plasmon-Induced Hot Carriers in Metallic Nanoparticles. *ACS Nano* **2014,** *8* (8), 7630-7638.
20. Sundararaman, R.; Narang, P.; Jermyn, A. S.; Goddard Iii, W. A.; Atwater, H. A., Theoretical predictions for hot-carrier generation from surface plasmon decay. *Nat. Commun.* **2014,** *5* (1), 5788.
21. Fowler, R. H., The Analysis of Photoelectric Sensitivity Curves for Clean Metals at Various Temperatures. *Phys. Rev.* **1931,** *38* (1), 45-56.
22. Hartland, G. V., Optical studies of dynamics in noble metal nanostructures. *Chem. Rev.* **2011,** *111* (6), 3858-3887.
23. Aruda, K. O.; Tagliazucchi, M.; Sweeney, C. M.; Hannah, D. C.; Weiss, E. A., The role of interfacial charge transfer-type interactions in the decay of plasmon excitations in metal nanoparticles. *Phys. Chem. Chem. Phys.* **2013,** *15* (20), 7441-7449.
24. Burda, C.; Chen, X.; Narayanan, R.; El-Sayed, M. A., Chemistry and Properties of Nanocrystals of Different Shapes. *Chem. Rev.* **2005,** *105* (4), 1025-1102.
25. Boerigter, C.; Aslam, U.; Linic, S., Mechanism of Charge Transfer from Plasmonic Nanostructures to Chemically Attached Materials. *ACS Nano* **2016,** *10*, 6108-6115.
26. Govind Rao, V.; Aslam, U.; Linic, S., Chemical requirement for extracting energetic charge carriers from plasmonic metal nanoparticles to perform electron-transfer reactions. *J. Am. Chem. Soc.* **2019,** *141*, 643-647.
27. Wu, K.; Rodríguez-Córdoba, W. E.; Yang, Y.; Lian, T., Plasmon-Induced Hot Electron Transfer from the Au Tip to CdS Rod in CdS-Au Nanoheterostructures. *Nano Lett.* **2013,** *13* (11), 5255-5263.
28. Wu, K.; Chen, J.; McBride, J. R.; Lian, T., Efficient hot-electron transfer by a plasmon-induced interfacial charge-transfer transition. *Science* **2015,** *349* (6248), 632-635.
29. Cushing, S. K.; Chen, C. J.; Dong, C. L.; Kong, X. T.; Govorov, A. O.; Liu, R. S.; Wu, N., Tunable Nonthermal Distribution of Hot Electrons in a Semiconductor Injected from a Plasmonic Gold Nanostructure. *ACS Nano* **2018,** *12*, 7117-7126.
30. Hovel, H.; Fritz, S.; Hilger, A.; Kreibig, U.; Vollmer, M., Width of cluster plasmon resonances: Bulk dielectric functions and chemical interface damping. *Phys. Rev. B* **1993,** *48* (24), 18178-18188.
31. Bosbach, J.; Hendrich, C.; Stietz, F.; Vartanyan, T.; Trager, F., Ultrafast dephasing of surface plasmon excitation in silver nanoparticles: influence of particle size, shape, and chemical surrounding. *Phys. Rev. Lett.* **2002,** *89* (25), 257404.
32. Therrien, A. J.; Kale, M. J.; Yuan, L.; Zhang, C.; Halas, N. J.; Christopher, P., Impact of chemical interface damping on surface plasmon dephasing. *Faraday Discuss.* **2019,** *214* (0), 59-72.

33. Persson, B. N. J., Polarizability of small spherical metal particles: influence of the matrix environment. *Surf. Sci.* **1993,** *281* (1), 153-162.
34. Valenti, M.; Venugopal, A.; Tordera, D.; Jonsson, M. P.; Biskos, G.; Schmidt-Ott, A.; Smith, W. A., Hot Carrier Generation and Extraction of Plasmonic Alloy Nanoparticles. *ACS Photonics* **2017,** *4* (5), 1146-1152.
35. Narang, P.; Sundararaman, R.; Atwater, H. A., Plasmonic hot carrier dynamics in solid-state and chemical systems for energy conversion. *Nanophotonics* **2016,** *5* (1), 96-111.
36. Habas, S. E.; Yang, P.; Mokari, T., Selective Growth of Metal and Binary Metal Tips on CdS Nanorods. *J. Am. Chem. Soc.* **2008,** *130* (11), 3294-3295.
37. O'Sullivan, C.; Gunning, R. D.; Barrett, C. A.; Singh, A.; Ryan, K. M., Size controlled gold tip growth onto II–VI nanorods. *J. Mater. Chem.* **2010,** *20* (36), 7875-7880.
38. Shabaev, A.; Efros, A. L., 1D Exciton Spectroscopy of Semiconductor Nanorods. *Nano Lett.* **2004,** *4* (10), 1821-1825.
39. Alvarez, M. M.; Khoury, J. T.; Schaaff, T. G.; Shafigullin, M. N.; Vezmar, I.; Whetten, R. L., Optical Absorption Spectra of Nanocrystal Gold Molecules. *J. Phys. Chem. B* **1997,** *101* (19), 3706-3712.
40. Inoue, Y.; Tsutamoto, Y.; Muko, D.; Nanamura, K.; Sawada, T.; Niidome, Y., Stepwise Preparation of Spherical Gold Nanoparticles Passivated with Cationic Amphiphiles. *Anal. Sci.* **2016,** *32* (8), 875-880.
41. Khon, E.; Mereshchenko, A.; Tarnovsky, A. N.; Acharya, K.; Klinkova, A.; Hewa-Kasakarage, N. N.; Nemitz, I.; Zamkov, M., Suppression of the plasmon resonance in Au/CdS colloidal nanocomposites. *Nano Lett.* **2011,** *11* (4), 1792-1709.
42. Link, S.; El-Sayed, M. A., Size and Temperature Dependence of the Plasmon Absorption of Colloidal Gold Nanoparticles. *J. Phys. Chem. B* **1999,** *103* (21), 4212-4217.
43. Kreibig, U.; Vollmer, M., Theoretical Considerations. In *Optical Properties of Metal Clusters*, Springer Berlin Heidelberg: Berlin, Heidelberg, 1995; pp 13-201.
44. Li, J.; Cushing, S. K.; Meng, F.; Senty, T. R.; Bristow, A. D.; Wu, N., Plasmon-induced resonance energy transfer for solar energy conversion. *Nat. Photon.* **2015,** *9* (9), 601-607.
45. Govorov, A. O.; Lee, J.; Kotov, N. A., Theory of plasmon-enhanced Förster energy transfer in optically excited semiconductor and metal nanoparticles. *Phys. Rev. B* **2007,** *76* (12), 125308.
46. Foerster, B.; Spata, V. A.; Carter, E. A.; Sönnichsen, C.; Link, S., Plasmon damping depends on the chemical nature of the nanoparticle interface. *Sci. Adv.* **2019,** *5* (3), eaav0704.
47. Foerster, B.; Joplin, A.; Kaefer, K.; Celiksoy, S.; Link, S.; Sonnichsen, C., Chemical Interface Damping Depends on Electrons Reaching the Surface. *ACS Nano* **2017,** *11* (3), 2886-2893.
48. Novo, C.; Gomez, D.; Perez-Juste, J.; Zhang, Z.; Petrova, H.; Reismann, M.; Mulvaney, P.; Hartland, G. V., Contributions from radiation damping and surface scattering to the linewidth of the longitudinal plasmon band of gold nanorods: a single particle study. *Phys. Chem. Chem. Phys.* **2006,** *8* (30), 3540-3546.
49. Olshansky, J. H.; Balan, A. D.; Ding, T. X.; Fu, X.; Lee, Y. V.; Alivisatos, A. P., Temperature-Dependent Hole Transfer from Photoexcited Quantum Dots to Molecular Species: Evidence for Trap-Mediated Transfer. *ACS Nano* **2017,** *11* (8), 8346-8355.
50. Ben-Shahar, Y.; Scotognella, F.; Kriegel, I.; Moretti, L.; Cerullo, G.; Rabani, E.; Banin, U., Optimal metal domain size for photocatalysis with hybrid semiconductor-metal nanorods. *Nat. Commun.* **2016,** *7*, 10413.

51. Chen, S.; Wang, L.-W., Thermodynamic Oxidation and Reduction Potentials of Photocatalytic Semiconductors in Aqueous Solution. *Chem. Mater.* **2012,** *24* (18), 3659-3666.
52. Zhang, Y.; Pluchery, O.; Caillard, L.; Lamic-Humblot, A. F.; Casale, S.; Chabal, Y. J.; Salmeron, M., Sensing the charge state of single gold nanoparticles via work function measurements. *Nano Lett.* **2015,** *15* (1), 51-55.
53. Ingram, R. S.; Hostetler, M. J.; Murray, R. W.; Schaaff, T. G.; Khoury, J. T.; Whetten, R. L.; Bigioni, T. P.; Guthrie, D. K.; First, P. N., 28 kDa Alkanethiolate-Protected Au Clusters Give Analogous Solution Electrochemistry and STM Coulomb Staircases. *J. Am. Chem. Soc.* **1997,** *119* (39), 9279-9280.
54. Wolf, M. G.; Groenhof, G., Evaluating nonpolarizable nucleic acid force fields: a systematic comparison of the nucleobases hydration free energies and chloroform-to-water partition coefficients. *J. Comput. Chem.* **2012,** *33* (28), 2225-2232.
55. Voisin, C.; Christofilos, D.; Loukakos, P. A.; Del Fatti, N.; Vallée, F.; Lermé, J.; Gaudry, M.; Cottancin, E.; Pellarin, M.; Broyer, M., Ultrafast electron-electron scattering and energy exchanges in noble-metal nanoparticles. *Physical Review B* **2004,** *69* (19), 195416.
56. Ladstädter, F.; Hohenester, U.; Puschnig, P.; Ambrosch-Draxl, C., First-principles calculation of hot-electron scattering in metals. *Physical Review B* **2004,** *70* (23), 235125.
57. Zhou, M.; Higaki, T.; Li, Y.; Zeng, C.; Li, Q.; Sfeir, M. Y.; Jin, R., Three-Stage Evolution from Nonscalable to Scalable Optical Properties of Thiolate-Protected Gold Nanoclusters. *J. Am. Chem. Soc.* **2019,** *141* (50), 19754-19764.
58. Varnavski, O.; Ramakrishna, G.; Kim, J.; Lee, D.; Goodson, T., Critical Size for the Observation of Quantum Confinement in Optically Excited Gold Clusters. *J. Am. Chem. Soc.* **2010,** *132* (1), 16-17.
59. Zhou, M.; Zeng, C.; Song, Y.; Padelford, J. W.; Wang, G.; Sfeir, M. Y.; Higaki, T.; Jin, R., On the Non-Metallicity of 2.2 nm Au246 (SR)80 Nanoclusters. *Angew. Chem. Int. Ed.* **2017,** *56* (51), 16257-16261.
60. Stoll, T.; Sgro, E.; Jarrett, J. W.; Rehault, J.; Oriana, A.; Sala, L.; Branchi, F.; Cerullo, G.; Knappenberger, K. L., Jr., Superatom State-Resolved Dynamics of the Au25(SC8H9)18(-) Cluster from Two-Dimensional Electronic Spectroscopy. *J. Am. Chem. Soc.* **2016,** *138* (6), 1788-1791.

Appendix 1

TEM image/UV-vis of CdS NRs, CdS-Au NRs and Au NPs

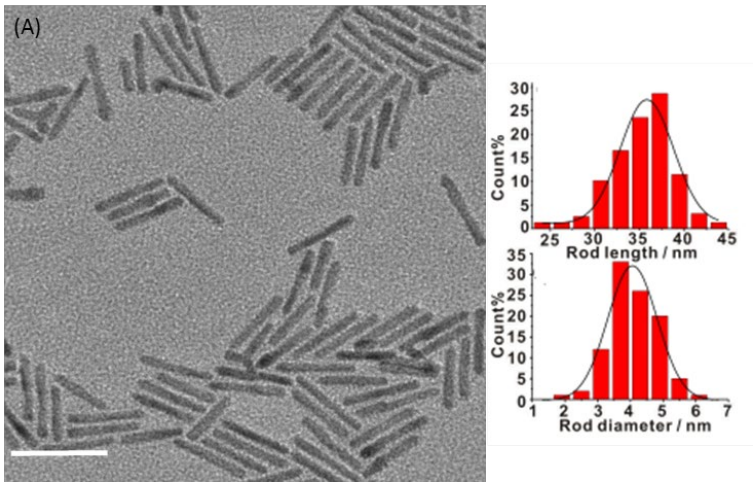

Figure A.6.1. TEM image of CdS NRs, showing an average length of 35.3±3.5 nm and diameter of 4.1±0.7 nm. The scale bar is 50 nm.

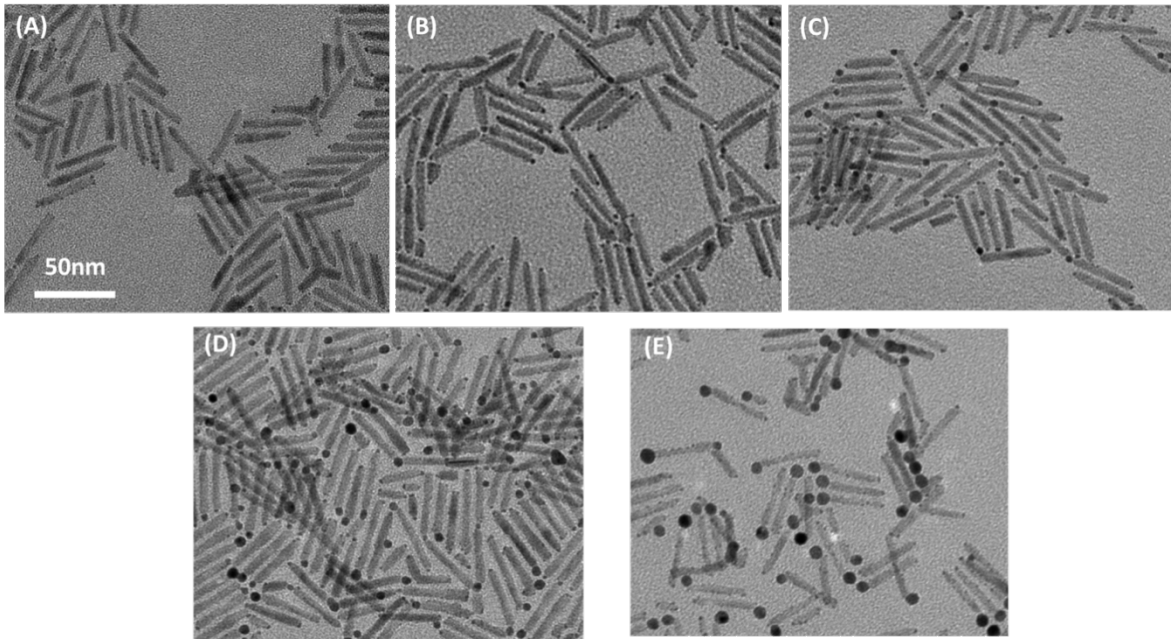

Figure A.6.2. TEM images of (A) CdSAu1.6nm (B) CdSAu1.7nm (C) CdSAu1.9nm (D) CdSAu3.3nm. (E) CdSAu5.5nm. The scales for all panels are the same and indicated in (A).

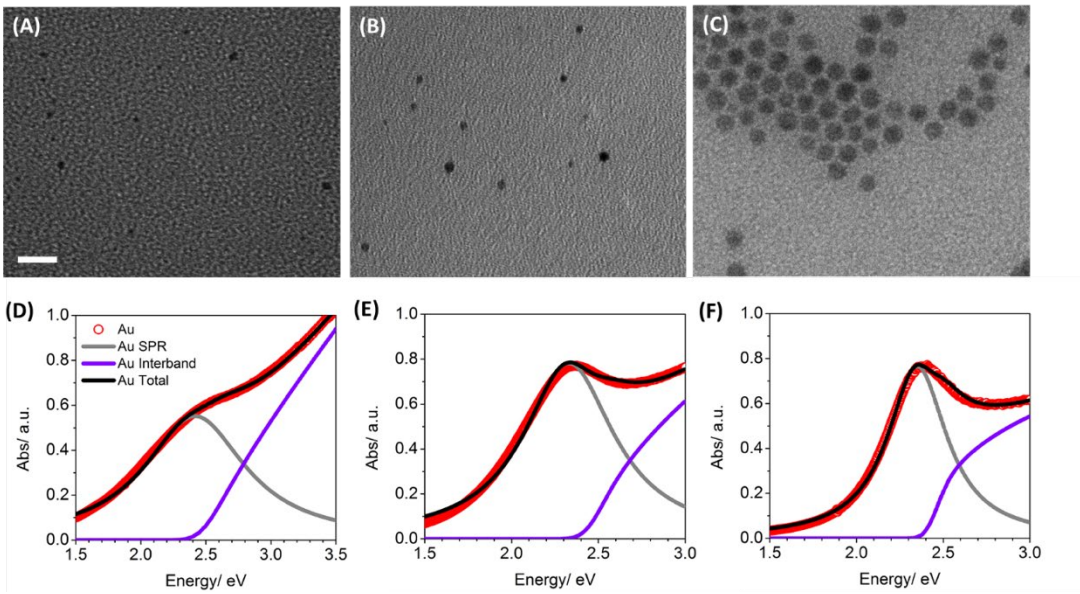

Figure A.6.3. TEM images and absorption spectra of Au nanoparticles (A, D) with diameters of 2.3±0.6 nm, (B,E) 3.5±1.3 nm, and (C,F) 6.5±0.7 nm. The scale bar for the TEM images is 15 nm. These UV-vis spectra (red circles) are fit to a function (black line) consisted of two components, the Au interband transition (violet line) and the Au SPR band (gray line).

Appendix 2

Fitting of absorption of Au and CdS-Au

The absorption of Au particle is fitted by a sum of a SPR band and interband transition with onset around 2.4 eV. The SPR band is fitted with a Lorentzian function, $f_{SPR}(E)$, shown in Eq. (A.6.1).

$$F_{SPR}(E) = \frac{A}{\pi}\frac{\frac{w}{2}}{(E-E_c)^2+\left(\frac{w}{2}\right)^2} \qquad (A.6.1)$$

E_c is the peak center, w is the full-width at the half maximum of the function, A is the amplitude. The interband absorption, $f_{inter}(E)$ is fitted by Eq. (A.6.2).

$$F_{inter}(E) = \int A\left(E - E_{g'}\right)^B \times \frac{1}{\sqrt{2\pi}\sigma} \exp\left[-\frac{(E_{g'}-E_g)^2}{2\pi\sigma^2}\right] dE_{g'} \qquad (A.6.2)$$

An interband transition with certain onset E_g can be described by $A\left(E - E_g\right)^B$. Due to the inhomogeneous size, the onset E_g become uncertain and has a Gaussian distribution associated with this imhomogeneousity. σ is the width of the Gaussian distribution. Thus, the real f_{inter} is a convolution of the interband transition with a Gaussian distribution of E_g. This convolution can be solved numerically. Here, we solved the Eq. (A.6.2) by integrating from 1.9 eV to 3.5 eV with integration internal of 0.05 eV. The fitting results are listed in **Table A.6.1** and **Figure A.6.3 D-F**.

Table A.6.1. Fitting results for pure Au particles

Size/nm	2.3±0.6	3.5±1.3	6.5±0.7
E_c/eV	2.416±0.004	2.328±0.002	2.350±0.001
w/eV	0.945±0.006	0.634±0.005	0.416±0.002
E_g/eV	2.48	2.46	2.44
B	0.85	0.62	0.38
σ/eV	0.10	0.07	0.05

The absorption spectra of CdS-Au are fitted to the sum of 3 components: the Au SPR band, Au interband transition and CdS absorption. The spectrum of CdS is obtained from the independent measure of CdS NRs without Au. The shape of the Au interband transition and the ratio of its amplitude relative to the integrated area of the SPR band are assumed to be the same as in free Au particles examined above. First, we fitted the SPR band with Lorentzian function to get the SPR amplitude, peak position and its band width. With fitted amplitude of SPR, the interband amplitude

can be estimated. Finally, the amount of NR can be determined. The fitted spectra are shown in **Figure A.6.4** and **Figure 6.3A** and the fitting parameters are shown in **Table A.6.2**.

Table A.6.2. Fitting parameters for the SPR bandwidths in CdS-Au NRs

Au in CdSAu(nm)	1.6±0.5	1.7±0.5	1.9±0.9	3.3±1.3	5.0±0.9	5.5±1.1
SPR width (eV)	N.A.	N.A.	1.103 ±0.011	0.870 ±0.004	0.670 ±0.001	0.599 ±0.001

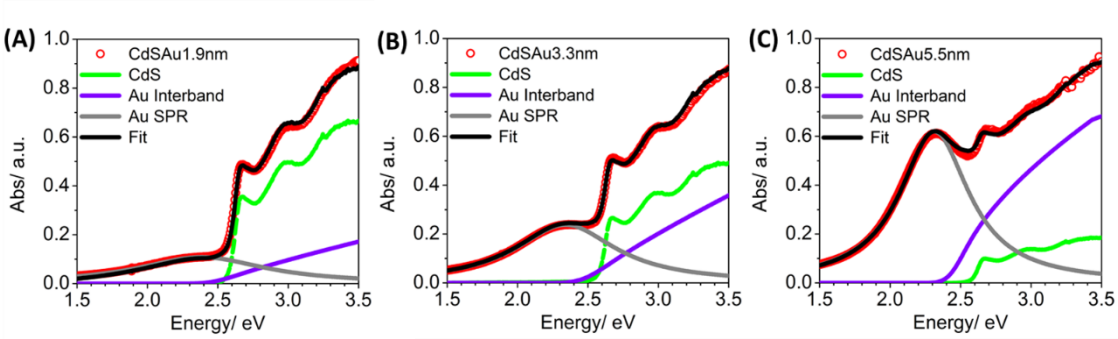

Figure A.6.4. Absorption spectra (red circles) and fits (black lines) of CdS-Au NRs. (A) CdSAu1.9nm (B) CdSAu3.3nm. (C) CdSAu5.5nm. The fit consists of 3 contributions: CdS NR absorption (green line), Au interband transition (violet line), Au SPR band (gray line).

Appendix 3

Transient IR Kinetics of CdS-Au

The TA IR kinetics shown in **Figure 6.4A** and **Figure A.6.5** are well fitted by a single exponential rise and biexponential decay function according to Eq. (A.6.3).

$$S(t) = IRF \otimes \left[A_1 \exp\left(-\frac{t}{T_1}\right) + A_2 \exp\left(-\frac{t}{T_2}\right) - (A_1 + A_2) \exp\left(-\frac{t}{T_f}\right)\right] \qquad (A.6.3)$$

A_i, T_i (i=1,2) are amplitude and time constants of the biexponential function decay function. T_f is the time constant of the signal rise. The IRF of the measurement was determined in a 1mm silicon wafer and can be well modelled by a Gaussian function with a FWHM of ~ 140±5 fs. The best fits to the measured transient IR kinetics to Eq. (A.6.3) are shown in **Figure A.6.5** and **Figure A.6.4A**. The fitting parameters are listed in **Table A.6.3**. The fit shows that the rise time of all data is ~ 10 fs, which is consistent with the expected fast hot electron decay and electron transfer times. However, due to the ultrafast growth (~10fs) compared with the IRF (140fs) and uncertainty (±5 fs) in the IRF, it becomes impossible to accurately determine the rise time, and the rise time should be considered as << 140 fs.

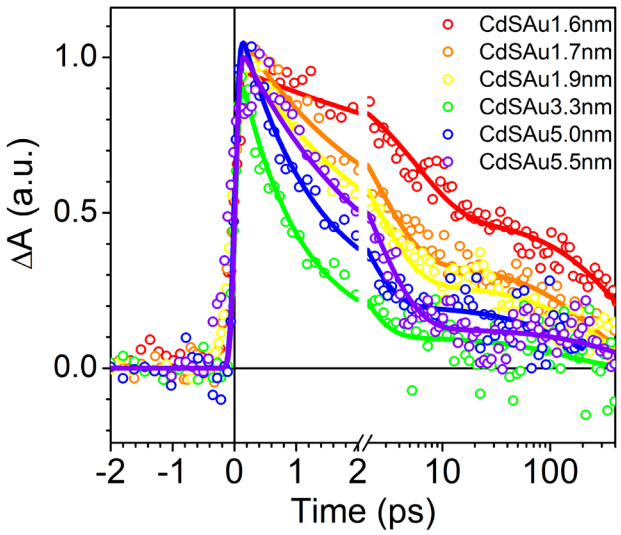

Figure A.6.5. Normalized comparison of transient IR kinetics (open circles) and fit (solid lines) of Au/CdS measured with 595 nm excitation (excitation density ~10-100mW/cm^2) and 3700 nm probe. The fit function is given in Eq. (A.6.3) and fitting parameters are listed in Table A6.3.

Table A.6.3. Fitting parameters for the transient IR kinetics of CdS-Au samples.

	A_1	T_1(ps)	A_2	T_2(ps)	T_f(fs)	$T_{1/2}$(ps)
CdSAu1.6nm	0.50±0.02	5.7±0.7	0.50±0.02	488.3±56.2	11.0±0.5	15.6±3.0
CdSAu1.7nm	0. 70±0.03	2.3±0.2	0.30±0.01	257.4±36.8	10.1±0.3	3.5±0.2
CdSAu1.9nm	0.73±0.03	2.2±0.2	0.27±0.01	278.1±59.1	8.4±0.2	2.6±0.3
CdSAu3.3nm	0.91±0.03	1.0±0.1	0.09±0.01	152.7±71.9	10.0±0.2	0.8±0.1
CdSAu5.0nm	0.82±0.03	1.2±0.1	0.18±0.01	170.7±40.2	6.8±0.1	1.4±0.3
CdSAu5.5nm	0.88±0.04	2.2±0.3	0.12±0.02	441.1±372.0	9.5±0.3	2.0±0.3

Appendix 4

Vis Pump-probe Transient Absorption (TA) Spectrum of CdS-Au Nanorods

Vis pump-probe TA experiments for selected samples were also carried out. The details of the visible pump-probe setup can be found in chapter 2. Figure A.6.6A shows the TA spectra of CdSAu5.0nm under 580 nm excitation. The early spectrum (0.3-0.5ps) shows a pronounced Au plasmon bleach around 530nm and its photoinduced absorption at 400-500nm because of the Au plasmon excitation. A CdS band edge exciton bleach signal around 460nm appears on top of the broad Au signal, indicating the ultrafast hot electron transfer from the Au to CdS, consistent with

the transient IR results. Then, the Au signal decays rapidly to nearly zero due to cooling the hot electron. Only CdS bleach signal can be seen in the late-time spectrum (>100ps). It is hard to quantify the initial CdS bleach amplitude in the visible TA spectra because of the overlap of with the plasmon signal. The comparison of CdS signals measured with the visible probe and IR probe is shown in Figure A.6.6B. For this comparison, the visible TA signal at the CdS exciton bleach is flipped and these signals are scaled to the same amplitude at late time (~100ps) when the Au signal is negligible. It is clear that due to the Au plasmon photoinduced signal, the visible signal at wavelength of CdS 1S exciton in early time doesn't agree with the IR signal. However, at longer delay times, when the Au signal have completely decayed, these signals appear to share the same decay kinetics. Figure A.6.6C shows the spectra of CdSAu sample with Au size 1.8±0.5nm under 550nm excitation. This sample is not shown in the main text. Its transient visible spectra also consist of broad Au plasmon signal and CdS bleach signal, indicating ultrafast hot electron transfer from Au to CdS. In this case, the plasmon band is less pronounced due to the low extinction coefficient of small Au. The comparison of scaled transient visible signal of CdS and transient IR signal of CdSAu1.9nm (a similar but not identical Au size) is shown in Figure A6.6D. Again these signals deviates at early delay times due to the plasmon photoinduced absorption of the Au.

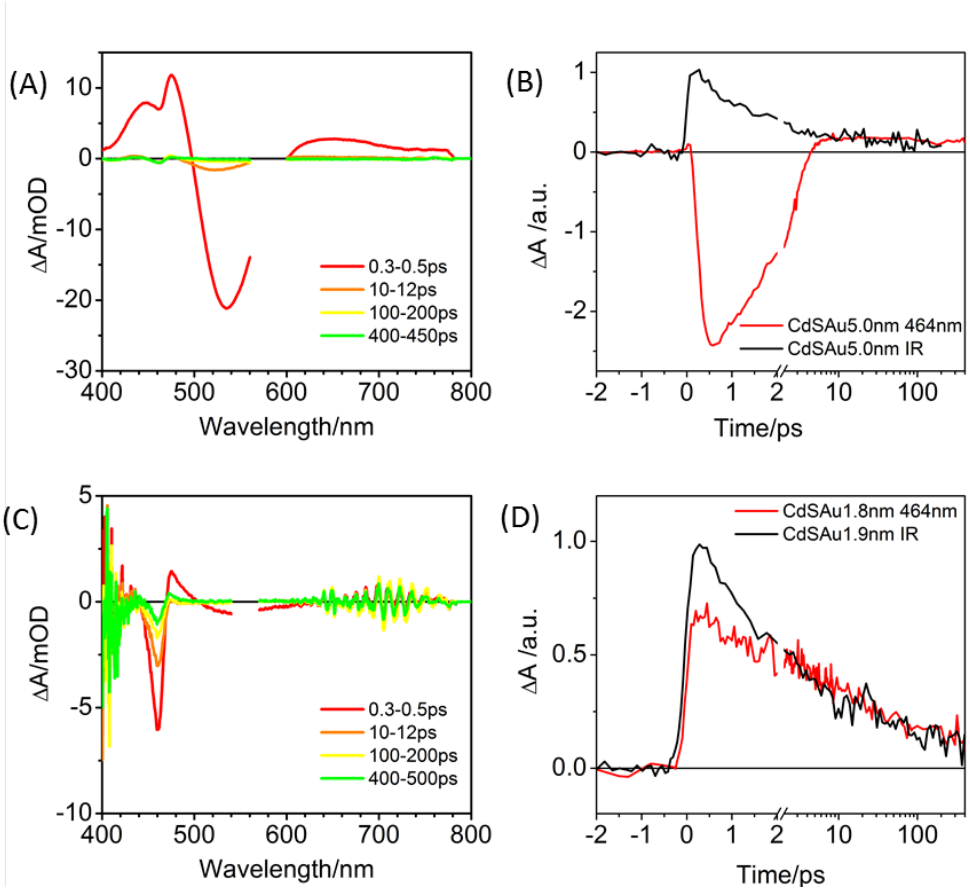

Figure A.6.6. Transient visible absorption spectra and kinetics. (A) Transient visible spectra of CdSAu5.0nm (A-B) measured with 595 nm excitation. (B) Comparison of transient kinetics probed in the visible (464 nm, at CdS exciton bleach) and IR (3700 nm) of CdSAu5.0nm. (C) Transient visible spectra of CdSAu1.8nm measured with 550 nm excitation. (D) Comparison of the transient visible kinetics of CdSAu1.8 nm probed at 464 nm with the transient IR kinetics CdSAu1.9nm probed at 3700 nm. In B and D, the transient visible signal has been inverted for better comparison with the transient IR signal and these signals have been scaled to the same amplitude at ~ 100 ps.

Appendix 5

Hot Electron Injection Efficiency Measurement

The quantum efficiency of the electrons transferred to the CdS from the Au tip as a result of 595 nm excitation can be quantified by the mid-IR intraband absorption at ~ 3700 nm of conduction band electrons in CdS. To determine the hot electron transfer quantum efficiency, we must quantify the amplitude of IR signal per CdS conduction band electron (S_0). It is previously reported that the mid-IR signal can be attributed the electron signal in CdS nanorods. So, S_0 can be calculated with following Eq. (A.6.4):

$$S_0 = \frac{\Delta A(\mathrm{CdS,400nm})}{\#\ of\ CdS\ CB\ electrons} \qquad \text{(A.6.4)}$$

ΔA is the maximum signal amplitude obtained from the kinetics by averaging the signal within 0.5-0.7ps. # of CdS CB electrons equals to absorbed photons by CdS, because every photon creates one band edge electron under 400 nm excitation. This number equals to the product of pump photon flux and the sample absorption ($\frac{\frac{power}{h\nu}}{beam\ size} * (1 - 10^{-\mathrm{OD}})$). Beam size here represents the overlap of pump beam and probe beam and hv is energy per photon.

The QE calculated by the # of hot electron generated in CdSAu per absorbed photons under 595nm excitation, shown by Eq.(A.6.5).

$$\mathrm{QE} = \frac{\#\ of\ hot\ electrons}{\#\ of\ absorbed\ photons} = \frac{\frac{\Delta A(\mathrm{CdSAu,595nm})}{S_0}}{\frac{\frac{power(595nm)}{h\nu(595nm)}}{beam\ size(595nm)} * \left(1-10^{-\mathrm{OD(CdSAu,595nm)}}\right)}$$

$$= \frac{\mathrm{beam\ size(\ 595nm)}}{beam\ size(\ 400nm)} * \left[\frac{\frac{\Delta A(\mathrm{CdSAu,595nm})}{\frac{power(595nm)}{h\nu(595nm)}}}{\frac{\Delta A(\mathrm{CdS,400nm})}{\frac{power(400nm)}{h\nu(400nm)}}} \cdot \frac{\left(1-10^{-\mathrm{OD(CdS,400nm)}}\right)}{\left(1-10^{-\mathrm{OD(CdSAu,595nm)}}\right)}\right] \qquad \text{(A.6.5)}$$

The first term $\frac{\mathrm{beam\ size(\ 595nm)}}{beam\ size(\ 400nm)}$ represents the ratio of the pump beam sizes at 595 nm and 400 nm excitations and can be calibrated by a calibration sample such as Cd_3P_2 (or CdSe) quantum dots

under the same conditions. The calibration samples can be excited at both wavelengths with same QE of generating conduction band electrons, which leads to

$$\frac{\text{beam size}(\ 595\text{nm})}{beam\ size(\ 400nm)} = \frac{\frac{\frac{\Delta A(\text{CdSe},595\text{nm})}{power(595nm)}}{\frac{hv(595nm)}{\left(1-10^{-\text{OD}(\text{CdSe},595\text{nm})}\right)}}}{\frac{\frac{\Delta A(\text{CdSe},400\text{nm})}{power(400nm)}}{\frac{hv(400nm)}{\left(1-10^{-\text{OD}(\text{CdSe},400\text{nm})}\right)}}}. \qquad \text{(A.6.6)}$$

Thus, the quantum efficiency of hot electron transfer in CdS-Au NRs is given by Eq. (A.6.6).

$$\text{QE} = \frac{\Delta\text{S}(\text{CdSAu},595\text{nm})}{1-10^{-\text{OD (CdSAu, 595nm)}}} \Big/ \frac{\Delta\text{S}(\text{CdS, 400nm})}{1-10^{-\text{OD (CdS, 400nm)}}} \cdot \frac{\Delta\text{S}(\text{CdSe},400\text{nm})}{1-10^{-\text{OD (CdSe, 400nm)}}} \Big/ \frac{\Delta\text{S}(\text{CdSe, 595nm})}{1-10^{-\text{OD (CdSe, 595nm)}}} \quad \text{(A.6.6)}$$

Here, we have defined $\Delta\text{S} = \frac{\Delta\text{A}}{\frac{power}{hv}}$, a quantity to be obtained from transient IR measurement. To improve the measurement accuracy and to check the linearity of the signal, we have measured ΔA as a function excitation power for all samples. An example is shown in **Figure A.6.7.** For all samples measured, the TA signal amplitude increases linearly with excitation power. ΔS can be obtained from the slope of the linear fits in **Figure A.6.7**. For all samples, the OD at excitation wavelength is controlled within 0.15-0.5 to maintain nearly uniform light intensity across the sample cell.

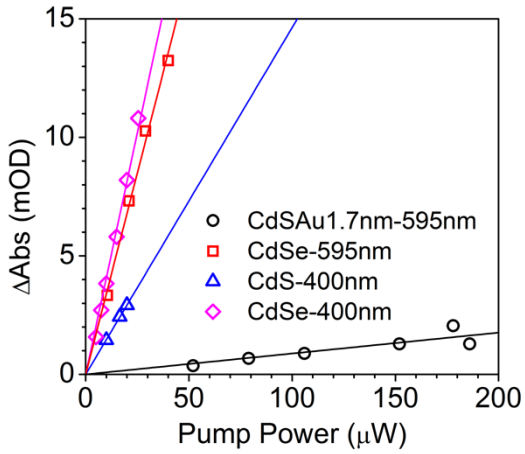

Figure A.6.7. Measurement of hot electron transfer efficiency. Dependence of peak signal amplitudes as a function of excitation power in CdSAu1.7nm (595 nm excitation), CdS (400 nm excitation), CdSe (400 nm excitation) and CdSe(595 nm excitation) are shown as an example.

Appendix 6

Calculated Hot Electron Efficiency after Accounting for Au Size Distribution

For simplicity, in our modelling of the size-dependent QEs shown in **Figure 6.4B**, we have not accounted for the Au size distributions. Our intent is to illustrate the qualitative trends of the size dependence of three factors, i.e. hot electron generation efficiency, Fowler hot electron transfer efficiency, and coupling strength. These trends are clearly illustrated in the dashed lines shown in **Figure 6.4B**. The Au size distribution can be accounted for by convoluting the computed values with the measured size distribution using Eq. (A.6.7).

$$QE(R_{ave}) = \int \frac{1}{\sqrt{2\pi\sigma^2}} \exp[-\frac{(R-R_{ave})^2}{2\sigma^2}]^2 QE(R)dR \qquad \text{(A.6.7)}$$

In Eq. (A.6.7), $QE(R)$ is the quantum efficiencies given by various terms shown in Eq. (6.4)

and (6.5), and shown as the dashed lines in **Figure 6.4B**. The experimentally determined size distribution is fit by a Gaussian function with a standard deviation of σ, which is listed in **Table A.6.2**. $QE(R_{ave})$ is the calculated values after accounting for the size distribution and is plotted in **Figure A.8** for various factors in the overall hot electron transfer efficiency.

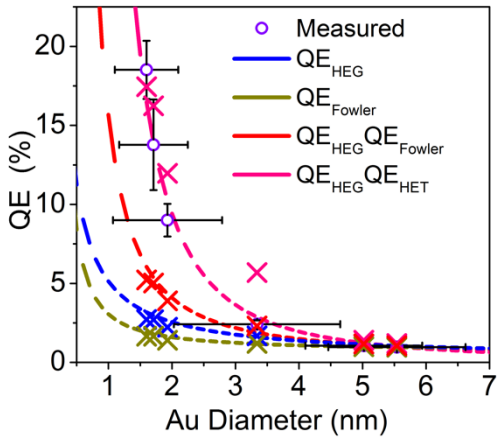

Figure A.6.8. Calculated efficiencies (X) after accounting for the Au size distribution according to Eq.(A.6.7). The remaining quantities are the same as those shown in Figure 6.4B of the main text.

Chapter 7. Summary and Outlook

Searching for efficient photocatalytic systems for solar-energy conversion has been long interested. Among various systems, colloidal semiconductor/metal heterostructures is regarded as a promising candidate. In this photocatalyst, semiconductor domain serves as the light absorber and the metal as the catalyst. Such catalysts combine the superior light absorption and efficient charge transport properties of the semiconductor with the superior catalytic activity and selectivity of the metal.

In this thesis, using Pt-tipped CdS nanorods as a model system, we demonstrate that the overall light-driven H_2 generation process in CdS-Pt NRs involves 4 stages, including hole transfer from CdS to surface ligands, electron transfer from CdS to Pt, hole scavenging by sacrificial donor and water reduction at Pt surfaces, respectively. The quantum efficiency of H_2 production can be treated as the product of these four steps. In chapter 3 and 4, we demonstrate how the morphology of catalysts influences the rate of electron transfer, the rate of charge recombination in the charge separated state and the rate of water reduction by independently tuning the semiconductor and metal domain. In chapter 3, we focus on the Pt domain, where enhanced H_2 production rate is observed with increasing Pt size. This improvement can be attributed to the increase in the quantum efficiencies of both electron transfer and water reduction. Transient absorption spectroscopy measurements of CdS-Pt NRs reveal that the electron transfer rate increases with the Pt-size, which can be attributed to the increase in the density of state in Pt and coupling strength between CdS and Pt at larger Pt particles. In chapter 4, we demonstrate that extending the rod length from 0D CdS quantum dot to 28 nm nanorod increases the lifetime of charge separated state and suppress the charge recombination loss, thus, contributing to more efficient H_2 production. However, further increase in rod length leads to no improvement in charge-separated lifetime and H_2 production efficiencies.

Photocatalysis, especially for light-drive solar fuel production, such as H_2 production, CO_2 reduction and N_2 fixation, requires multielectron reduction at the catalyst sites. In chapter 5, we illustrate multiexciton recombination and dissociation processes in CdS-Pt by excitation-fluence dependence study. Due to the

deep hole trap states in CdS nanorods, the Auger recombination of trapped exciton scaling with $n^2(n-1)$, indicating the recombination likely undergoes trion interactions. The electron transfer rate from the CdS rod to the Pt tip is independent of the number of excitons and the ET process outcompetes multi-exciton Auger recombination to enable simultaneous multielectron transfer into the Pt. The total multiexciton dissociation efficiency can be well-predicted by a pseudo-first order kinetics which considers the competition between Auger recombination and electron transfer. The recombination of multi charge-separated state roughly scales with $n^{-3.5}$. Accelerated charge recombination indicates the necessity of efficient hole removal under intense excitation to enable slow photoreduction reactions. Our study illustrates the feasibility of driving multiple electron photoreduction reactions under conditions significantly different from the 1 sun illumination, which may offer a way to control the branching ratio of reaction pathways that require different number of electrons.

In Chapter 7, we investigate the mechanism of plasmon-induced hot electron in CdS-Au, which is the essential process involved in the emerging area of plasmonic hot carrier photocatalysis. Plasmon induced hot electron transfer process in CdS-Au proceeds via the conventional hot electron transfer pathway. It consists of two sequential steps, the generation of hot electrons plasmon decay and interfacial hot electron transfer. The total quantum efficiency can be regarded as the product of quantum efficiencies of these two steps. Reduction of the plasmonic nanoparticles' size into a few nanometers can greatly enhance the generation of hot carriers through intraband transitions within the nanoparticles by increased surface scattering mechanisms. Smaller particle size also leads to reduced injection barrier, further improving the efficiency.

In this dissertation, we have established the frameworks of understanding photon-driven H_2 production and plasmon-induced hot electron injection in semiconductor-metal nanorod heterostructures. However, detailed mechanisms of some the of the processes remain to be more fully explored. For instance, the morphology dependent carrier kinetics hasn't been fully

understood. We observed the length-dependence in electron transfer and charge recombination. However, the microscopic models for describing such behaviors have not been fully established. Although we have demonstrated the feasibility of multielectron transfer in CdS-Pt rods dispersed in organic solvents, experiments in aqueous phase under light-driven H_2 generation conditions haven't been carried out. It would be interesting to examine whether the simultaneous transfer of multiple electrons to Pt facilitates the light-driven H_2 production efficiencies. If successful, advanced design integrating various catalytic systems and solar energy concentration may be applied towards more efficient solar fuels generation.